UNIVERSIDADE FEDERAL DE SANTA CATARINA
CENTRO DE CIÊNCIAS FÍSICAS E MATEMÁTICAS
PROGRAMA DE PÓS-GRADUAÇÃO EM FÍSICA

Cheryl Henkels de Souza

Exclusive photo and electroproduction of vector mesons in proton and nuclear targets within the color dipole model.

Florianópolis
2023

Cheryl Henkels de Souza

Exclusive photo and electroproduction of vector mesons in proton and nuclear targets within the color dipole model.

Tese submetida ao Programa de Pós-Graduação em Física da Universidade Federal de Santa Catarina para a obtenção do título de doutora em física.
Orientador: Prof. Emmanuel Gräve de Oliveira, Dr.
Coorientador: Prof. Roman Sergeevich Pasechnik, Dr.

Florianópolis
2023

Ficha de identificação da obra elaborada pelo autor,
através do Programa de Geração Automática da Biblioteca Universitária da UFSC.

Souza, Cheryl Henkels de
Exclusive photo and electroproduction of vector mesons in proton and nuclear targets within the color dipole model / Cheryl Henkels de Souza ; orientador, Emmanuel Gräve de Oliveira, coorientador, Roman Sergeevich Pasechnik, 2023.
124 p.

Tese (doutorado) - Universidade Federal de Santa Catarina, Centro de Ciências Físicas e Matemáticas, Programa de Pós-Graduação em Física, Florianópolis, 2023.

Inclui referências.

1. Física. 2. Méson vetorial. 3. Modelo de dipolo de cor. 4. Colisões ultraperiféricas. 5. Cromodinâmica quântica. I. Oliveira, Emmanuel Gräve de. II. Pasechnik, Roman Sergeevich. III. Universidade Federal de Santa Catarina. Programa de Pós-Graduação em Física. IV. Título.

Cheryl Henkels de Souza

Exclusive photo and electroproduction of vector mesons in proton and nuclear targets within the color dipole model.

O presente trabalho em nível de doutorado foi avaliado e aprovado por banca examinadora composta pelos seguintes membros:

Prof. Magno Valério Trindade Machado, Dr.
Instituição UFRGS

Prof. Bruno Duarte da Silva Moreira, Dr.
Instituição UDESC

Profª Débora Peres Menezes, Dra.
Instituição UFSC

Certificamos que esta é a **versão original e final** do trabalho de conclusão que foi julgado adequado para obtenção do título de doutora em física.

Documento assinado digitalmente
Paulo Henrique Souto Ribeiro
Data: 26/09/2023 13:10:26-0300
CPF: ***.886.506-**
Verifique as assinaturas em https://v.ufsc.br

Coordenação do Programa de Pós-Graduação

Documento assinado digitalmente
Emmanuel Grave de Oliveira
Data: 25/09/2023 19:24:35-0300
CPF: ***.765.300-**
Verifique as assinaturas em https://v.ufsc.br

Prof. Emmanuel Gräve de Oliveira, Dr.
Orientador

Florianópolis, 2023.

ACKNOWLEDGEMENTS

First, I am grateful to my advisor, prof. Emmanuel G. de Oliveira, for the knowledge, experiences, and skills transmitted to me over these years of mentoring. I recognize the valuable role he played in my academic journey, and I appreciate all the fruitful discussions and projects developed under his guidance. I am also grateful to my co-advisor, prof. Roman Pasechnik, for his invaluable guidance, support, and expertise throughout the duration of this project

Another person who was very important in the development of this work was my friend and collaborator, Haimon Trebien. Thank you very much for all the hours spent checking my codes, all the interesting papers that you shared with me, all the conceptual questions that you helped me to solve, all the excellent ideas that you brought to the project, and above all, for the partnership built up over these years.

I would like to thank my research friends, Bruna, Edgar, Gabriel, and João, not only for proofreading this thesis and for their contributions to my project but also for their affection for me over this period. The scientific events we attended together will forever hold a special place in my memory. An addendum is extended to the former member, Caetano Ternes, whose remarkable sincerity and insightful comments have been greatly appreciated by me.

I would like to extend my heartfelt appreciation to all friends I have met during my graduation course, Betânia, Cristiane, Eduarda, Eduardo, Laura, Maria de Lourdes, Rafael, and Valéria. Your companionship, support, and shared experiences have made this journey truly memorable. From weekend study sessions to celebrating our achievements together, you have been a priceless part of my life. Thank you for the laughter, encouragement, and lasting friendships. I also want to express my gratitude to my friends, Antônio, César, and Gabriele, for the amazing memories we created together. Thank you for standing by me during difficult times, for lending me your ears, for showing concern, for offering wise counsel, and for befriending me. Your presence has brought immense happiness to my life.

I am deeply grateful to my family for all the encouragement and support provided throughout my educational journey. In particular to my mother for all the sacrifices she has made to ensure that I had access to quality education and a comfortable life. And to my grandmother, the most responsible for my education, the person who tirelessly aided me with homework and often studied with me for school exams. Who never put barriers to my goals and never accepted less than excellence in everything I have done. Thank you for believing I could do anything with effort and dedication and always encouraging me to reach for the stars.

Finally, I want to express my gratitude to UFSC for providing me with free and high-quality education, as well as to CAPES for its financial support. I am thankful to my professors for sharing their knowledge with me, and to all the Physics department staff for maintaining a conducive learning environment. I am especially appreciative of Mariângela for her kind words and helpful advice. Lastly, I would like to acknowledge everyone who directly or indirectly supported and contributed to this work.

"It's kind of fun to do the impossible."
(Walt Disney)

RESUMO

Nesse trabalho, fotoprodução e eletroprodução exclusivas dos estados fundamental e excitado dos mésons vetoriais ρ, ω, ϕ, ψ e Υ são discutidas em colisões hadrônicas ultraperiféricas (UPCs) com prótons e núcleos como alvo. Como estamos interessados em espalhamentos nos quais o projétil é um fóton virtual ou quase real produzido pelo lépton ou hádron incidente, nós empregamos o modelo de dipolo de cor, o qual permite a fatorização do processo em três etapas. A primeira consiste no desdobramento do fóton no par $q\bar{q}$, o qual é descrito por uma função de onda calculada perturbativamente. A segunda corresponde à interação desse par com o alvo, que é descrita por uma seção de choque de dipolo parametrizada para considerar os fenômenos não perturbativos. Nesse trabalho, usamos cinco parametrizações diferentes: duas integradas (GBW e KST) e três não integradas (bCGC, bSat e BK), estas dependentes do parâmetro de impacto. O terceiro passo é a transição do par $q\bar{q}$ num méson vetorial. As contribuições dessa parte para o cálculo de seções de choque totais e diferenciais em t é um dos principais objetos de estudo desse trabalho, por isso, para descrever mésons vetoriais leves e pesados, usamos dois modelos para a função de onda do méson vetorial: o modelo AdS/QCD holográfico e o modelo de potenciais (que incorpora a transformação de spin de Melosh). Com esse formalismo e com o próton como alvo, nós comparamos os nossos resultados com os dados disponíveis dos colisores HERA e LHC e obtivemos uma boa concordância tanto nos resultados diferenciais quanto nos resultados integrados. Para o caso nuclear, nós estendemos nossos cálculos a partir do uso da teoria de Glauber-Gribov e os aplicamos para a fotoprodução coerente e incoerente de mésons vetoriais em colisões ultraperiféricas com a inclusão dos efeitos de comprimento de coerência finito e sombreamento de glúons ajustado a dados. Nossos resultados independentes de t foram comparados com os dados disponibilizados pelo LHC, tanto para processos incoerentes (J/ψ a 2.76 TeV) quanto para processos coerentes (J/ψ e ψ' a 2.76 e 5.02 TeV). Enquanto que no primeiro caso não conseguimos descrever o único dado disponível no momento, no segundo caso, nós obtivemos uma boa descrição dos dados coerentes, especialmente para J/ψ, o que mostra a eficácia do formalismo utilizado. Já no caso dependente de t, a divulgação recente de dados de fotoprodução coerente de J/ψ a 5.02 TeV foi uma ferramenta conveniente para medir a eficácia dos nossos resultados, os quais se mostraram muito próximos dos dados experimentais. Nós também apresentamos predições para seções de choque para produção de $\Upsilon(1S)$ e $\Upsilon(2S)$ em energias do LHC ($s = 5.02$ TeV), que podem ser úteis no futuro com novas medições nos grandes colisores de partículas.

Palavras-chave: Méson vetorial. Modelo de dipolo de cor. Fotoprodução. Colisões ultraperiféricas. Cromodinâmica quântica. Modelo holográfico.

RESUMO EXPANDIDO

Um marco importante para a física de partículas ocorreu com a construção do colisor elétron-hádron HERA (do inglês "High Energy Ring Accelerator") em Hamburgo na Alemanha [1]. Sua vasta quantidade de medições, obtida entre 1992 e 2007, foi muito importante para a investigação da estrutura interna do próton e uma melhor visualização da distribuição dos seus componentes, que ocorreu com o advento da ideia de utilizar um lépton para sondar via a troca de um fóton as interações fortes do alvo. Um processo de grande relevância que tomou lugar nesse experimento foi a produção exclusiva de mésons vetoriais, onde exclusivo significa que no estado final há apenas o méson vetorial e o próton inicial. Esse processo permite a obtenção de observáveis diferenciais que portam informações importantes para a obtenção de uma imagem detalhada do próton. Esse tipo de processo pode ser descrito através do formalismo de dipolo de cor, que se baseia no fato de que no referencial de repouso do próton o tempo de vida do dipolo de cor é muito maior que o tempo de interação entre ele e o alvo.

Nesse modelo, um fóton se divide em um par quark-antiquark (o dipolo de cor), o qual interage elasticamente com o próton, e depois se recombina formando um méson vetorial (Fig. 1). Enquanto que a primeira etapa do processo é descrita pela função de onda do fóton, que é bem conhecida a partir do cálculo perturbativo da QED, a última etapa é descrita pela função de onda do méson vetorial, que apresenta diversas incertezas quanto a sua forma devido à inclusão de processos não perturbativos. Na literatura há algumas parametrizações para essa parte, e as mais conhecidas são a boosted Gaussian e a Gaus-LC, que são construídas analogamente à função de onda do fóton, mas assumindo-se uma forma gaussiana para a parte escalar [2]. Mesmo que essas funções descrevam de forma satisfatória os dados de processos exclusivos difrativos do HERA [3], essas análises simplificadas não descrevem a produção de estados excitados nem levam em conta vários efeitos que podem ter um impacto significativo nas predições teóricas, como a rotação de Melosh [4]. Com isso, um dos objetivos deste trabaho é estudar outras formas para as funções de onda de mésons vetoriais baseadas em princípios teóricos da QCD.

Num primeiro momento, decidiu-se usar uma abordagem de potenciais para obter as funções de onda de mésons vetoriais pesados, como o J/ψ e o Υ. Nesse caso, a função de onda é obtida no referencial de repouso do par $q\bar{q}$, através da solução da equação de Schroedinger não relativística para diversos potenciais de interação, e depois transformada para o referencial de momento infinito do par, onde está definido o formalismo de dipolo. Nesse procedimento, além do *boost* nos quadrivetores do par, também é necessário um boost nos spins, que é realizado através da rotação de Melosh. Com esse formalismo, foi possível calcular seções de choque totais e diferenciais para fotoprodução dos estados fundamentais $\psi(1S)$ e $\Upsilon(1S)$ e dos estados excitados $\psi(2S)$ e $\Upsilon(2S)$ com próton-alvo. Esses resultados conseguiram descrever bem os dados existentes para esses mésons, como será mostrado adiante.

O sucesso na descrição desses dados, foi um incentivo para estender esse formalismo para o caso de núcleo-alvo. Para isso, foi utilizado o modelo de Glauber-Gribov para considerar os diversos espalhamentos do dipolo com o núcleo, assim como a inclusão dos efeitos de comprimento de coerência finito e de sombreamento de glúons (ajustado aos dados). Com isso, foram calculadas seções de choque independentes de t para as produções coerente e incoerente dos mésons vetoriais $\psi(1S)$, $\psi(2S)$, $\Upsilon(1S)$ e $\Upsilon(2S)$. Os resultados para os estados de ψ foram

Figure 1 – Representação esquemática da amplitude de espalhamento para a produção exclusiva de mésons vetoriais a partir do modelo de dipolo de cor.

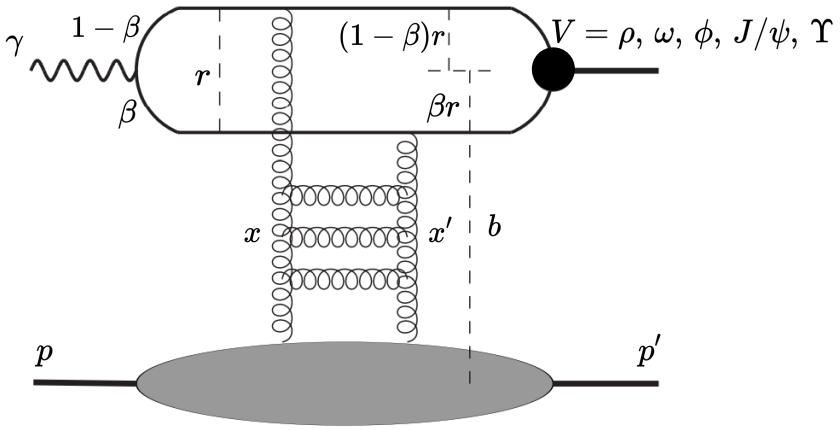

Source: Figura adaptada de [4].

comparados com os dados existentes do LHC e, no caso coerente (Fig. 2), conseguiu-se uma boa descrição dos dados (principalmente para o caso fundamental), porém, no caso incoerente, esse formalismo mostrou-se insuficiente para a descrição do único dado disponível do ALICE. Além disso, foram calculadas seções de choque dependentes de t para a fotoprodução coerente dos quatro mésons vetoriais pesados estudados e, graças à publicação de novos dados do ALICE em 2021, foi possível compará-los com os resultados de J/ψ e verificar que ambos concordavam.

Figure 2 – Distribuição em rapidez da fotoprodução coerente de ψ em colisões PbPb UPCs em 2.76 TeV (esquerda) e 5.02 TeV (direita). Os resultados obtidos para 2.76 TeV foram comparados com dados do CMS [5] e do ALICE [6, 7] para J/ψ e do ALICE [8] para ψ'. Os resultados para 5.02 TeV foram comparados com dados do ALICE [9] e com resultados preliminares do LHCb [10].

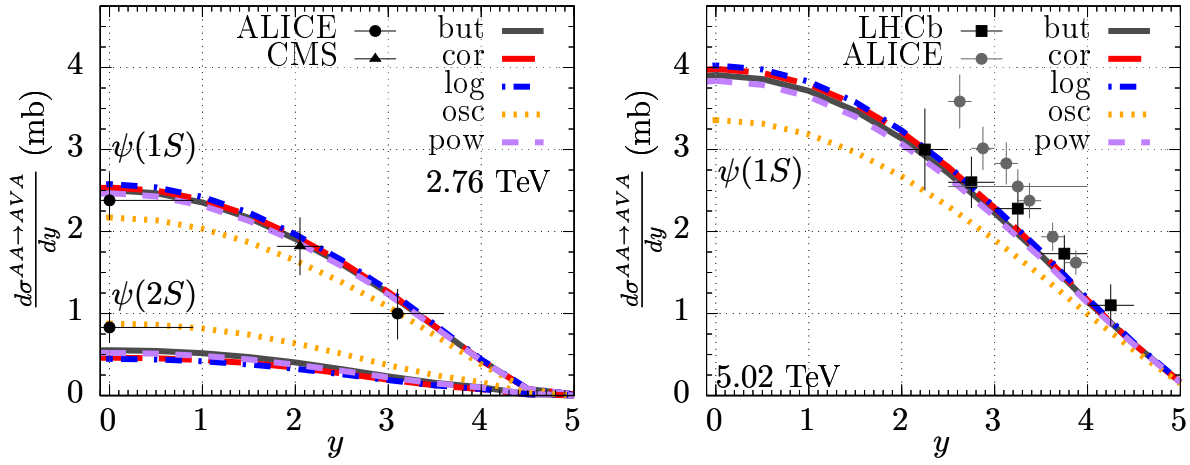

Source: Elaborado pela própria autora e publicado em [11].

Após estudar mésons vetoriais pesados, decidiu-se por estudar mésons vetoriais mais leves, como o ρ, o ω e o ϕ. Nesse caso, o fato deles possuírem uma massa menor faz com que ela

não possa ser usada como escala dura para o processo, ou seja, não é nítida a separação da parte perturbativa da não-perturbativa dos cálculos. Isso implica que a sua função de onda apresenta mais efeitos não perturbativos do que os mésons pesados estudados anteriormente, o que invalida o procedimento anterior para encontrar a função de onda. Para contornar esse problema, foi avaliado um modelo holográfico proposto por Brodsky e Téramond [12] para explicar a espectroscopia de mésons, e que baseia-se numa generalização da correspondência entre estados de corda do espaço anti-de Sitter (AdS) e teorias de campos conformes [13]. A vantagem desse modelo é que ele permite encontrar a função de onda do méson vetorial a partir da solução de uma equação relativística, igual a equação de Schroedinger, com um potencial de confinamento efetivo. Com essa abordagem, foi possível obter a função de onda tanto para os estados fundamentais dos mésons leves ρ, ω e ϕ quanto para seus estados excitados. Com isso, foi possível obter resultados para seções de choque totais e diferenciais com próton-alvo que conseguem descrever bem os dados existentes para o estado fundamental desses três mésons vetoriais leves. Além disso, conseguiu-se fazer predições para os seus estados excitados, o que não havia sido encontrado na literatura até o momento.

O último ingrediente do formalismo de dipolo de cor, que até agora não foi citado, é a seção de choque do dipolo, que é responsável pela descrição da interação do par $q\bar{q}$ com o alvo. Devido a sua natureza não perturbativa, ela não é calculada a partir dos primeiros princípios da QCD, mas sim, parametrizada e obtida a partir de ajustes com relação a resultados experimentais. Um problema encontrado é que os resultados obtidos a partir do formalismo de dipolo são fortemente dependentes da parametrização usada para a seção de choque do dipolo. Além disso, não há consenso entre os processos sobre qual é o melhor modelo para descrição dessa parte da interação. Com isso, nesse trabalho, cinco parametrizações são usadas: duas independentes do parâmentro de impacto (GBW e KST) e três dependentes do parâmetro de impacto (bCGC, bSat e BK) e percebe-se que cada uma delas descreve melhor um tipo de processo. Os resultados obtidos nessa tese podem ser importantes para definir qual é o melhor modelo para a seção de choque do dipolo, pois espera-se que novas medições desses observáveis sejam realizadas nos futuros colisores de partículas como o EIC (Electron Ion Collider) e o FCC (Future Circular Collider).

ABSTRACT

In this work, exclusive photo and electroproduction of ground and excited states of the vector mesons ρ, ω, ϕ, ψ, and Υ are discussed in ultraperipheral hadron collisions (UPCs) with proton and nucleus targets. Since we are interested in scatterings with the projectile being a virtual or quasi-real photon produced by the incoming lepton or hadron, we employ the color dipole model, which permits the factorization of the process into three steps. The first one is the splitting of the photon in a $q\bar{q}$ pair, which is described by a perturbatively calculated wave function. The second is the interaction of this pair with the target, which is described by a parametrized dipole cross section in order to account for the non-perturbative effects. In this work, we use five different parametrizations, two integrated (GBW and KST) and three unintegrated (bCGC, bSat, and BK), which are b-dependent. The third step is the transition of the $q\bar{q}$ pair into the vector meson. This part's contributions to the evaluation of total and t-differential cross sections is one of the main objects of study of this work, thus to describe light and heavy vector mesons, we used two models for the vector meson wave function: the AdS/QCD holographic model and the potential model (which incorporates the Melosh spin transformation). With this formalism and the proton as a target, we compared our results with the available data from the HERA and the LHC colliders, and we obtained a good agreement for both the differential and integrated results. For the nuclear case, we extended our calculations by using the Glauber-Gribov theory and applied it to the coherent and incoherent photoproduction of vector mesons in UPCs with the inclusion of the finite coherence length and gluon shadowing effects fitted to data. Our t-independent results are compared to the available LHC data in both incoherent (J/ψ at 2.76 TeV) and coherent (J/ψ and ψ' at 2.76 and 5.02 TeV) processes. While in the first case, we could not describe the data, in the second case, we obtained a good description of the coherent data, especially for J/ψ, which shows the efficiency of the formalism used. In the t-dependent case, the recent publication of coherent J/ψ photoproduction data at 5.02 TeV was a convenient tool to measure the efficiency of our results, which were very close to the experimental data. We also presented predictions for $\Upsilon(1S)$ and $\Upsilon(2S)$ cross sections at LHC energies ($s = 5.02$ TeV), which can be helpful in the future with new measurements on the large particle colliders.

Keywords: Vector meson. Color dipole model. Photoproduction. Ultraperipheral collisions. Quantum-chromodynamics. Holographic model.

RELATED PAPERS

Heavy vector mesons

- C. Henkels, E. G. de Oliveira, R. Pasechnik, and H. Trebien, "*Exclusive photoproduction of excited quarkonia in ultraperipheral collisions*", Phys. Rev. D 102 , 014024 (2020) , arXiv:2004.00607 .
- C. Henkels, E. G. de Oliveira, R. Pasechnik, and H. Trebien, "*Momentum transfer squared dependence of exclusive quarkonia photoproduction in ultraperipheral collisions*", Phys. Rev. D 104, 054008 (2021), arXiv:2009.14158.

Light vector mesons

- C. Henkels, E. G. de Oliveira, R. Pasechnik, and H. Trebien, "*Exclusive photo- and electroproduction of excited light vector mesons via holographic model*", Eur. Phys. J. C 83 6, 551 (2023), arXiv: 2207.13756.

CONTENTS

1 INTRODUCTION

Since the earliest civilizations that lived in this world, humanity has been intrigued by the fundamental question: "What are things made of?". Around the fifth century BC, an answer to this question emerged with Democritus and Leucippus, who proposed that matter was composed of tiny indivisible particles, which they called atoms. Today, it is known that the atom is not an indivisible structure, but in a general sense, it is formed by protons, neutrons, and electrons. A big step in understanding the composition of the atoms was taken in the 1960s with the discovery that the first two are not indivisible either, but they are composed of smaller particles called quarks [14].

1.1 STANDARD MODEL

The fundamental particles are grouped in what is called the Standard Model. It puts together the fundamental blocks that constitute the matter of the Universe (fermions, which have a half-integer spin) and the interaction mediators (bosons, which have an integer spin).

Fermions are classified into two groups: the quarks (which can not be found isolated in nature due to their color charge) and the leptons (that can exist alone). Each of these groups is composed of six particles. The six quark flavors are: up, down, strange, charm, top, and bottom, and they carry one of the three color charges: red, green, or blue. Since, in nature, just singlet-bound states can be observed (i.e., only states with neutral color charge can be measured), quarks combine to form bound states. The combination of three quarks is called baryon, while a state formed by a quark and an antiquark is named meson. Since each possesses a semi-half spin, mesons compulsorily have an integer spin. Mesons with zero spin and odd parity are called pseudoscalar mesons, such as pions. On the other hand, mesons with spin equal to one, and also odd parity, are called vector mesons (as an example, one can cite the ρ vector meson). Lastly, quarks also have a fractional electric charge; up, charm, and top quarks (first line in Fig. 3) possess $Q_{\mathrm{e}} = 2/3$ of the positron charge, while down, strange, and bottom (second line in Fig. 3) have $Q_{\mathrm{e}} = -1/3$.

As was aforementioned, leptons exist in six flavors: the electron, the muon, and the tau have an electric charge $Q_{\mathrm{e}} = -1$ (third line in Fig. 3), while each of its corresponding neutrinos (fourth line in Fig. 3) are electrically neutral and possess a very small mass. Leptons are colorless, thereby, can exist in isolation without forming composite states.

Besides this classification, fermions also can be divided into three generations (the first three columns in Fig. 3). Each generation contains two quarks (one with charge $2/3$ and one with charge $-1/3$) and two leptons (one with charge -1 and one with 0 charge). They are organized by the particle mass. Each generation, except maybe for neutrinos, has a higher mass than the previous one. This is known as the mass hierarchy, which explains why particles from the second and third generations decay into the first one. The first generation is composed of lighter particles, which can combine to form ordinary matter. The description of the matter

Figure 3 – Standard Models of elementary particles.

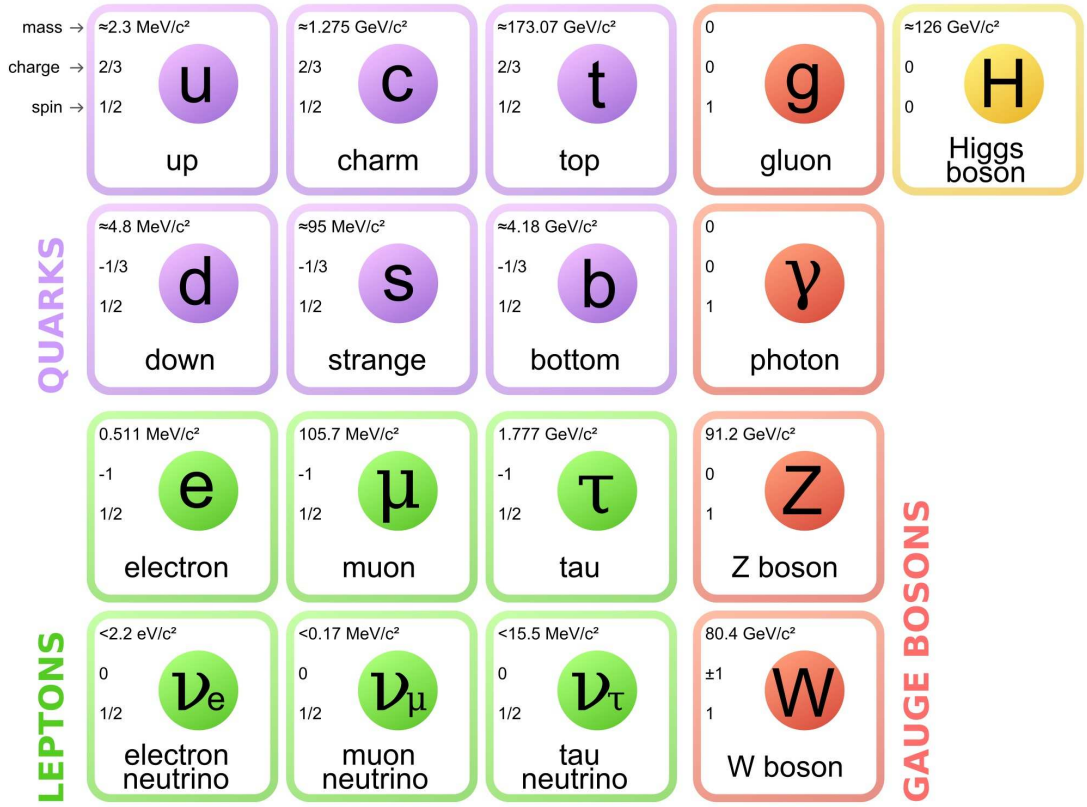

Source: Figure taken from [15].

in the Universe requires the existence of 12 building blocks. This number does not account for the antifermions, which need to be considered since in the Standard Model each particle is associated with an antiparticle (a particle with the same mass but opposite additive quantum numbers, such as electric and color charges). It also does not include the three possible color charges that each quark can possess. Thus, in light of all this, this sector of the Standard Model contains 48 building blocks [16].

Looking now for the boson sector, only W^+ and W^- are electrically charged, the other bosons are electrically neutral. As a consequence, W^+ is the W^- antiparticle, and vice-versa. They also can have spin 0 (scalar bosons) or spin 1 (vector bosons). In the first case, the Higgs boson is the only one that belongs to this category, being isolated in the fifth column of Fig. 3. It is also responsible for giving mass to the other particles. The second group is composed of the bosons which are responsible for three of the four fundamental forces that exist in nature. The photon carries the electromagnetic force, which is related to the electric charge. Gluons intermediate the strong force and are associated with the color charge. And finally, there are the Z and $W^\pm$ bosons, which are the mediators of the weak interactions and are responsible for the quark flavor change in charged currents [17].

1.2 QCD

Quantum chromodynamics (QCD) is a gauge theory responsible for the description of strong interactions. This means that it describes the force that exists between colorful quarks and antiquarks that occurs by the exchange of gluons, which also carry color charge. This last characteristic makes possible the interaction of gluons with themselves, which makes the theory richer and more complex, and, in addition, more difficult to be treated when compared to quantum electrodynamics (QED), which describes electromagnetic interactions [18].

The intensity with which these forces act is measured by the coupling constants α_{em} and α_s. In the electromagnetic interaction case, the fine-structure constant $\alpha_{\text{em}} \sim 1/137$ is much smaller than unity, which makes possible the use of perturbative theories in calculations involving QED. However, in strong interactions, the coupling constant varies considerably with energy, being relatively large for low energies (or large distances), and decreasing rapidly with increasing energy [19], as can be seen in Fig. 4. This fact evidences that studies involving QCD should consider two different energy regimes.

Figure 4 – Strong coupling constant as a function of the energy scale Q.

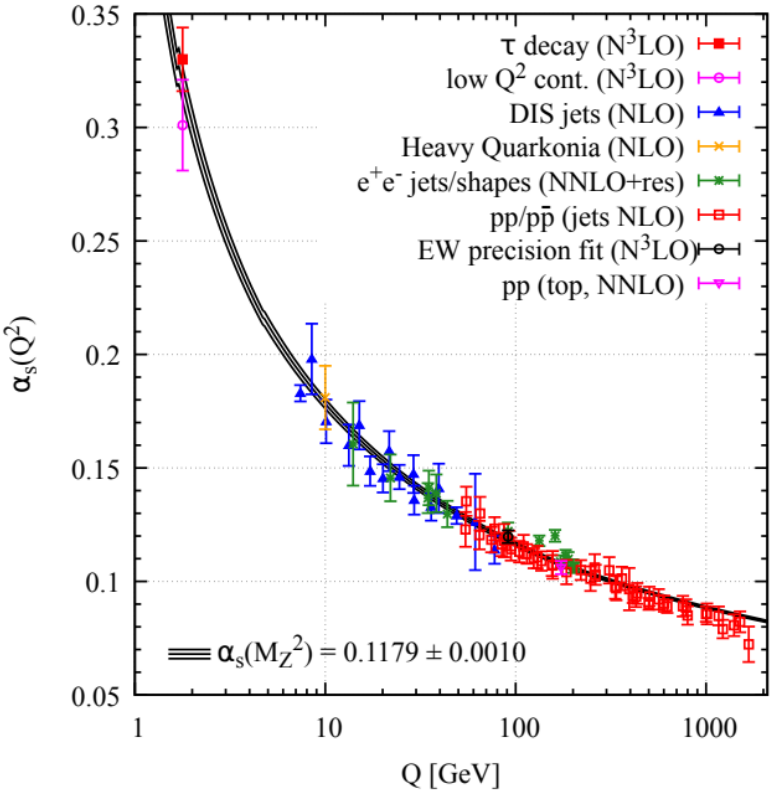

Source: Figure taken from [20].

In the high energy limit, the interaction between the quarks becomes very weak, causing them to move practically freely inside the hadrons. This property is called asymptotic freedom and allows the use of perturbative theories to perform the calculations. On the other hand, in

the low energy regime, the strong force grows as the separation between two quarks increases, in such a way that at a given moment the energy applied to the system is so great that a new $q\bar{q}$ pair is spontaneously produced, transforming the initial hadron into a pair of hadrons. This QCD particularity is called color confinement and prevents the observation of colored objects in nature. Furthermore, due to the size of the coupling constant, it is not possible to use perturbative techniques in this region, which makes the calculations extremely complicated and prompts the emergence of phenomenological models to deal with physics in this domain.

The Deep Inelastic Scattering (DIS) played an important role in improving the understanding of the proton structure [21]. It was vastly investigated in the HERA accelerator (Hadron-Electron Ring Accelerator), where it was realized that the deep inelastic scattering cross section was weakly dependent on Q^2. Actually, it was noticed that the structure function $F(x, Q^2)$ has a scaling behavior in the limit of $Q^2 \to \infty$, depending only on the variable x [22]. This variable, named after James Bjorken, is interpreted at leading-order (LO) as the fraction of the proton momentum carried by the parton that participates in the interaction [23]. This phenomenon was explained by Feynman by means of the parton model, which states that a proton is constituted by interacting point-like particles called partons. Quarks and gluons are considered partons. The second ones were vastly measured by HERA collider between 1996 and 2007. The way in which the partons are distributed inside the proton, or any nucleon, is described by parton distribution functions (PDFs), which are obtained by parameterizations [24] fitted to experimental data.

1.3 EXCLUSIVE VECTOR MESON PRODUCTION

The exclusive production of vector mesons in photon-proton or photon-nucleus collisions is a very interesting tool to understand the limits of perturbative QCD. Exclusive production means that in the final state there exists only the vector meson and the initial proton or nucleus. Regarding the production of heavy vector mesons such as J/ψ and Υ, which are respectively charm ($c\bar{c}$) and bottom ($b\bar{b}$) bound states, the quark mass m_Q can serve as a hard scale for the process, which determines the suitability of the perturbative theory in the calculation of the observables [25]. However, in the case of light vector meson production, as ρ, ω, and ϕ - where the first two are bound states composed by the superposition of up and down $q\bar{q}$ pairs and the third one is a strange bound state ($s\bar{s}$) - their quark masses are not high enough to work as a hard scale for the process [26]. This prevents a clear separation of the perturbative effects from the non-perturbative ones, a phenomenon known as factorization. Thus, for these processes, phenomenological techniques need to be applied in order to calculate observables.

Moreover, this type of production can play a significant and promising role in testing diffractive processes, which are characterized by the absence of an exchange of quantum numbers between the projectile and the target [27]. A notable aspect of diffractive interactions is that the final particle beams travel almost in the same direction as the initial one, generating a rapidity gap that provides a clear measurement. This means that in this kind of collision, the

interaction is minimal at the central region, which suggests that the interaction occurs through an exchange of a colorless object with the vacuum quantum numbers. In Regge theory, this object is called Pomeron and was proposed in 1961 to explain the growth of the hadronic cross section at high energies [28].

There are two different ways of exclusively producing vector mesons in photon–target collisions. The first one is called photoproduction, $\gamma p \to Vp$, and concerns the cases where the photon emitted by the (usually nucleus) projectile is quasi-real, which means that it has a virtuality that tends to zero ($Q^2 \sim 0$). The second one, known as electroproduction, $\gamma^* p \to Vp$, has a virtual ($Q^2 > 0$) photon originated from the (usually electron) projectile. In both cases, the quantum numbers of the projectile photon and the target remain unchanged, allowing their interaction to be described as a Pomeron exchange. Over the course of many years, the HERA collider served as a prominent facility for vector meson production and has accumulated an extensive quantity of measurements with proton targets. Its precise data were valuable to test the available theories and understand the exclusive vector meson production mechanism.

Recently, vector meson photoproduction data have been released by the Large Hadron Collider (LHC). This collider executes collisions involving both proton targets and nuclear targets, which means that these particles actively participate in the collision with the photon. When protons or nuclei emit the photons, they are regarded as the projectile. In the case of nuclear targets, the impact parameters must be larger than the sum of the two nuclei radii (ultraperipheral collisions - UPC) to ensure that they only interact through photon exchange. In the ultra-relativistic limit, using the Weizsäcker-Williams method, it is possible to factorize the collision cross section into a photon flux factor and a cross section for photon-nucleus interaction.

1.4 COLOR DIPOLE MODEL

The description of cross sections with the proton as a target and a photon as a projectile can be evaluated using the famous and successful color dipole model [29], which consists of a photon fluctuating into a quark-antiquark pair and interacting with the target before transforming into the vector meson. In the small dipole approximation, the photon part can be calculated with perturbative QED, presenting no big mysteries in its analytical form. However, the second and third parts present a significant contribution of nonperturbative effects, which encourage the use of parameterizations to describe them. Thus, they are vulnerable to uncertainties stemming from the choice of models [4]. In this work, it was selected five parameterizations for the strong interaction of the color dipole through gluon exchange: two integrated ones (GBW and KST) and three unintegrated ones (bCGC, b-Sat, and BK), which present an impact parameter dependence. The objective of testing this number of models is to achieve the best description of the data available in the literature. All these concepts are discussed in more detail in Chapter 2, which is destinated to the color dipole formalism and the elements that concern it.

In the literature, there is no profound understanding about what is the form of the vector meson wave function, the last part of the process in the color dipole model. It is common to describe it by utilizing a Gaussian form to encode all dynamics of the vector meson formation; however, since it is mostly fitted, it depends on the existence of data to restrict the parameterization parameters. For this reason, one of the biggest goals of this project was to study some important observables using wave functions based on the theoretical fundaments of QCD. It would be very nice to find a universal wave function for all vector mesons; however, as was aforementioned, their different masses make them work differently in distinct scale regimes. Therefore, this work addresses two models for the vector meson wave function: one for light vector mesons (the holographic model) and the other for the heavy ones: based on a solution of the Schrödinger equation in the $q\bar{q}$ pair rest frame for different interquark potential models and incorporating a boost on the spins (Melosh spin rotation).

These two models provide a framework to obtain not only the wave functions for the ground states but also the wave functions for the excited states. This fact is of great significance, as it allows the description of new data from LHCb and ALICE [8, 30] for $\psi(2S)$ and obtaining predictions for $\rho(2S)$, $\omega(2S)$, $\phi(2S)$, and $\Upsilon(2S)$. This will be of immense value with the construction of future high-energy colliders, such as the Electron-Ion Collider (EIC) [31] and the Future Circular Collider (FCC). These predictions are presented in Chapter 3, together with a thorough explanation of each vector meson wave function model. Moreover, this chapter shows total cross sections as a function of the center of mass energy W and differential cross sections as a function of the proton transferred momentum $|t|$ for the exclusive production of the ground and excited states of all five vector mesons: ρ, ω, ϕ, ψ, and Υ .

In Chapter 4, a generalization of this formalism for the case of nuclear targets will be presented. In this case, it is necessary to employ the Glauber-Gribov formalism to account for the various possible interactions of the dipole with the nucleons within the nucleus and to consider that the vector mesons can be produced coherently (when the nucleus remains intact) or incoherently (when after the collision the nucleus final state is different than its initial state). In nuclear target collisions, there are two important effects to consider. The first is gluon shadowing, which occurs when higher states with gluon inclusions are present and survive a shorter time than the $|q\bar{q}\rangle$ state [32]. The second is the finite coherence length, which is related to the finiteness lifetime of the quark-antiquark pair. Both effects lead to a suppression of the cross section, however, the former is more relevant at high energies, while the latter affects more the low-energy regime. The final results are presented at the end of the chapter, which include rapidity distributions for the coherent and incoherent cases and t-dependent differential cross sections, both considering heavy vector meson photoproduction at LHC energies.

2 COLOR DIPOLE FORMALISM FOR VECTOR MESON PRODUCTION WITH PROTON AS THE TARGET.

The exclusive vector meson production processes are powerful and effective tools for exploring the limit between perturbative (hard QCD) and non-perturbative phenomena (soft QCD). The production of bound states such as Υ provides a sufficiently hard scale (m_b) that enables the application of perturbative calculations. The production of slightly lighter states such as ψ exhibits a semi-hard scale and can work as an environment to study the interplay between the two regimes. And finally, the production of very light vector mesons such as ρ, ω, and ϕ possesses a soft scale, which makes non-perturbative effects dominate the process. Developing a formalism capable of describing the data for all these vector mesons is a good way to test the efficiency of the parameterizations responsible for describing non-perturbative aspects and validate their universality.

Furthermore, the exclusive production of vector mesons allows the determination of differential observables, such as differential cross sections that depend on kinematic variables. These observables are extremely important for obtaining a detailed description of the proton structure, highlighting the dependence of this structure on the impact parameter. Considering these motives, this chapter will present a study of this process through the lens of color dipole formalism.

2.1 KINEMATICS OF THE PROCESS WITH A PROTON TARGET.

The exclusive vector meson production in γp scattering is a diffractive process in which the proton remains intact. It can be measured in fixed target experiments as well as in electron-proton and proton-proton collisions. Its lowest order diagram (Fig. 5) consists of an electron emitting a photon with four-momentum $q = k - k'$, which subsequently interacts with the target proton. This interaction is represented in Fig. 5 by the dashed bubble.

In order to describe the kinematics of this interaction, it is helpful to define some invariant quantities, like:

$$\begin{aligned} s &= (p+k)^2 \\ Q^2 &= -q^2 = -(k-k')^2 \\ x &= \frac{(p-p')\cdot q}{p\cdot q} \approx \frac{M_x^2+Q^2}{W^2+Q^2}. \end{aligned} \tag{1}$$

On the first line, $\sqrt{s}$ is the total center-of-mass (c.o.m) energy of the collision between the incident particle and target proton (ep, pp, or Ap), M_x is the bound state mass produced in the collision and x is the modified Bjorken-x. The virtuality Q^2 measures how much off-shell the photon is. The Heisenberg principle states that the virtuality can be related to the resolution in which the photon probes the proton, and is approximately $1/\sqrt{Q^2}$. The last invariant is the center of mass energy of the photon-proton system squared, given by $W^2 = (p+q)^2$.

This process has two particles in the final state, Vp, as such it can be described by

Figure 5 – Kinematics of the vector meson production through an electron-proton collision.

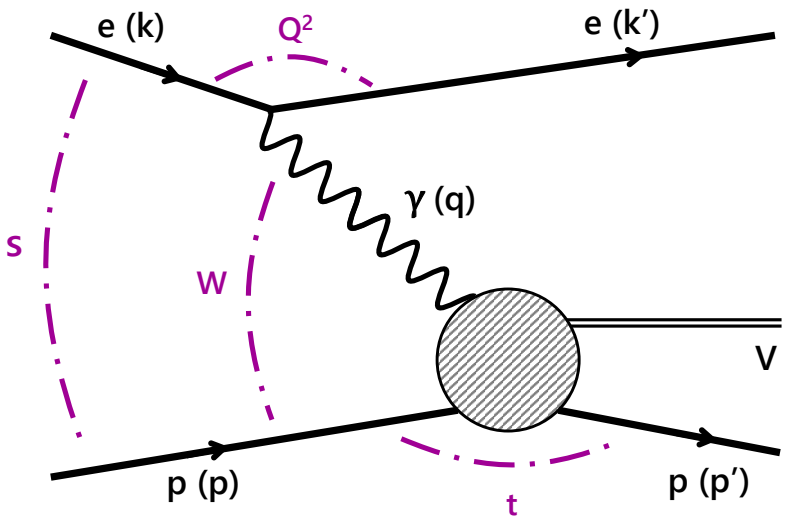

Source: Elaborated by the author.

two independent variables [33]. The cross section does not depend on the azimuthal angle φ, but it does depend on the scattering angle θ. However, since it is not Lorentz-invariant, it is convenient to write it in terms of the Mandelstam variable t

$$t = (p' - p)^2 = m_p^2 + m_{p'}^2 - 2E_p E_{p'} + 2|\boldsymbol{p}||\boldsymbol{p'}|\cos\theta, \tag{2}$$

which corresponds to the difference between the proton four-momentum before and after the interaction. Together with initial-state dependent W, we have the complete description.

In the high energy limit, it is possible to approximate the energy and the momentum absolute value by (See Appendix F):

$$E_p, E_{p'}, |\boldsymbol{p}|, |\boldsymbol{p'}| \underset{W^2\to\infty}{\simeq} \frac{W}{2}, \tag{3}$$

and neglect the particle masses. Thereby, it is found the following relation for the scattering angle:

$$\cos\theta = 1 + \frac{2t}{W^2} \tag{4}$$

Finally, it is interesting to express the vector meson transverse momenta $\Delta_T \equiv |\boldsymbol{\Delta}|$ as function of the invariants t and W^2:

$$\Delta_T^2 = |\boldsymbol{p'}|^2 \sin^2\theta \cong -\left[t + \frac{t^2}{W^2}\right], \tag{5}$$

which in the high energy limit, $W^2 \to \infty$, becomes

$$\Delta_T^2 \simeq -t. \tag{6}$$

2.2 COLOR DIPOLE PICTURE

The photon-proton interaction can be described by the color dipole picture, which is based on the fact that in quantum mechanics a photon can fluctuate into a $q\bar{q}$ pair, which can strongly interact with a proton. The reason why it is possible to use this approach is that, in the proton rest frame, the fluctuation lifetime is bigger than the duration of the interaction. This permits the factorization of the cross section into a part that deals with the photon transformation into the quark-antiquark pair and another that models the interaction. Briefly, the γp elastic scattering can be divided into three steps: first, the photon splits into a $q\bar{q}$ pair, which then interacts elastically with the proton and, finally, recombines into a vector meson (Fig. 6).

Figure 6 – Schematic representation of the scattering amplitude for the vector meson production in the color dipole picture.

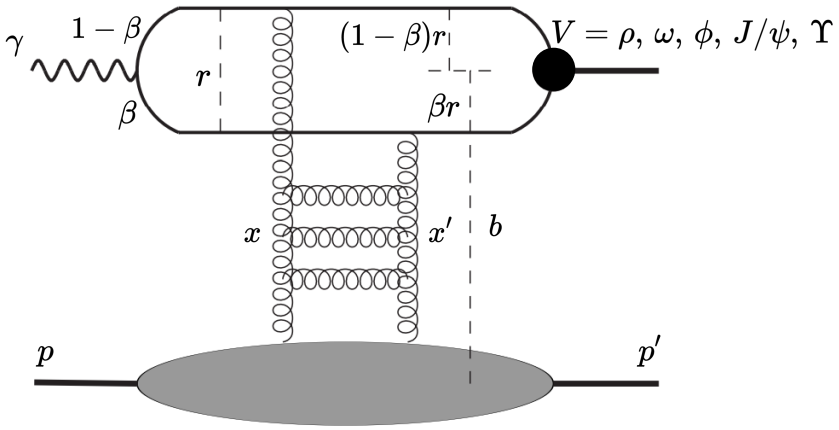

Source: Figure adapted from [4].

The scattering amplitude for this process is given by the product of the amplitude of each subprocess integrated in β and r, which are the momentum fraction of the photon carried by the quark and the $q\bar{q}$ transverse distance,

$$\mathcal{A}^{\gamma p}\left(x, \Delta_T\right) = \int \mathrm{d}^2\boldsymbol{r} \int_0^1 \mathrm{d}\beta \Psi_V^*(r,\beta)\Psi_\gamma(r,\beta)\mathcal{A}_{q\bar{q}}(x,\boldsymbol{r},\boldsymbol{\Delta})\,. \tag{7}$$

In this equation, Ψ_γ is the photon wave function (vertex $\gamma \to q\bar{q}$), Ψ_V is the vector meson wave function (vertex $V \to q\bar{q}$) and $\mathcal{A}_{q\bar{q}}(x,\boldsymbol{r},\boldsymbol{\Delta})$ is the elementary elastic amplitude of the dipole-proton interaction, which can be related to the S-matrix as:

$$\mathcal{A}_{q\bar{q}}(x,\boldsymbol{r},\boldsymbol{\Delta}) = \int \mathrm{d}^2\boldsymbol{b}\, \mathrm{e}^{-\mathrm{i}\boldsymbol{b}\cdot\boldsymbol{\Delta}}\, \mathcal{A}_{q\bar{q}}(x,\boldsymbol{r},\boldsymbol{b}) = \mathrm{i}\int \mathrm{d}^2\boldsymbol{b}\, \mathrm{e}^{-\mathrm{i}\boldsymbol{b}\cdot\boldsymbol{\Delta}}\, 2[1 - S(x,\boldsymbol{r},\boldsymbol{b})]\,. \tag{8}$$

From the optical theorem[1] it is possible to correlate the imaginary part of the forward elementary elastic amplitude ($\boldsymbol{\Delta} = 0$) with the total dipole cross section (a universal ingredient

that will be explained later) [2]

$$\begin{aligned}\sigma_{q\bar{q}}(x,\boldsymbol{r}) &= \mathrm{Im}\mathcal{A}_{q\bar{q}}(x,\boldsymbol{r},\boldsymbol{\Delta}=0)\\ &= \int \mathrm{d}^2\boldsymbol{b}\, 2\left[1-\mathrm{Re}S(x,\boldsymbol{r},\boldsymbol{b})\right]\\ &\equiv \int \mathrm{d}^2\boldsymbol{b}\, 2N(x,\boldsymbol{r},\boldsymbol{b})\end{aligned} \tag{9}$$

Considering that the elementary elastic amplitude is purely imaginary, which is a safe approximation in the high energy limit, it is possible to use the optical theorem to rewrite the scattering amplitude of the $\gamma p \to Vp$ process (Eq. 7) as:

$$\mathcal{A}^{\gamma p}(x,\Delta_T) = 2i\int \mathrm{d}^2\boldsymbol{r}\int_0^1 \mathrm{d}\beta \int \mathrm{d}^2\boldsymbol{b}\Psi_V^*(r,\beta)\Psi_\gamma(r,\beta)\mathrm{e}^{-i[\boldsymbol{b}-\frac{(1-2\beta)}{2}\boldsymbol{r}]\cdot\boldsymbol{\Delta}}N(x,\boldsymbol{r},\boldsymbol{b})\,. \tag{10}$$

This equation includes a correction that considers the finite size of the color dipole, which is not necessarily smaller than the proton size. It was first introduced by Kowalski, Motyka, and Watt, who stated that the non-forward elementary amplitude ($\Delta \neq 0$) could be written exactly as (8), but multiplying it by the exponential factor $\exp\left[-i(1-\beta)\boldsymbol{r}\cdot\boldsymbol{\Delta})\right]$. This approach was used in many works [34, 35, 36, 37, 3], including our first two papers [11, 38] (which show results of heavy vector meson photoproduction). However, recently, the authors of [39] underlined that this term is not compatible with the requirement made in [40] that the amplitude should be invariant under replacing quark and antiquark kinematic variables: $\beta \to 1-\beta$ and $r \to -r$. Thus, they show that the correct phase factor is $\exp(-i\frac{1-2\beta}{2}\boldsymbol{r}\cdot\boldsymbol{\Delta})$, which we included in our third paper [41] (that presents results for light vector mesons). Implementing the correct factor provided a better description of the t-dependent cross sections since it enhanced the cross section at larger t values, preventing the curves from dropping so fast.

Recalling that the formalism presented previously was constructed based on the supposition that the scattering amplitude is purely imaginary, we chose to include a term on Eq. 10 referent to the ratio of its real to its imaginary part, in order to consider the small contribution of the real part of the amplitude. Thus the modification of the amplitude is:

$$\mathcal{A}^{\gamma p} \Rightarrow \mathcal{A}^{\gamma p}\left(1-i\frac{\pi\lambda}{2}\right), \quad \mathrm{com} \quad \lambda = \frac{\partial \ln \mathcal{A}^{\gamma p}}{\partial \ln(1/x)}\,. \tag{11}$$

This substitution was suggested in [42], and it is based on dispersion relations on pp collisions, as can be seen in [43, 44] and in Appendix C. However, there are no known ways to extend this approach to other hadronic processes, consequently this expression should be considered an *ansatz*.

Another correction introduced in the calculations is the skewness effect. It takes into account that the gluons exchanged between the $q\bar{q}$ pair and the target nucleon can carry

[1] Originally, in the high energy limit, the optical theorem presents a factor $1/W^2$ multiplying the imaginary part of the amplitude: $\sigma_{q\bar{q}}(x,\boldsymbol{r}) = \frac{\mathrm{Im}\mathcal{A}_{q\bar{q}}(x,\boldsymbol{r},\boldsymbol{\Delta}=0)}{W^2}$. However, the absorption of this denominator into the definition of the amplitude was conventionalized in the dipole formalism, which leads to an amplitude with the dimension of $1/\text{energy}^2$. This subject is discussed in more detail in [2].

different momentum fractions (x and x'). This effect is not considered in the dipole cross section, since the optical theorem makes the two gluons have symmetric momenta. Thus, on the limit of $x' \ll x \ll 1$ and small t values, it is possible to include the skewness effect by multiplying the scattering amplitude by the factor [45]:

$$R_g(\lambda) = \frac{2^{2\lambda+3}}{\sqrt{\pi}} \frac{\Gamma(\lambda + 5/2)}{\Gamma(\lambda + 4)} . \tag{12}$$

2.3 COLOR DIPOLE PARAMETRIZATIONS

An essential ingredient of the color dipole formalism is the universal dipole cross section $\sigma_{q\bar{q}}(r, x)$. It is responsible for describing the interaction between the $q\bar{q}$ pair and the target nucleon and it is directly related to the gluon distribution inside the proton. It was introduced for the first time in [29], more than 40 years ago, and it is based on the fact that the interaction eigenstates in QCD, at high energies, are dipoles with a fixed transverse size r. This implies that the value of the dipole cross section for each color dipole with a different size is an interaction eigenvalue.

It is possible to see in Eq. 10 that all the scattering amplitude dependence on the energy is located on the partial dipole amplitude $N(x, r, b)$. This dependence comes from higher-order corrections related to gluon radiations. This means that besides the photon splits into a $q\bar{q}$ pair, like in Fig. 6, it also can split into higher Fock states (that include gluons), like $q\bar{q}G$, $q\bar{q}2G...q\bar{q}nG$. In this case, the radiated gluons are responsible for the emergence of the dependence of the partial dipole amplitude on the energy.

For small dipoles, it is possible to use perturbative QCD (pQCD) to find this dependence on the energy [42]. However, for larger dipoles, the strong interaction coupling constant becomes very high, which precludes the use of pQCD in this regime. Therefore, a phenomenological form is necessary to describe this part of the interaction. A lot of parameterizations are available in the literature and some of them will be shown hereafter.

2.3.1 GBW

One of the first parameterizations to succeed, mostly on the description of deep inelastic scattering (DIS) events, was proposed by Golec-Biernat and Wüsthoff (GBW) [46, 47] in 1998 and presented a very simple form given by:

$$\sigma_{q\bar{q}}(x, r) = \sigma_0 \left(1 - e^{-\frac{r^2 Q_s^2(x)}{4}} \right) . \tag{13}$$

In this case, σ_0 is merely a constant parameter, and $Q_s^2(x) \equiv R_0^{-2}(x) = Q_0^2 \left(\frac{x_0}{x}\right)^\lambda$ is the saturation scale (or the inverse of the saturation radius), which delimits the regime where the saturation effects become relevant. Eq. 13 is responsible for describing two phenomena; the first is called color transparency and basically considers that the dipole cross section has a quadratic behavior ($\sigma_{q\bar{q}} \propto r^2$) in the $r \to 0$ limit (or in other words, the target becomes more

transparent to interactions with smaller color dipoles). The second phenomenon is saturation. It occurs in the limit of high r values, when the photon wavelength $\sim 1/Q$ reaches the target size, making the dipole cross section approach a constant value σ_0. Another aspect considered by [46], refers to the fact that on the small-x regime, the partons inside the proton form a dense system, which permits them to interact with each other and recombine. This means that the density of partons that effectively interact is limited (there will be partons that will be just spectators of the interaction), and the point where this effect starts to be relevant is defined by the saturation scale. This limitation on the effective interactions makes the cross section approach a constant value, which is called black disk limit.

It is worth emphasizing that Eq. 13 depends on the photon virtuality Q^2 by means of x. In the original paper [46], the authors define it with a dependence on the quark masses $x = (Q^2 + 4m_f^2)/(Q^2 + W^2)$. They also provided two sets of fit parameters: one for only three light flavors, and another including the charm quark. In the course of our studies, we tested both the original set of fits as well as the updated GBW fit found in [48], and we observed that the numerical differences in the results obtained were minimal. However, regarding the results for total $\gamma p \to Vp$ photoproduction cross section at higher W (these results will be discussed in Sec.3.2.1), we noticed that the original GBW parameterization is somewhat closer to the data points. For this reason, we chose the "old" GBW fit for the evaluation of the observables in this work. Its four free parameters were fitted to HERA data for F_2 structure function [47],

$$Q_0^2 = 1 \text{ GeV}^2, \quad x_0 = 3.04 \times 10^{-4}, \quad \lambda = 0.288, \quad \sigma_0 = 23.03 \text{ mb}\,, \tag{14}$$

enabling a good description of several observables in ep and pp collisions at high energies.

2.3.2 KST

On the soft limit, where the virtuality goes to zero (photoproduction), the Bjorken variable x is not a very proper variable to describe the data. This issue motivated Kopeliovich, Schäfer, and Tarasov to develop a model (named KST) [49], whose dipole cross section is treated as a function of the center of mass energy squared of the photon-nucleon system, $\hat{s} = W^2$, and is more convenient for hadronic processes.

In this case, they used a simple form for the dipole cross section analogous to that used in GBW model:

$$\sigma_{\bar{q}q}\,(r, \hat{s}) = \sigma_0(\hat{s}) \left[1 - e^{-r^2/R_0^2(\hat{s})}\right] . \tag{15}$$

However, now the parameters $\sigma_0(\hat{s})$ and $R_0(\hat{s})$ are energy dependent,

$$R_0(\hat{s}) = 0.88 \text{ fm}\,(s_0/\hat{s})^{0.14}\,, \quad \sigma_0(\hat{s}) = \sigma_{\text{tot}}^{\pi p}(\hat{s}) \left(1 + \frac{3R_0^2(\hat{s})}{8\,\langle r_{\text{ch}}^2 \rangle_\pi}\right) \ , \tag{16}$$

and are chosen in a way that the normalized dipole cross section reproduces the pion-proton total cross section [50]

$$\sigma_{\text{tot}}^{\pi p}(\hat{s}) = 23.6\,(\hat{s}/s_0)^{0.08}\,\text{mb}. \tag{17}$$

Besides that, on Eq. 16, $\langle r^2_{\rm ch}\rangle_\pi = 0.44$ fm^2 is the mean pion charge radius squared [51] and $s_0 = 1000$ GeV^2. More information about this model can be found in [49], where they state that the success of this model is guaranteed only up to $Q^2 \sim 10$ GeV^2.

2.3.3 bSat

With the purpose of describing t-distributions for the exclusive vector meson production, it is necessary to use a dipole cross section that depends on the impact parameter, since this is the Fourier conjugate variable to the transferred momentum. A famous parameterization with this dependence was proposed by Kowalski and Teaney [52] to describe HERA data, and is well known by the name bSat. This parameterization also has an exponential behavior

$$N(x, \boldsymbol{r}, \boldsymbol{b}) = 1 - \exp\left(-\frac{\pi^2}{2N_c} r^2 \alpha_s(\mu^2) x g(x, \mu^2) T(b)\right) \tag{18}$$

that depends on the gluon density $xg(x, \mu^2)$, the number of colors ($N_c = 3$) and the strong coupling constant $\alpha_s(\mu^2)$, which depends on the scale $\mu^2 = 4/r^2 + \mu_0^2$ (found in [2] as $\mu_0^2 = 1.17$ GeV^2).

In the original model [52], the initial gluon density is expressed as an ansatz, which is evolved from the initial scale μ_0^2 (fitted to ZEUS data [53, 54]) to μ^2 through the factorization scale evolution equation DGLAP (Dokshitzer [55], Gribov-Lipatov [56] e Altarelli-Parisi [57]) at leading order (LO) without the inclusion of quarks in the gluon density. However, in this work, we used the parton distribution function (PDF) CT14LO [58] parameterized to data from several processes. The deviation between the results obtained with these two different approaches is very small, thus, aiming for the universality of the description of the QCD non-perturbative phenomena, we chose CT14LO over the original gluon distribution for the calculations. Besides that, it was considered a Gaussian form for the proton shape function

$$T(b) = \frac{1}{2\pi B_G} \mathrm{e}^{-b^2/2B_G}\,, \tag{19}$$

with the slope parameter $B_G = 4.0$ GeV^{-2} [2].

2.3.4 BK

The DGLAP evolution equation, which generally is used for the description of HERA data, is not very appropriate when x approaches the saturation limit, because in this regime the parton density becomes so high that the neighboring gluon ladders start to overlap [59]. Therefore, the Balitsky-Kovchegov (BK) evolution equation [60, 61, 62] can be a more interesting option on the description of the photoproduction processes since it includes a non-linear term that controls the rise of the gluon density in the saturation region. A recent solution for the BK equation, which includes a b-dependence in the partial dipole amplitude, can be found in [63]. It considers only the absolute value of the transversal dipole size r and of the

impact parameter b, i.e., it does not depend on the angle between $\boldsymbol{r}$ and $\boldsymbol{b}$. This leads to a BK equation with the form:

$$\frac{\partial N(r,b,Y)}{\partial Y} = \int d\boldsymbol{r_1} K\left(r,r_1,r_2\right)\left(N\left(r_1,b_1,Y\right)+N\left(r_2,b_2 Y\right)-N(r,b,Y)\right. \\ \left.-N\left(r_1,b_1,Y\right)N\left(r_2,b_2,Y\right)\right) , \tag{20}$$

which has $N(x,r,b)$ as the partial dipole amplitude, that appears in Eq. 10, with rapidity $Y=\ln(0.008/x)$.

An interesting fact about this solution is that it has a new and improved kernel $K\left(r,r_1,r_2\right)$ [64] that suppresses daughter dipoles with large transverse size, fixing the problem of Coloumb tails (a name given to a phenomenon related to an unphysical growth of the cross section for high b-values).

2.3.5 bCGC

Another parameterization that includes the non-linear saturation effects is the bCGC dipole model. It was first proposed, without impact parameter dependence, by Iancu, Itakura, and Munier in [65] as an interpolation of two limiting behavior functions. The first one is the analytical solution of the Balitsky-Fadin-Kuraev-Lipatov (BFKL) equation, valid in the vicinity of the saturation line, for small dipoles ($r \ll 2/Q_s$); and the second is the Levin-Tuchin solution [66] for the BK equation, used in the saturation limit to include the non-linear effects that appear with large dipoles ($r \gg 2/Q_s$). In their model, called CGC, the dipole-proton amplitude is given by [2, 3, 67]:

$$N(x,\mathbf{r},\mathbf{b}) = \begin{cases} N_0\left(\frac{rQ_s}{2}\right)^{2[\gamma_s+(1/(\eta\Lambda Y))\ln(2/rQ_s)]} & rQ_s \leq 2 \\ 1-e^{-\mathcal{A}\ln^2(\mathcal{B}\,r\,Q_s)} & rQ_s > 2 \end{cases} , \tag{21}$$

with $Y=\ln(1/x)$ and $\eta = 9.9$ (fixed at the LO BFKL value [65]). The parameters $\mathcal{A}$ and $\mathcal{B}$ are determined by the condition that the partial dipole amplitude $N(x,\mathbf{r},\mathbf{b})$, as well as its derivative with respect to rQ_s, must be continuous at $rQ_s=2$, which gives:

$$\mathcal{A} = -\frac{N_0^2\gamma_s^2}{\left(1-N_0\right)^2\ln\left(1-N_0\right)}, \quad \mathcal{B} = \frac{1}{2}\left(1-N_0\right)^{-\frac{1-N_0}{N_0\gamma_s}} . \tag{22}$$

The b-dependence was introduced later on the CGC model by Watt, Motyka and Kowalski [2], who included it in the saturation scale:

$$Q_s \equiv Q_s(x,b) = \left(\frac{x_0}{x}\right)^{\Lambda/2}\left[\exp\left(-\frac{b^2}{2B_{\mathsf{CGC}}}\right)\right]^{1/(2\gamma_s)} . \tag{23}$$

This was quite a natural choice, because it is expected that the gluon distribution is higher in the center of the proton than in its outskirts, thus the saturation effects should be stronger in the center, which can be taken into account with a saturation scale that depends on x and b. This model was called bCGC, and its parameters N_0, x_0 γ_s, and Λ were obtained by a fit to

the HERA data (we used the ones for $m_c = 1.4$ GeV in [3]), while B_{CGC} was determined by requiring a good description of the t-distribution of the exclusive J/ψ photoproduction.

It is worth emphasizing that the dipole cross sections are parameterized considering just the part of the gluon density that grows at small-x values. From the constituent counting rules [68, 69, 70], it is known that the gluon density inside the target should decrease as $g(x) \propto (1-x)^N$ for $x > 0.01$. In [71], it was verified that multiplying the saturation scale by this factor improves the description of Drell-Yan process for larger x, maintaining the results mostly unaltered for small x. Regarding this, we chose to follow the same approach as [72] and multiply the dipole cross section by the factor $(1-x)^{2n_s-1}$, where n_s is the number of spectator quarks. In the color dipole model, these quarks represent the sea quark contribution, and for this reason, we set $n_s = 4$.

2.4 PHOTON WAVE FUNCTION

The photon wave function is the part of the scattering amplitude that carries the information about the photon fluctuation into the quark-antiquark pair. Basically, it describes the probability of finding a quark (antiquark) carrying a fraction of the momentum of the photon β $(1-\beta)$ and separated by a distance r. This vertice was calculated with perturbative QED by many authors [73, 74, 75, 76, 77, 78] and its shape is very known in the literature [42]:

$$\Psi^{(\mu,\bar{\mu})}_{\gamma_{T,L}}\left(r,\beta,Q^2\right) = \frac{\sqrt{N_c\alpha_{\text{em}}}}{2\pi} Z_Q \chi^{\mu\dagger}_Q \hat{\mathcal{O}}_{T,L} \tilde{\chi}^{\mu}_{\bar{Q}} K_0(\varepsilon r), \quad \varepsilon^2 = \beta(1-\beta)Q^2 + m_Q^2. \tag{24}$$

In this equation the variables ε and Z_Q are, respectively, the energy and electric charge fraction of the quark that forms the dipole (ergo, $Z_u = Z_c = 2/3$ and $Z_d = Z_s = Z_b = 1/3$); χ^{μ}_Q and $\tilde{\chi}^{\bar{\mu}}_{\bar{Q}} \equiv i\sigma_y \chi^{\bar{\mu}*}_{\bar{Q}}$ are, in due order, the quark and antiquark spinors.

The operators $\hat{\mathcal{O}}_{T,L}$ are defined in the following way:

$$\begin{aligned} \hat{\mathcal{O}}_T &= m_Q \vec{\sigma}\cdot\vec{e}_\gamma + i(1-2\beta)(\vec{\sigma}\cdot\vec{n})\left(\vec{e}_\gamma\cdot\vec{\nabla}_r\right) + (\vec{n}\times\vec{e}_\gamma)\,\vec{\nabla}_r \\ \hat{\mathcal{O}}_L &= 2Q\beta(1-\beta)\vec{\sigma}\cdot\vec{n}, \quad \vec{\sigma} = (\sigma_x,\sigma_y,\sigma_z), \quad \vec{\nabla}_r \equiv \partial/\partial\boldsymbol{r} \end{aligned} \tag{25}$$

where $\vec{e}_\gamma$ is the photon transversal polarization, $\vec{n} = \vec{p_\gamma}/|\vec{p_\gamma}|$ is a unit vector that points to the photon momentum direction and $\sigma_{\{x,y,z\}}$ are the Pauli matrices. Looking at equation 25, it is evident that in the photoproduction case ($Q^2 = 0$) the photon longitudinal wave function is zero. Thus, one can use this process to study the photon transverse wave function.

It is worth mentioning that the fact that Eq. 24 was obtained by perturbative calculations makes this expression very reliable for small dipoles. However, when the $q\bar{q}$ separation is not small (large dipoles), confinement effects start to appear, which should be included in the photon wave function. Some studies about the subject can be found in [35, 76]. These effects become more relevant in light vector meson production at small virtualities since, in this case, there is no hard scale to inhibit the modified Bessel functions that appear in Eq. 24 from

becoming very large. This is not a concern in the heavy vector meson case, because the quark mass can be used as a hard scale, making it safe to use Eq. 24.

2.5 VECTOR MESON WAVE FUNCTION

The last part of the Eq. 10 is the vector meson wave function, which is one of the major sources of uncertainties in the vector meson production [4, 34, 79, 80, 81]. This comes from the fact that when one is dealing with bound states, one has to consider the existence of an interaction between the constituents [82], which adds non-perturbative effects to the calculations, such as color confinement. One can deal with that by projecting the physical vector meson onto the Fock space where the vector states are composed of free and non-interacting quarks and gluons $|V_{phys}\rangle = c_0|q\bar{q}\rangle + c_1|q\bar{q}g\rangle + c_2|q\bar{q}gg\rangle + c_3|q\bar{q}q\bar{q}\rangle + ...$, and the coefficients c_i are the wave functions of the physical vector meson projected in the states $|i\rangle$. The problem is that in Quantum Field Theory (QFT), it is uncertain whether the entire framework that assumes well-defined wave functions and vector mesons represented as states of free and non-interacting components would function properly. For this reason, many authors in the literature [2, 3, 34, 81] use a photon-like vertex, i.e. they assume that the vector meson wave function has the same polarization and helicity structure as the photon wave function, with the scalar part parameterized by a Gaussian function. This is the case of two often used vector mesons wave function models: the Boosted Gaussian [76] and the Gauss-LC [52, 83]. However, some recent works showed that the use of these simplified parameterizations can have a significant impact on the theoretical predictions of exclusive quarkonia production observables (something about 30% for the J/ψ cross section [4, 79]). As a result of the aforementioned circumstance, I was encouraged to seek out models based on first principles and capable of describing excited quarkonia states. Considering its importance to my work, I will allocate the next chapter to provide a comprehensive exposition on this topic.

2.6 CROSS SECTION

Now that all the ingredients of the amplitude were explained, it is possible to calculate the differential cross section, which, using the notation discussed earlier for the optical theorem (Eq. 9), is defined as [2, 84]:

$$\frac{\mathrm{d}\sigma^{\gamma p\to Vp}}{\mathrm{d}t} = \frac{1}{16\pi}\left|\mathcal{A}^{\gamma p}(x,\Delta_T)\right|^2 . \tag{26}$$

This equation will be a fundamental piece for describing the present HERA data as well as any measurement conducted by LHC and EIC in the future. A pictorial representation of this quantity can be found in Fig. 7.

In the integrated cross section calculus, it is customary to assume an exponential parameterization for the differential cross section behavior in the small-$|t|$ limit, $\frac{\mathrm{d}\sigma^{\gamma p\to Vp}}{\mathrm{d}t} \propto \mathrm{e}^{-Bt}$, with B representing the size of the interaction area [2]. This assumption comes from an analysis

Figure 7 – Pictoric representation of the cross section for J/ψ photoproduction in a collision with a proton as a target.

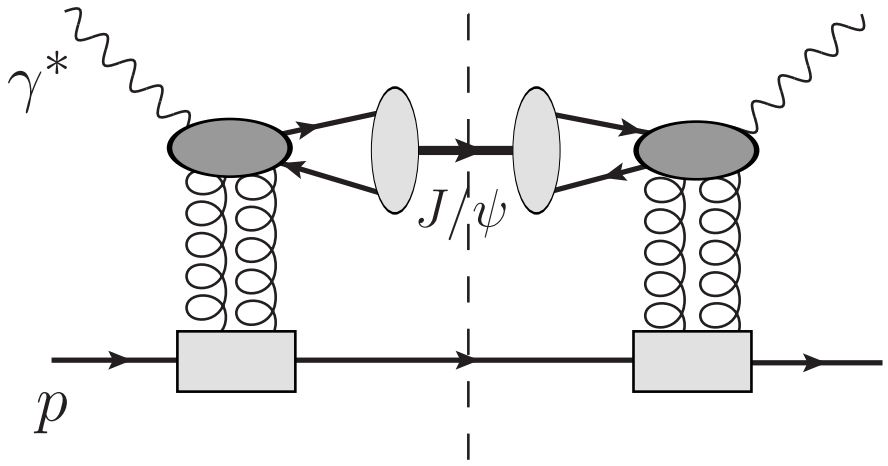

Source: Figure taken from [4].

of the phase space, where the perturbative QCD permits the calculation of hard processes, whereas soft processes cannot be computed with it. In the second case, the interactions bear a close resemblance to hadron-hadron elastic scattering, which can be described by soft Pomeron exchange, as dictated by Regge phenomenology [85]. This makes it possible to write the differential cross section as:

$$\frac{\mathrm{d}\sigma^{\gamma p\to Vp}}{\mathrm{d}t} = \left.\frac{\mathrm{d}\sigma^{\gamma p\to Vp}}{\mathrm{d}t}\right|_{t=0} \mathrm{e}^{-Bt}, \tag{27}$$

with B defined by the Regge trajectory [86, 4]:

$$B = B_0 + 4\alpha'(0)\ln\left(\frac{W}{W_0}\right). \tag{28}$$

The parameters $B_0 = 4.62$ GeV^{-2} and $\alpha'(0) = 0.171$ GeV^{-2} came from a fit to H1 [87, 88] and ZEUS [89, 90] combined data and can be found in [4]. Besides that, data shows [85, 91, 92, 93] that in the case where $Q^2 > 0$ or when one is interested in the exclusive production of the Υ heavy vector meson, the results obtained with Eq. 28 are not satisfactory, which suggests the necessity of inclusion of an empiric term in Eq. 28 [93]. Thus, for the heavy vector mesons production, the slope parameter takes the form:

$$B\left(W, Q^2\right) \approx B\left(W, Q^2 = 0\right) - B_1 \ln\left(\frac{Q^2 + M_V^2}{M_{J/\Psi}^2}\right), \tag{29}$$

with $B_1 = 0.45$ GeV^{-2}. For the light vector mesons, a better parameterization is given by [94, 95, 96, 97]:

$$B = N\left[14.0\left(\frac{1\mathrm{GeV}^2}{Q^2 + M_V^2}\right)^{0.2} + 1\right], \tag{30}$$

with $N = 0.55\,\mathrm{GeV}^{-2}$, which agrees with the ZEUS data for both ρ and ϕ production.

When B data is plotted as a function of the scale $\mu^2 = (Q^2 + M_V^2)/4$ (Fig. 8), one can see that it decreases with the scale increasing, until it approaches the asymptotic value of 5 GeV^{-2}. This is evidence of the fact that for small μ^2 values, the presence of large dipoles is enhanced and soft diffraction dominates the process, increasing the B slope value. However, with the increase of the scale, the size of the dipoles will decrease, and the hard diffraction will start to dominate until the fully hard regime is reached ("finite size" effects) [91].

Figure 8 – Elastic scattering data for the B slope parameter as function of the scale μ^2.

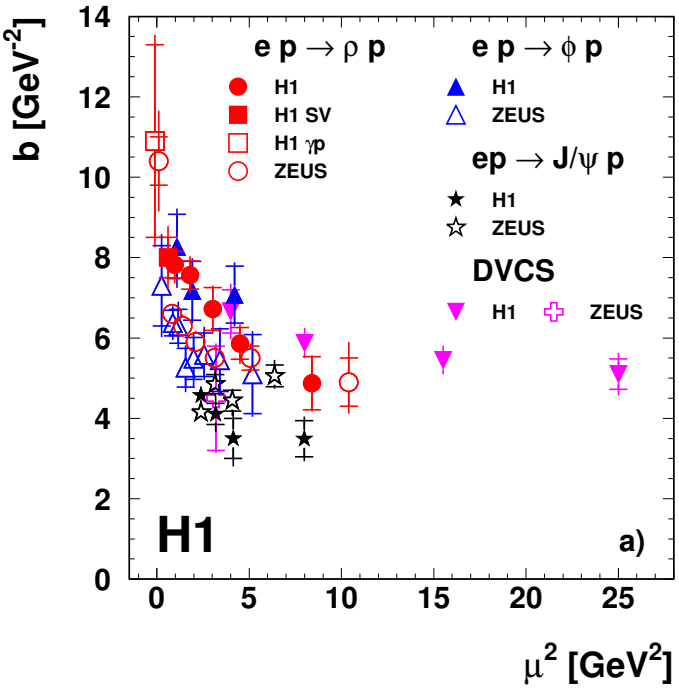

Source: Figure taken from [91].

After all this discussion, it is possible to find the total cross section for the vector meson exclusive production by integrating Eq. 27, and thus write it as

$$\sigma^{\gamma p \to Vp} = \frac{1}{16\pi B} \left| \mathcal{A}^{\gamma p \to Vp}(t=0) \right|^2 . \tag{31}$$

This equation will be used in the next section to calculate the total t-independent cross sections.

3 VECTOR MESON WAVE FUNCTIONS AND RESULTS

The pursuit of ways to describe the important aspects of nature is one of the biggest goals of theoretical physics. It would be very nice to be capable of obtaining each piece of the dipole model calculated completely by first principles. However, the behavior of the strong constant at small scales forbids the use of the known method of the perturbative QCD in all energy ranges. This directly impacts the attempt to find one universal model to describe the vector meson wave function for all vector mesons (ρ, ω, ϕ, ψ, and Υ) at once. The heavy vector mesons ψ, and Υ possess a significant mass that can serve as a hard scale that separates the perturbative dynamics from non-perturbative ones in an effect called factorization. However, the light vector mesons ρ, ω, and ϕ do not have a mass high enough to provide a sufficiently high scale to ensure that factorization works. Actually, their mass is so small that their wave functions are highly non-perturbative. This fact implies that the formalism used to obtain the wave functions is different for heavy and light vector meson production.

3.1 HEAVY VECTOR MESON WAVE FUNCTION

The heavy quarkonium wave function is obtained on the $q\bar{q}$ rest frame, where it is appropriately defined. In this reference frame, solutions for the non-relativistic Schrödinger equation for various quark-antiquark interaction potentials can be found, and these solutions are identified as the vector meson wave functions. While obtaining these solutions is not a challenging task, a complication arises due to the dipole approach being defined in the target rest frame. Consequently, a boost is required to transform from the dipole rest frame to the target rest frame. Moreover, it is advantageous to switch to the light cone variables: $x^+ = x^0 + x^3$ and $x^- = x^0 - x^3$ (additional properties are available in Appendix D), as they are a more convenient way for transforming to the reference frame. Following the original approach [42], this combination of a boost and a change of variables will be equivalent to the infinite momentum frame (IMF) of the $q\bar{q}$ pair.

The wave functions in the two aforementioned frames are related by a Lorentz transformation, which means applying a boost to the four-vectors of the pair and a Melosh spin rotation to the spins of the pair. In this simplified relation, the multiparticle effects are not considered. For instance, the lowest order $|q\bar{q}\rangle$ state in the rest frame does not correspond exactly to the lowest $|q\bar{q}\rangle$ state in the infinite momentum frame since the frame change can mix the states in the Fock space. Although interesting and relevant, this effect will not be included in the presented calculations since there is no consensus in the literature about how to describe it. It is expected that the contribution of this effect is small, in truth, even smaller than other neglected contributions that appear in next-to-leading order.

This task can be resolved by employing a methodology, as explained in [4, 42], that involves initially performing a Fourier transform of the wave function in the rest frame (RF)

from the coordinate space to the momentum space ($\Psi_V^{RF}(\tilde{\boldsymbol{r}}) \Rightarrow \Psi_V^{RF}(\boldsymbol{p})$):

$$\Psi_V^{RF}(p) = \frac{2}{\sqrt{2\pi}p}\int_0^\infty \mathrm{d}\tilde{r}\,\tilde{r}\Psi_V^{RF}(\tilde{r})\sin(p\tilde{r}), \quad \int \mathrm{d}^3p\,|\Psi_V^{RF}(p)|^2 = 1\,. \tag{32}$$

In these equations, $p \equiv |\boldsymbol{p}|$ is the quark 3-momentum in the rest frame and $\tilde{r} \equiv |\tilde{\boldsymbol{r}}|$ is the quark-antiquark separation in 3D.

The second step consists of boosting the wave function from the rest frame to the infinite momentum frame. For this purpose, one can use the Brodsky-Huang-Lepage prescription [98, 99] and equate the $q\bar{q}$ pair squared invariant mass in both frames. Thus, in the infinite momentum frame, the squared invariant mass is (Appendix E)

$$M_{Q\bar{Q}}^2 = \frac{p_T^2 + m_Q^2}{\beta(1-\beta)}\,, \tag{33}$$

while in the rest frame, it is given by:

$$M_{Q\bar{Q}}^2 = 4\left(p^2 + m_Q^2\right)\,, \tag{34}$$

in which p_L and p_T are respectively the longitudinal and transversal components of the three-momentum $\boldsymbol{p}$ and m_Q is the quark mass.

Equating both equations it is possible to find

$$p^2 = \frac{p_T^2 + (1-2\beta)^2 m_Q^2}{4\beta(1-\beta)}. \tag{35}$$

Using the fact that $p^2 = p_L^2 + p_T^2$ and isolating p_L^2 one obtain:

$$p_L^2 = \frac{\left(p_T^2 + m_Q^2\right)(1-2\beta)^2}{4\beta(1-\beta)}\,, \tag{36}$$

which is an appropriate kinetic variable conversion between the two frames. It will be useful to differentiate both sides of Eq. 36,

$$\mathrm{d}p_L = \frac{\sqrt{p_T^2 + m_Q^2}}{4\left(\beta(1-\beta)\right)^{3/2}}\mathrm{d}\beta\,, \tag{37}$$

and substitute it into the equation of the conservation of probability density:

$$\mathrm{d}^3p|\Psi_V^{RF}(p)|^2 = \mathrm{d}^2p_T\mathrm{d}\beta\left|\Psi_V^{IMF}\left(p_T,\beta\right)\right|^2, \quad \mathrm{d}^3p = \mathrm{d}p_L\mathrm{d}^2p_T \tag{38}$$

to thereby, obtain the Terent'ev relation [100] between the infinite momentum wave function $\Psi_V^{IMF}(p_T,\beta)$ and its counterpart in the rest frame $\Psi_V^{RF}(p)$:

$$\Psi_V^{IMF}\left(p_T,\beta\right) = \left(\frac{p_T^2 + m_Q^2}{16(\beta(1-\beta))^3}\right)^{\frac{1}{4}}\Psi_V^{RF}(p), \tag{39}$$

which is also normalized to $\int\left|\Psi_V^{IMF}\left(p_T,\beta\right)\right|^2\mathrm{d}^2p_T\mathrm{d}\beta = 1$.

Now that the boost from the rest frame to the dipole infinite momentum frame was done, it is time to add an essential ingredient to the Lorentz transformation, the Melosh spin rotation, responsible for the spin boost. The two bidimensional spinors χ_Q and $\chi_{\bar{Q}}$ that describe the quark and the antiquark in the infinite momentum frame respectively are related to the rest frame spinors $\bar{\chi}_Q$ and $\bar{\chi}_{\bar{Q}}$ via Melosh rotation [100, 101]:

$$\begin{aligned} \bar{\chi}_Q &= \widehat{R}\left(\beta, \boldsymbol{p}_T\right) \chi_Q \,, \\ \bar{\chi}_{\bar{Q}} &= \widehat{R}\left(1-\beta, -\boldsymbol{p}_T\right) \chi_{\bar{Q}}, \end{aligned} \tag{40}$$

in which the rotation matrix is given by:

$$\widehat{R}\left(\beta, \boldsymbol{p}_T\right) = \frac{m_Q + \beta M_{Q\bar{Q}} - i[\vec{\sigma} \times \vec{n}]\boldsymbol{p}_T}{\sqrt{\left(m_Q + \beta M_{Q\bar{Q}}\right)^2 + p_T^2}} \,. \tag{41}$$

Since the potentials used in this work are not spin-dependent, it is convenient to assume that the infinite momentum wave function can be factorized into a spatial part and a spin-dependent one

$$\Psi_V^{(\mu,\bar{\mu})}\left(\beta, \boldsymbol{p}_T\right) = U^{(\mu,\bar{\mu})}\left(\beta, \boldsymbol{p}_T\right) \Psi_V^{IMF}\left(\beta, p_T\right) \,, \tag{42}$$

in which the spin-dependent part

$$U^{(\mu,\bar{\mu})}\left(\beta, \boldsymbol{p}_T\right) = \frac{1}{\sqrt{2}} \bar{\chi}_Q^{\mu\dagger} \vec{\sigma} \cdot \vec{e}_V \tilde{\mathrm{X}}_{\bar{Q}}^{\bar{\mu}}, \quad \tilde{\mathrm{X}}_{\bar{Q}}^{\bar{\mu}} = i\sigma_y \bar{\chi}_{\bar{Q}}^{\bar{\mu}*} \,, \tag{43}$$

depends on the vector meson polarization vector $\vec{e}_V$ and on the aforementioned quark spinors. Lastly, with the help of Eq. 40 it is possible to write

$$U^{(\mu,\bar{\mu})}\left(\beta, \boldsymbol{p}_T\right) = \frac{1}{\sqrt{2}} \chi_Q^{\mu\dagger} \widehat{R}^{\dagger}\left(\beta, \boldsymbol{p}_T\right) \vec{\sigma} \cdot \vec{e}_V \sigma_y \widehat{R}^{*}\left(1-\beta, -\boldsymbol{p}_T\right) \sigma_y^{-1} \widetilde{\chi}_{\bar{Q}}^{\bar{\mu}} \,. \tag{44}$$

Now, it is possible to find the vector meson wave function in the infinite momentum frame as a function that depends on the longitudinal momentum and the transverse spatial coordinate, in the same way as it appears in Eq. 10. For this purpose, one just needs to apply a Fourier transformation in Eq. 42

$$\Psi_V^{(\mu,\bar{\mu})}\left(\beta, \boldsymbol{r}\right) = \frac{1}{2\pi} \int d^2 p_T \, \mathrm{e}^{-i\boldsymbol{p}_T \boldsymbol{r}} \Psi_V^{(\mu,\bar{\mu})}\left(\beta, \boldsymbol{p}_T\right) \,, \tag{45}$$

and then replace it, together with Eq. 44, in Eq. 10 to obtain the final expression for the scattering amplitude

$$\mathcal{A}_{T,L}^{\gamma p}(x, \Delta_T) = 2i \int \mathrm{d}^2\boldsymbol{r} \int_0^1 \mathrm{d}\beta \int \mathrm{d}^2\boldsymbol{b} \, \mathrm{e}^{-i[\boldsymbol{b} - \frac{(1-2\beta)}{2}\boldsymbol{r}]\cdot\boldsymbol{\Delta}} \times \Sigma_{T,L}(\beta, r) N(x, \boldsymbol{r}, \boldsymbol{b}) \,, \tag{46}$$

with $\Sigma_{T,L}$ given by

$$\Sigma_{T,L}\left(\beta, \boldsymbol{r}; Q^2\right) = \int \frac{\mathrm{d}^2 p_T}{2\pi} e^{-i\boldsymbol{p}_T \boldsymbol{r}} \Psi_V^{IMF\dagger}\left(\beta, p_T\right) \sum_{\mu,\bar{\mu}} U^{\dagger(\mu,\bar{\mu})}\left(\beta, \boldsymbol{p}_T\right) \Psi_{\gamma_{T,L}^*}^{(\mu,\bar{\mu})}\left(r, \beta, Q^2\right) \,. \tag{47}$$

Evaluating the sum over the spins and the angular integration in the Eq. 47, one finds:

$$\Sigma_L = Z_Q \frac{\sqrt{N_c \alpha_{\mathsf{em}}}}{2\pi\sqrt{2}} 4Q\beta(1-\beta) K_0(\varepsilon r) \int p_T \, \mathrm{d}p_T J_0\left(p_T r\right) \Psi_V\left(\beta, p_T\right) \frac{m_T m_L + m_Q^2}{m_Q\left(m_T + m_L\right)}, \quad (48)$$

for the longitudinal component. And, for the transverse component, it is convenient to write $\Sigma_T(\beta, \boldsymbol{r}) = \Sigma^{(1)}(\beta, \boldsymbol{r}) + \Sigma^{(2)}(\beta, \boldsymbol{r}) \frac{\partial}{\partial r}$ in terms of the coefficients

$$\Sigma^{(1)} = \frac{Z_Q \sqrt{N_c \alpha_{\mathsf{em}}}}{2\pi\sqrt{2}} \, 2K_0(\varepsilon r) \int \mathrm{d}p_T J_0(p_T r) \Psi_V(\beta, p_T) p_T \, \frac{m_T m_L + m_T^2 - 2\beta(1-\beta) p_T^2}{m_L + m_T}$$

and

$$\Sigma^{(2)} = \frac{Z_Q \sqrt{N_c \alpha_{\mathsf{em}}}}{2\pi\sqrt{2}} \, 2K_0(\varepsilon r) \int \mathrm{d}p_T J_1(p_T r) \Psi_V(\beta, p_T) \frac{p_T^2}{2} \, \frac{m_L + m_T + (1-2\beta)^2 m_T}{m_T(m_L + m_T)} \, .$$

In these equations $\alpha_{\mathsf{em}} = 1/137$ is the fine structure constant, $N_c = 3$ is the QCD number of colors, $J_{0,1}$ and K_0 are respectively the Bessel function and the modified Bessel function, $m_L = 2m_Q\sqrt{\beta(1-\beta)}$ and $\varepsilon = \sqrt{\beta(1-\beta)Q^2 + m_Q^2}$. The superscript notation "IMF" was also dismissed from the vector meson wave function in the last equations, and henceforth, it shall be a standard practice for all the wave functions defined in the infinite momentum frame.

3.1.1 Schrödinger equation solution for the potential model

Given that the procedure for transforming wave functions from the dipole rest frame to its infinite momentum frame has been demonstrated, it is essential, indeed, to calculate the wave functions in the rest frame.

As was aforementioned, in the rest frame the $q\bar{q}$ pair wave functions satisfy the non-relativistic Schrödinger equation [102]

$$\left(-\frac{\Delta}{2\mu} + V(\tilde{r})\right) \Psi_{nlm}(\tilde{\boldsymbol{r}}) = E_{nl} \Psi_{nlm}(\tilde{\boldsymbol{r}}), \quad \mu = \frac{m_q}{2} \, , \quad (49)$$

where μ is the $q\bar{q}$ pair reduced mass and the laplacian operator Δ acts on the coordinates of $\tilde{r}$ in the following way:

$$\Delta = \sum_{i=1}^{3} \frac{\partial^2}{\partial x_i^2} = \frac{1}{\tilde{r}^2} \frac{\partial}{\partial \tilde{r}} \left(\tilde{r}^2 \frac{\partial}{\partial \tilde{r}}\right) + \frac{1}{\tilde{r}^2 \sin\theta} \frac{\partial}{\partial \theta} \left(\sin\theta \frac{\partial}{\partial \theta}\right) + \frac{1}{\tilde{r}^2 \sin^2\theta} \frac{\partial^2}{\partial \varphi^2} \, . \quad (50)$$

Making a separation of variables between the radial and the angular parts,

$$\Psi_{nlm}(\tilde{\boldsymbol{r}}) = \psi_{nl}(\tilde{r}) Y_{lm}(\theta, \varphi) \, , \quad (51)$$

it is possible to part the Schrödinger equation (49), by utilizing Eq. 50, into two equations:

$$\begin{aligned} \frac{1}{\tilde{r}} \frac{\partial^2}{\partial \tilde{r}^2} (\tilde{r}\psi(\tilde{r})) + m_q(E - V(\tilde{r}))\psi(\tilde{r}) &= \frac{l(l+1)}{\tilde{r}^2} \psi(\tilde{r}) \\ \frac{1}{\sin\theta} \frac{\partial}{\partial \theta} \left(\sin\theta \frac{\partial Y(\theta,\varphi)}{\partial \theta}\right) + \frac{1}{\sin^2\theta} \frac{\partial^2 Y(\theta,\varphi)}{\partial \varphi^2} &= -l(l+1) Y(\theta, \varphi) \, , \end{aligned} \quad (52)$$

wherein, the quantum number $l = 0$ denotes the ground state, $l = 1$ corresponds to the first excited state, $l = 2$ represents the second excited state, and so forth. The first differential equation can be rewritten in a more convenient way

$$\frac{\partial^2 u(\tilde{r})}{\partial \tilde{r}^2} = (V_{\text{eff}}(\tilde{r}) - \epsilon_Q)\, u(\tilde{r}) \tag{53}$$

by the definition of two new quantities:

$$V_{\text{eff}}(\tilde{r}) = m_q V(\tilde{r}) + \frac{l(l+1)}{\tilde{r}^2}, \quad \epsilon_Q = m_q E\,. \tag{54}$$

In this equation, the relation between the radial wave function $\psi(\tilde{r})$ and the new one $u(\tilde{r})$ is given by: $u(\tilde{r}) = \sqrt{4\pi}\tilde{r}\psi(\tilde{r})$.

Lastly, the solution for the Schrödinger equation (53) can be obtained numerically for different $q\bar{q}$ interaction potentials. In this work, 5 different potential parameterizations were used:

- **Buchmüller-Tye potential (but)**

  The Buchmüller-Tye potential [103] presents a Coulomb-like behavior for small $\tilde{r}$ values and a string-like behavior at high $\tilde{r}$ values. Therefore, it presents two different forms for each regime. For $\tilde{r} \geq 0.01$ fm,

  $$V(\tilde{r}) = \frac{k}{\tilde{r}} - \frac{8\pi}{27}\frac{v(\lambda\tilde{r})}{\tilde{r}}\,, \tag{55}$$

  and for $\tilde{r} < 0.01$ fm

  $$V(\tilde{r}) = -\frac{16\pi}{25}\frac{1}{\tilde{r}\ln(w(\tilde{r}))}\left(1 + 2\left(\gamma_E + \frac{53}{75}\right)\frac{1}{\ln(w(\tilde{r}))} - \frac{462}{625}\frac{\ln(\ln(w(\tilde{r})))}{\ln(w(\tilde{r}))}\right)\,. \tag{56}$$

  In these equations, the used parameters were $w(\tilde{r}) = \frac{1}{\lambda_{\text{MS}}^2 \tilde{r}^2}$, $\lambda_{\text{MS}} = 0.509$ GeV, $k = 0.153$ GeV^2 , $\lambda = 0.406$ GeV, $\gamma_E = 0.5772$ is the Euler constant and the function $v(x)$ is evaluated numerically in [103]. Besides that, it was used $m_c = 1.48$ GeV and $m_b = 4.87$ GeV for the quark masses.

- **Cornell potential (cor)**

  The Cornell potential is given by [104]:

  $$V(\tilde{r}) = -\frac{k}{\tilde{r}} + \frac{\tilde{r}}{a^2} \tag{57}$$

  with the parameters $k = 0.52$, $a = 2.34$ GeV^{-1} and the masses $m_c = 1.84$ GeV and $m_b = 5.17$ GeV.

- **Logarithmic potential (log)**

  The logarithmic potential is written as [105]:

  $$V(\tilde{r}) = -0.6635 \text{ GeV} + (0.733 \text{ GeV})\log(\tilde{r} \cdot 1 \text{ GeV}) \tag{58}$$

  with masses $m_c = 1.5$ GeV and $m_b = 5.0$ GeV.

- **Harmonic oscillator potential (osc)**

  The harmonic oscillator potential has the following form:

$$V(\tilde{r}) = \frac{1}{2} m_q \omega^2 \tilde{r}^2, \quad \omega = \frac{1}{2} \left(M_{2S} - M_{1S} \right) , \tag{59}$$

  which leads to a wave function that exhibits a straightforward Gaussian profile. In this model, the charm and bottom quark masses are taken as $m_c = 1.4$ GeV and $m_b = 4.2$ GeV. The ω parameter is fixed in 0.3 GeV for charmonia and 0.28 for bottomonia.

- **Power-law potential (pow)**

  This potential is parameterized by a power-law function expressed as [106]:

$$V(\tilde{r}) = -6.41 \text{ GeV} + (6.08 \text{ GeV})(\tilde{r} \cdot 1 \text{ GeV})^{0.106} , \tag{60}$$

  with $m_c = 1.334$ GeV and $m_b = 4.721$ GeV.

3.2 HEAVY VECTOR MESON NUMERICAL RESULTS

In the last few years, the amount of information regarding vector meson exclusive production has become more abundant thanks to the contributions from high-energy accelerators such as the LHC. Considering that this collider will pass through future updates and possibly an expansion of its collider complex, it is possible that more observables related to these particles will be obtained. This, in turn, motivates the search for realistic models capable of accurately describing this process. Furthermore, the recent data published by the LHCb [30] and CMS [107] collaborations on the cross section for the production of J/ψ, ψ', and $\Upsilon(1S)$ has motivated the use of the previously described formalism in the calculation of cross sections for the process $\gamma p \to Vp$, with $V = \psi(nS), \Upsilon(nS)$ for $n = 1, 2$.

3.2.1 Heavy vector meson total cross section

In this subsection, it will be presented numerical results for the total integrated cross section for the $\gamma p \to Vp$ process for the heavy vector mesons: $V = \psi(1S)$, $\psi(2S)$, $\Upsilon(1S)$ and $\Upsilon(2S)$; and for real photons ($Q^2 = 0$), which are represented by γ. First, Fig. 9 shows the total cross section for $\psi(1S)$ (left) and $\psi(2S)$ (right) photoproduction as a function of the photon-proton center of mass energy W. In this analysis, five different potential models were used to describe the quark-antiquark interaction, along with the GBW model for the dipole cross section. It is worth mentioning that the KST model provides extremely similar results to the GBW, making its presentation unnecessary. The results were compared to the H1 [87], ZEUS [89], ALICE [7] and LHCb [30] data as well as to fixed target experiments performed at Fermilab [108, 109, 110]. It is possible to observe that all five potentials describe very well the available data for both $\psi(1S)$ and $\psi(2S)$ in all considered energy range.

Figure 9 – Total cross section as a function of the γp center of mass energy W for $\psi(1S)$ (left) and $\psi(2S)$ (right) photoproduction. The results were obtained with the GBW model and compared to the available data from H1 [87], ZEUS [89], ALICE [7] and LHCb [30], as well as from the fixed target experiments at Fermilab [108, 109, 110].

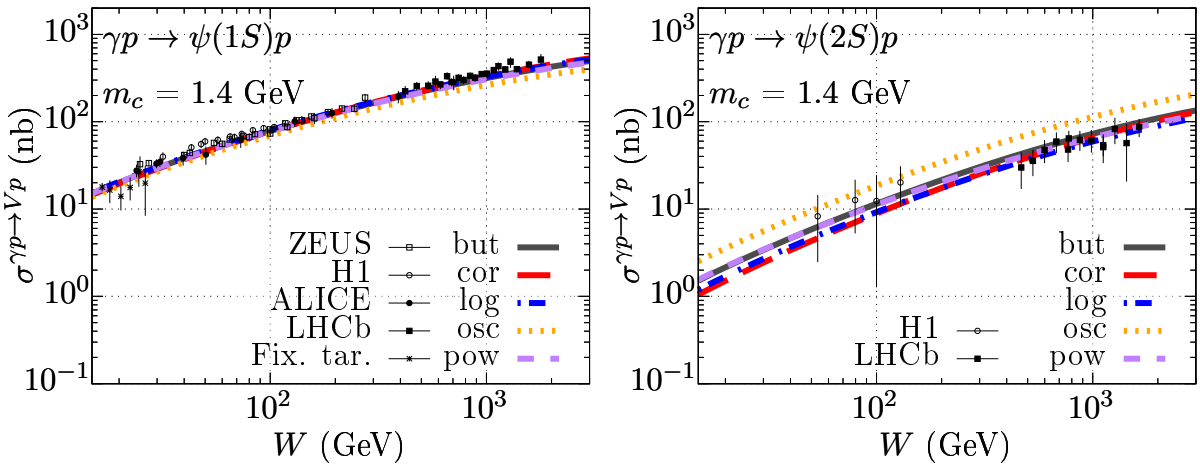

Source: Elaborated by the author and published in [11].

Figure 10 – Total cross section as a function of the γp center of mass energy W for $\Upsilon(1S)$ (left) and $\Upsilon(2S)$ (right) photoproduction. The results were obtained with the KST model and compared to the available data from CMS [107], H1 [111], ZEUS [112, 113] and LHCb [114].

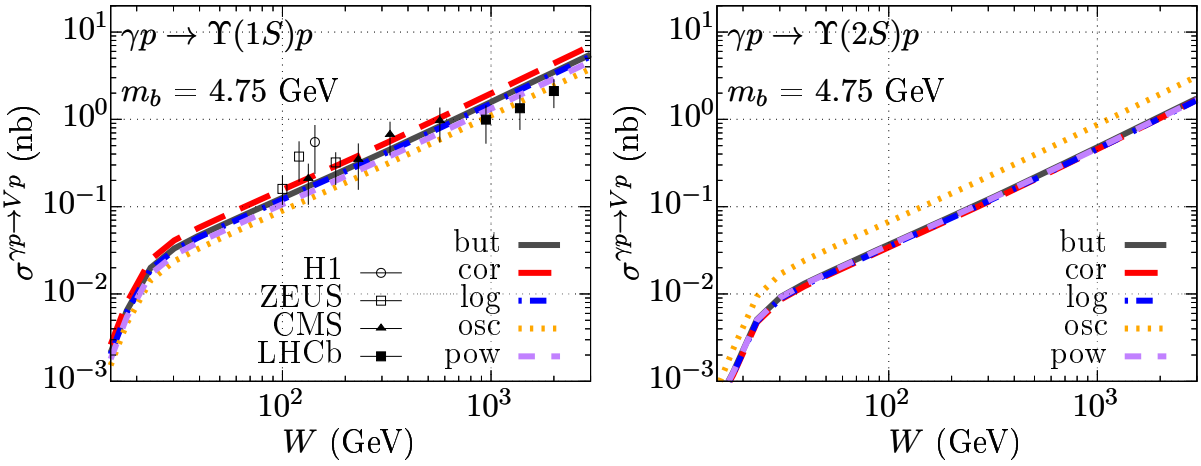

Source: Elaborated by the author and published in [11].

It is worth mentioning that the original GBW model [46] was employed in the calculations. This choice is supported by an independent analysis comparing the results obtained with the original model and the more recently fitted version [48], which reveals that the differences between the results obtained with these two GBW parameterizations are insignificant. However, a detailed examination reveals that the original fit gets closer to the experimental data, mostly in the high W region.

Fig. 10 presents the numerical results for the total integrated cross section for the diffractive photoproduction of $\Upsilon(1S)$ (left) and $\Upsilon(2S)$ (right) as a function of W. Analogously

to the previous figure, the bottomonia wave functions are calculated with the aforementioned five different potentials. The Υ ground state results are compared to CMS [107], H1 [111], ZEUS [112, 113] and LHCb [114] available data. In this figure, the KST model was used for the dipole cross section since it provides a better description for the Υ photoproduction data. It is worth to note that all five potentials generate comparatively good results for the $\Upsilon(1S)$ data, in the considered energy range. These two facts unleash the utilization of the same setup to obtain predictions for the excited state $\Upsilon(2S)$ total cross sections.

A detailed survey of Fig. 10 reveals that the differences between the cross sections for the ground and the excited states reduce with the W increase for all potentials. In the oscillator potential case, the $\Upsilon(1S)$ result is approximately 22% bigger than the $\Upsilon(2S)$ one, at $W = 1000$ GeV, which has the smallest difference when compared to the other potentials. The observation that the oscillator potential presents very close results for the ground and the excited states can be explained by the similar contribution of the two wave functions at small-r, which does not occur with the other potentials. Therefore, since the main contribution to the total cross section comes from the small-r region, this effect is particularly relevant for the Υ states.

3.2.2 Heavy vector meson t-distributions

Besides the total cross section, it is possible, as was seen previously in the text, to calculate differential cross sections that depend on the proton transferred momentum t. Nevertheless, the evaluation of these observables is only possible through the utilization of impact parameter-dependent dipole cross section parameterizations. The GBW and KST models, which were used in the previous results, do not have this dependence, and the non-integrated forms for these models found in the literature [115] were not effective in the available data description. It is expected that the factorized exponential form (Eq. 27) works in the small $|t|$ regime, however, this assumption was used in this work only for evaluating total cross sections. Hence, more parameterizations were tested, and it was noticed that the best data description was obtained with the famous "bSat" model and the recent solution of the BK equation. For this reason, it was decided to show the results with both models. Moreover, it is worth mentioning that the two parameterizations were originally fitted to data with the skewness factor to consider different momentum fractions carried by the gluons, thus, its inclusion is indispensable in our calculations.

Fig. 11 shows the differential cross section for the photoproduction of $J/\psi \equiv \psi(1S)$ (upper curves) and $\psi(2S)$ (lower curves) as a function of the transferred momentum $|t|$ at $W = 100$ GeV (left) and $W = 55$ GeV (right). The results were obtained with the solution of the BK equation and the five potential models described previously in the text. The charmonium ground state curves were compared with the few available experimental data from H1 collaboration [87, 88], which was very well described. It is worth to note that the inclination of the curve is almost constant and arises from the almost exponential behavior of

Figure 11 – Differential cross section for $\psi(1S)$ (upper curves) and $\psi(2S)$ (lower curves) photoproduction as a function of $|t|$ obtained using the numerical solution of the BK equation obtained in Ref. [63], for $W = 100$ GeV (left) and $W = 55$ GeV (right). The results are presented for five different potential models. The $\psi(1S)$ results are compared to data from H1 Collaboration [87, 88].

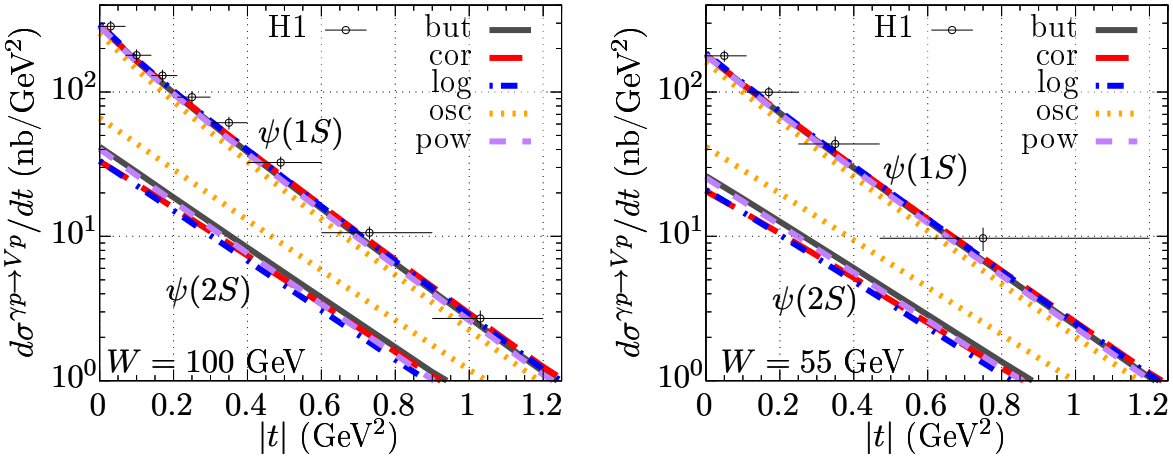

Source: Elaborated by the author and published in [38].

the dipole amplitude with respect to the impact parameter, which agrees with the data.

Figure 12 – Predictions for the differential cross section for $\Upsilon(1S)$ (left) and $\Upsilon(2S)$ (right) photoproduction as a function of $|t|$ obtained using the numerical solution of the BK equation obtained in Ref. [63], for $W = 120$ GeV. The results are presented for five different potential models.

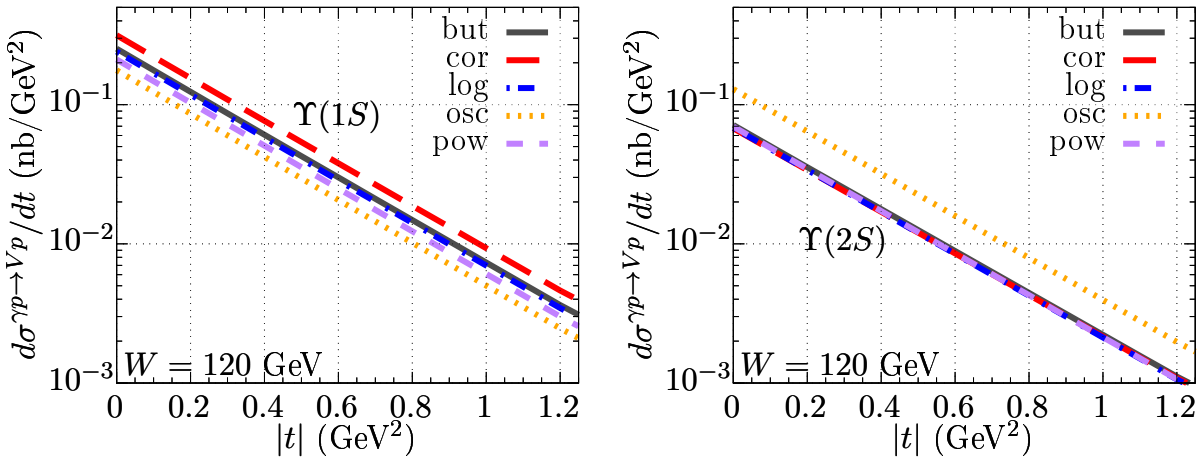

Source: Elaborated by the author and published in [38].

Predictions for the differential cross section for the $\Upsilon(1S)$ (left) and $\Upsilon(2S)$ (right) photoproduction are presented in Fig. 12 as a function of $|t|$. In the same way as the previous figure, the solution of the BK equation was used together with the five $q\bar{q}$ interaction potentials, however in this case it was calculated for $W = 120$ GeV. The ground and excited state results are shown in two different plots because of the closeness of the oscillator potential results. As was aforementioned, this occurs because the two wave functions have a r-dependence very

similar for small r values. Thus, since this domain has a big contribution to the amplitude integrals for the Υ states production, the results for $\Upsilon(1S)$ and $\Upsilon(2S)$ become very close.

Figure 13 – Differential cross section for $\psi(1S)$ (upper curves) and $\psi(2S)$ (lower curves) photoproduction as a function of $|t|$ obtained with the "bSat" model, for $W = 100$ GeV (left) and $W = 55$ GeV (right). The results are presented for five different potential models. The $\psi(1S)$ results are compared to data from H1 Collaboration [87, 88].

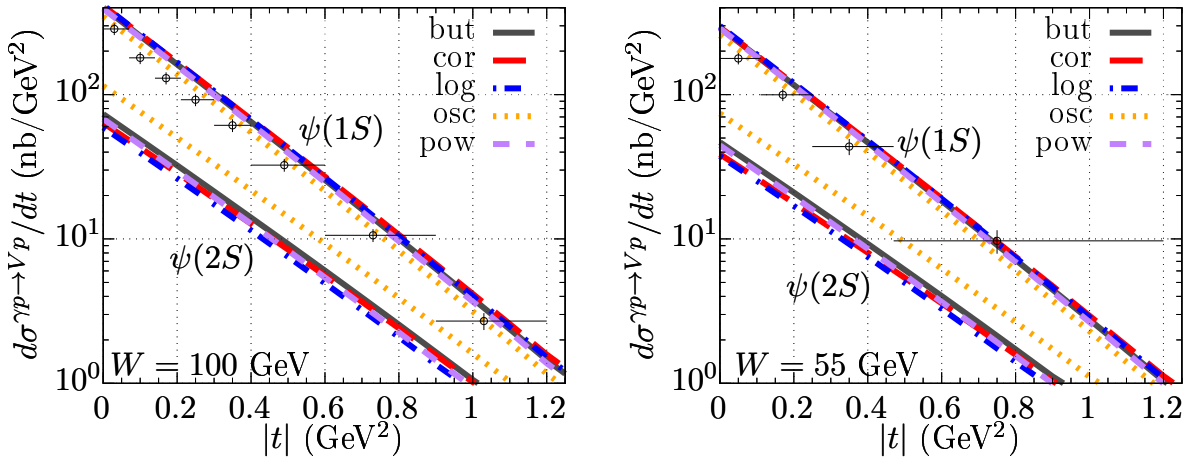

Source: Elaborated by the author and published in [38].

Last but not least, Figs. 13 and 14 are analogous to Figs. 11 and 12, except by the fact that they are computed with the "bSat" model, instead of the BK solution. Fig. 13 shows that the "bSat" model also gives a reasonable description of the H1 data, thus, even if this description is not as good as the one obtained with the BK solution, it was decided to show it due to its great popularity in the literature. A comparison between the results obtained with the two models can be found in Fig. 15, where one can see that both curves are mostly inside the experimental error bars for both $W = 100$ GeV (left) and $W = 55$ GeV (right). The biggest divergence happens at small-t values, where the "bSat" overestimates the data.

3.3 LIGHT VECTOR MESON WAVE FUNCTION

The method of obtaining the heavy vector meson wave function by solving the non-relativistic Schrödinger equation in a rest frame relies on the large quark masses which make them have non-relativistic speeds. However, in the light vector mesons case, the light quark masses are not high enough to treat them non-relativistically. Besides that, it cannot be considered a hard scale, provoking the emergence of non-perturbative effects [26, 116]. Thus, the difficult goal of finding the light vector meson wave functions reduces to discovering a way to deal with the relativistic strongly coupled regime of QCD at large distances.

The AdS/CFT correspondence establishes a relationship between a gravitational theory in $(d+1)$-dimensional anti-de-Sitter (AdS) space and a conformal field theory (CFT) in d-dimensional Minkowski space. This correspondence led to what is called Brodsky-de Téramond

Figure 14 – Predictions for the differential cross section for $\Upsilon(1S)$ (left) and $\Upsilon(2S)$ (right) photoproduction as a function of $|t|$ obtained with the "bSat" model, for $W = 120$ GeV. The results are presented for five different potential models.

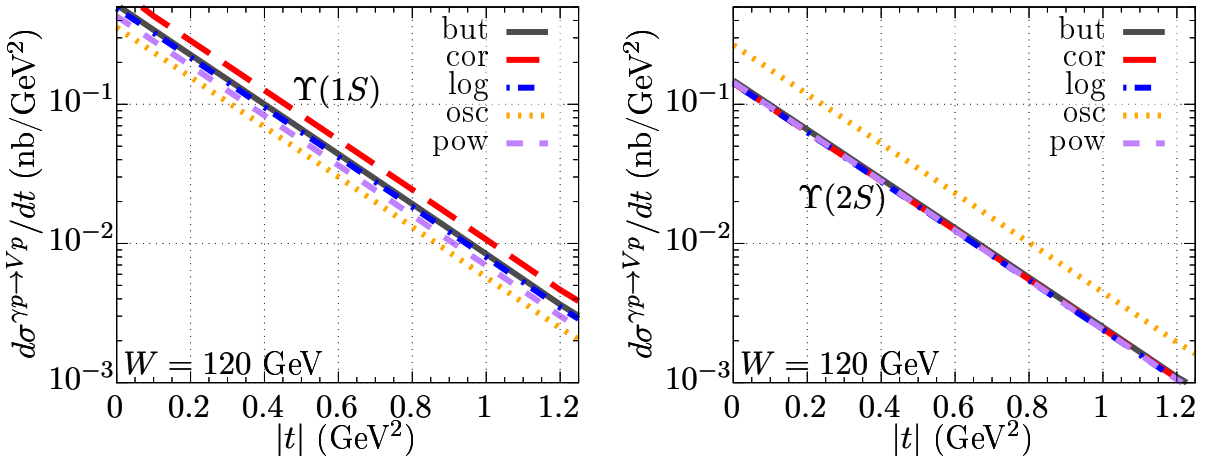

Source: Elaborated by the author and published in [38].

Figure 15 – Differential cross section for $\psi(1S)$ photoproduction as a function of $|t|$ found using the Buchmüller-Tye potential with BK and "bSat" models for $W = 100$ GeV (left) and $W = 55$ GeV (right). The $\psi(1S)$ results are compared to data from H1 Collaboration [87, 88].

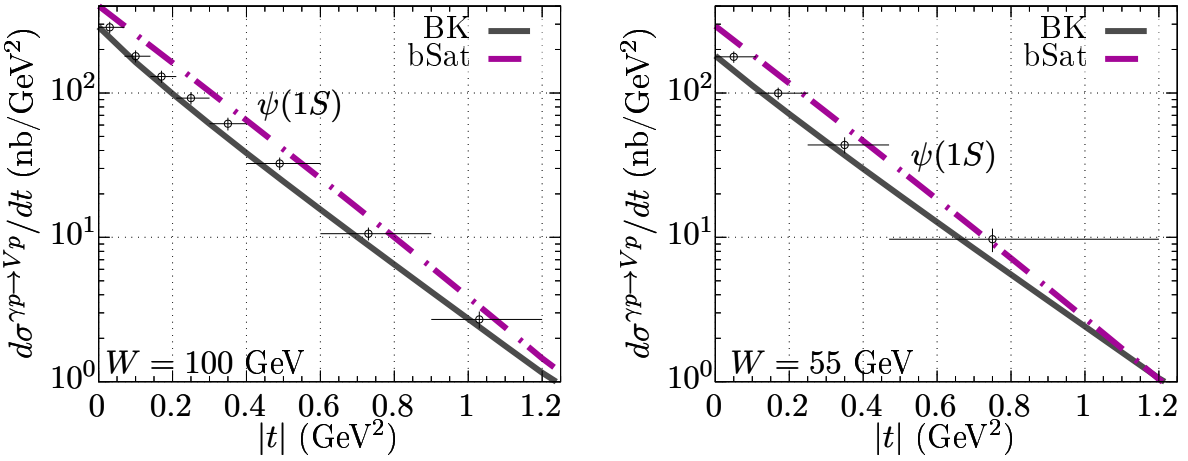

Source: Elaborated by the author and published in [38].

semiclassical model, which offers a framework for studying the strongly coupled QCD and sheds light on its perturbative dynamics. It is an explicit manifestation of the holographic principle[1], and enables the calculation of physical observables in a strongly coupled theory through a weakly coupled classical gravity theory [12].

Five-dimensional anti-de Sitter space (AdS_5) possesses 15 isometries[2], which yields the symmetry of the conformal group Conf($\mathbb{R}^{1,3}$) to the Minkowski-spacetime theory. The conformal symmetry implies that the mass spectrum is continuous or that all masses are zero

[1] The holographic principle states that a gravitational system is equivalent to a non-gravitational one in one lower dimension [117, 118]. In this correspondence, the former is denoted as the holographic dual, or gravity dual, of the lower-dimensional system.

[119]. Thus, the classical QCD lagrangian with massless quarks preserves conformal symmetry. However, the existence of quantum effects introduces an energy scale μ, which breaks the conformal invariance, since it separates the space into two regions: the asymptotic freedom perturbative region and the confined non-perturbative one. The problem does not come from the perturbative region, since the small coupling makes it almost scale-invariant, but it comes from the non-perturbative part. The good news is that there are evidences [120, 121, 122, 123] that point out that the strong coupling does not grow indefinitely but becomes constant at small μ. This can be physically treated as an infrared cut-off originated from the confinement effect.

To maintain the correct correspondence between QCD and AdS$_5$ spaces, it is necessary to incorporate confinement into the gravitational space. This can be achieved by imposing a boundary condition on the holographic variable z. In the "soft-wall" model [124], a smooth infrared cut-off is introduced by including a dilaton[3] background field $\varphi(z) = \kappa^2 z^2$, whose form is chosen to reproduce the Regge behavior of the hadronic mass spectrum. After this consideration, one can proceed with the mapping of the vector meson wave function in AdS$_5$ to its corresponding expression in QCD space. For this task, it will be necessary to write the wave equation in both spaces, which will be done right below.

3.3.1 Wave equation in AdS$_5$ space

In this section, the derivation of the hadronic bound-state wave equations in the anti-de Sitter space will be carried out following the Brodsky-de Téramond prescription presented in [12, 126]. In their formulation, for a general purpose, the equations will be obtained in a $(d+1)$-dimensional AdS space. Then, in the comparison with the equations obtained in the QCD physical space, one takes $d = 4$.

The coordinates in the $(d+1)$-dimensional anti-de Sitter space can be expressed as a combination of the coordinates in the d-dimensional Minkowski space, denoted by x^μ, and the holographic variable, denoted by z. This combination can be represented by $x^M = (x^\mu, z = x^d)$, where $M, N = 1, ..., d$ are indices corresponding to the higher-dimensional AdS space, and $\mu, \nu = 0, ..., d-1$ are indices corresponding to the Minkowski flat space. Using Poincaré coordinates - which means taking $x^0 = t, x^i$ (with $i = 1, ..., d-1$), and $x^d \equiv z$ - the conformal AdS metric can be written as

$$ds^2 = g_{MN} dx^M dx^N = \frac{R^2}{z^2}(\eta_{\mu\nu} dx^\mu dx^\nu - dz^2). \tag{61}$$

In this equation, g_{MN} is the metric tensor of the AdS space and $\eta_{\mu\nu} = \mathsf{diag}(1, -1, -1, -1)$ is the metric tensor of the Minkowski space.

[2] Isometry is, roughly, a transformation between two spaces that preserves distance.

[3] Dilaton is a scalar field that appears in all string theories. Its existence and characteristics come from the symmetries of the theory [125].

The first step to find the wave functions for a bound state with integer spin J is writing the action in AdS_{d+1} space considering the effect of the dilaton background field $\varphi(z)$:

$$S = \int d^d x dz \sqrt{g} e^{\varphi(z)} g^{N_1 N_1'} \cdots g^{N_J N_J'} \Big(g^{MM'} D_M \Phi^*_{N_1 \ldots N_J} D_{M'} \Phi_{N_1' \ldots N_J'} - \mu^2 \Phi^*_{N_1 \ldots N_J} \Phi_{N_1' \ldots N_J'} + \cdots \Big) . \tag{62}$$

In this equation, $\Phi_{N_1 \ldots N_J}$ represents the J-spin fields, $\sqrt{g}$ is the square root of the modulus of the determinant of the metric tensor g_{MN}, D_M is the covariant derivative, and μ is the AdS mass. The three dots at the end of the Eq. 62 represent terms with different indices contractions. In fact, all terms with indices along the z-direction must vanish,

$$\Phi_{z N_2 \ldots N_J} = 0 , \tag{63}$$

because physical hadrons have only polarization indices along the 3+1 physical coordinates. This implies that only the terms with $\Phi_{\nu_1, \nu_2 \ldots \nu_J}$ will survive.

A convenient way of conducting the conformal symmetry breaking consists in including a z-dependence in an effective AdS mass $\mu_{eff}(z)$ and rewriting Eq. 62 as the effective action:

$$S_{eff} = \int d^d x dz \sqrt{g} e^{\varphi(z)} g^{N_1 N_1'} \cdots g^{N_J N_J'} \Big(g^{MM'} D_M \Phi^*_{N_1 \ldots N_J} D_{M'} \Phi_{N_1' \ldots N_J'} - \mu^2_{eff}(z) \Phi^*_{N_1 \ldots N_J} \Phi_{N_1' \ldots N_J'} \Big) . \tag{64}$$

The terms with different indices contractions omitted in Eq. 62 are now contained into $\mu_{eff}(z)$. The z-dependence of this function is unknown at the present moment, however, it will be determined by the meticulous mapping of the AdS space into the QCD one.

The equations of motion will be defined by the Euler-Lagrange equations:

$$\frac{\delta S_{eff}}{\delta \Phi^*_{\nu_1 \nu_2 \cdots \nu_J}} = 0 \tag{65}$$

$$\frac{\delta S_{eff}}{\delta \Phi^*_{z N_2 \cdots N_J}} = 0. \tag{66}$$

Nevertheless, prior to their evaluation, it is worth noting that the presence of covariant derivatives in the action (Eqs. 62 and 64) leads to complicated expressions with several sums that are difficult to be treated. A solution to this predicament can be found in Appendix D of [12], where the authors go to a local inertial frame where the covariant derivatives become partial derivatives, thereby simplifying the expressions. Thus, the evaluation of Eq. 65 results in the equation of motion for the AdS fields with polarizations in the physical directions:

$$\left[\partial_\mu \partial^\mu - \frac{z^{d-1-2J}}{e^{\varphi(z)}} \partial_z \left(\frac{e^{\varphi(z)}}{z^{d-1-2J}} \partial_z \right) + \frac{(mR)^2}{z^2} \right] \Phi_{\nu_1 \ldots \nu_J} = 0 , \tag{67}$$

with

$$(mR)^2 = (\mu_{eff}(z) R)^2 - J z \varphi'(z) + J(d - J + 1), \tag{68}$$

whereas Eq. 66 provides kinematical constraints which eliminate lower spin states $J-1, J-2, ...$ from the symmetric tensor $\Phi_{\nu_1\nu_2\cdots\nu_J}$:

$$\eta^{\mu\nu}\partial_\mu\Phi_{\nu\nu_2\cdots\nu_J} = 0, \quad \eta^{\mu\nu}\Phi_{\mu\nu\nu_3\cdots\nu_J} = 0. \tag{69}$$

In order to establish a connection between the equation of motion in AdS_5 and physical QCD spaces, one needs to rewrite Eq. 67 as a one-dimensional equation of motion. This can be done by considering hadronic states with momentum P and a z-independent spinor $\epsilon_{\nu_1\cdots\nu_J}(P)$. This bound states can be represented by a z-dependent wave function $\Phi_J(z)$ and a plane wave propagating in the physical space-time:

$$\Phi_{\nu_1\cdots\nu_J}(x,z) = e^{iP\cdot x}\Phi_J(z)\epsilon_{\nu_1\cdots\nu_J}(P)\,. \tag{70}$$

Inserting this into Eq. 67 and considering the invariant hadron mass $P_\mu P^\mu = M^2$, one obtains the hadronic bound-state wave equation in AdS_5 space:

$$\left[-\frac{z^{d-1-2J}}{e^{\varphi(z)}}\partial_z\left(\frac{e^{\varphi(z)}}{z^{d-1-2J}}\partial_z\right) + \frac{(mR)^2}{z^2}\right]\Phi_J(z) = M^2\Phi_J(z)\,. \tag{71}$$

3.3.2 Wave equation in QCD space

The challenge of finding the light vector meson wave function in the four-dimensional QCD space-time lies in the fact that the small quark masses prevent the identification of a rest frame where the Schrödinger equation can be applied. One way to contour this problem relies on using light-front quantization, since it provides a relativistic and frame-independent framework to solve bound-state wave equations. This approach has the advantage of not running into the multiparticle problem of boosting a hadronic state from its rest frame to a moving one, at an ordinary fixed time (x_0).

The idea of working in the light-front frame[4] was formulated by Dirac [127], who realized that the advantage of defining the states at the fixed light-front time $x^+ = x^0 + x^3$ is that the boost operators are kinematic generators of the Lorentz transformations, which means that they do not depend on the system dynamics and make the hadron description independent of the observer's frame. Thus, for a hadron with four-momentum $P^\mu = (P^+, P^-, \boldsymbol{P}_\perp)$ (Appendix D), one can construct a LF (light-front) Lorentz invariant Hamiltonian $H_{LF} = P^+P^- - \boldsymbol{P}_\perp^2$, whose eigenvalues M^2 and eigenstates $|\psi(P)\rangle$ can be obtained from the equation

$$H_{LF}|\psi(P)\rangle = M^2|\psi(P)\rangle\,, \tag{72}$$

where M^2 defines the hadron mass spectrum and $|\psi(P)\rangle$ gives the hadron wave function.

Having established a procedure for deriving the wave equations within a relativistic framework, one can now focus on describing the dynamics of QCD using the LF variables. For

[4] The expression "light-front" comes from the idea that a measurement in this frame can be likened to a captured image with a flash camera. This image portrays the object as it appears when illuminated by the front of the light wave from the flash.

this, one can start with the invariant QCD Lagrangian:

$$\mathcal{L}_{\rm QCD} = \bar{\psi}\left(i\gamma^\mu D_\mu - m\right)\psi - \frac{1}{4}G^a_{\mu\nu}G^{a\mu\nu}\,, \tag{73}$$

where $D_\mu = \partial_\mu - ig_s A^a_\mu T^a$ is the covariant derivative and $G^a_{\mu\nu} = \partial_\mu A^a_\nu - \partial_\nu A^a_\mu + g_s c^{abc} A^b_\mu A^c_\nu$ is the gluon field strength tensor. In these equations, T^c are the color matrices (related to the Gell-Mann matrices), c^{abc} are structure constants, g_s is the coupling constant of the strong force, and a, b, c are color indices.

One can obtain from the Lagrangian (Eq. 73) expressions for the four-momentum components $P^\mu = (P^+, P^-, \boldsymbol{P}_\perp)$ in terms of the $+$ component of the quark field ψ_+ and the transverse component of the gluon field $\boldsymbol{A}_\perp$ quantized on the LF frame with fixed LF time x^+ [128, 129]:

$$\begin{aligned} P^- = {} & \frac{1}{2}\int dx^- d^2\mathbf{x}_\perp \left(\bar{\psi}_+\gamma^+ \frac{m^2 + (i\nabla_\perp)^2}{i\partial^+}\psi_+ - A^{a\mu}\left(i\nabla_\perp\right)^2 A^a_\mu\right) \\ & + g_s\int dx^- d^2\mathbf{x}_\perp \bar{\psi}_+\gamma^\mu T^a \psi_+ A^a_\mu + \\ & + \frac{g_s^2}{4}\int dx^- d^2\mathbf{x}_\perp c^{abc}c^{ade}A^b_\mu A^c_\nu A^{d\mu}A^{e\nu} \\ & + \frac{g_s^2}{2}\int dx^- d^2\mathbf{x}_\perp \bar{\psi}_+\gamma^+ T^a\psi_+ \frac{1}{\left(i\partial^+\right)^2}\bar{\psi}_+\gamma^+ T^a\psi_+ \\ & + \frac{g_s^2}{2}\int dx^- d^2\mathbf{x}_\perp \bar{\psi}_+\gamma^\mu T^a A^a_\mu \frac{\gamma^+}{i\partial^+}\left(T^b A^b_\nu \gamma^\nu \psi_+\right)\,, \end{aligned} \tag{74}$$

$$P^+ = \int dx^- d^2\mathbf{x}_\perp \left(\bar{\psi}_+\gamma^+ i\partial^+\psi_+ - A^{a\mu}\left(i\partial^+\right)^2 A^a_\mu\right)\,, \tag{75}$$

and

$$\mathbf{P}_\perp = \frac{1}{2}\int dx^- d^2\mathbf{x}_\perp \left(\bar{\psi}_+\gamma^+ i\nabla_\perp\psi_+ - A^{a\mu}i\partial^+ i\nabla_\perp A^a_\mu\right)\,. \tag{76}$$

Now, it is evident that the operators P^+ and $\boldsymbol{P}_\perp$ are kinetic generators, since there is no interaction term in Eqs. 75 and 76. The fact that the operator P^- has interaction terms (Eq. 74), makes it responsible for the evolution of the system. This type of operator is classified as dynamic generator.

The quark and the gluon fields can be written in terms of particle creation and particle annihilation operators:

$$\psi_+\left(x^-, \mathbf{x}_\perp\right)_\alpha = \sum_\lambda \int_{q^+>0} \frac{dq^+}{\sqrt{2q^+}}\frac{d^2\mathbf{q}_\perp}{(2\pi)^3}\left[b_\lambda(q)u_\alpha(q,\lambda)e^{-iq\cdot x} + d^\dagger_\lambda(q)v_\alpha(q,\lambda)e^{iq\cdot x}\right], \tag{77}$$

and

$$\mathbf{A}_\perp\left(x^-, \mathbf{x}_\perp\right) = \sum_\lambda \int_{q^+>0} \frac{dq^+}{\sqrt{2q^+}}\frac{d^2\mathbf{q}_\perp}{(2\pi)^3}\left[a(q)\vec{\epsilon}_\perp(q,\lambda)e^{-iq\cdot x} + a^\dagger(q)\vec{\epsilon}^*_\perp(q,\lambda)e^{iq\cdot x}\right]\,, \tag{78}$$

where u and v are LF spinors and $a^\dagger(q)$, $b^\dagger(q)$, and $c^\dagger(q)$ are respectively the quark, antiquark, and gluon creation operators. This expansion will be useful in the next step, when the hadron state will be expanded on a LF Fock basis.

The hadronic state $|\psi(P)\rangle$, that appears in Eq. 72, can be expanded into multiparticle Fock states $|n\rangle$ constituted by free partons

$$|\psi(P)\rangle = \sum_n \psi_n |n\rangle \,, \tag{79}$$

which are constructed by the application of creation operators to the vacuum state $|0\rangle$ (for example, the one-quark state is $|q\rangle = \sqrt{2q^+} b^\dagger(q)|0\rangle$). The advantage of this approach is that the coefficients of the Fock expansion do not depend on the hadron momentum P^+ and $\boldsymbol{P}_\perp$; they only depend on the relative partonic coordinates, which are: the longitudinal momentum fraction carried by the i^{th}-parton $\beta_i = k_i^+/P^+$, the parton transverse momentum $k_{\perp i}$, and the projection of its spin along the z direction λ_i. Thus, the wave function $\psi_n(\beta_i, k_{\perp i}, \lambda_i)$ is frame-independent and relates the hadron state to its quark and gluon state constituents.

Now, one has all the pieces to compute M^2 from the matrix element

$$\left\langle \psi\left(P'\right) \left| H_{LF}(P^+, P^-, \boldsymbol{P}_\perp) \right| \psi(P) \right\rangle = M^2 \left\langle \psi\left(P'\right) \mid \psi(P) \right\rangle \,. \tag{80}$$

For this arduous task, the initial and final hadronic states need to be expanded into the Fock basis (as presented in Eq. 79) and the LF Hamiltonian must be written in terms of the creation and annihilation operators, by inserting Eqs. 77 and 78 into Eqs. 74, 75, and 76, and substituting it into $H_{LF} = P^+P^- - \boldsymbol{P}_\perp^2$. The result is the following [130, 13]:

$$M^2 = \sum_n \int \left[d\beta_i\right] \left[d^2\mathbf{k}_{\perp i}\right] \sum_{a=1}^{n} \left(\frac{\mathbf{k}_{\perp a}^2 + m_a^2}{\beta_a} \right) \left|\psi_n\left(\beta_i, \mathbf{k}_{\perp i}\right)\right|^2 + \text{ (interactions) } \,, \tag{81}$$

which also includes similar terms referring to antiquarks and gluons ($m_g = 0$). The phase space is normalized to a Dirac δ-function, which leads to the expression [12, 130]:

$$\left[d\beta_i d^2k_{\perp i}\right] = \delta\left(1 - \sum_{j=1}^{N_n} \beta_j\right) \delta^{(2)}\left(\sum_{j=1}^{N_n} \vec{k}_{\perp j}\right) d\beta_1 \ldots d\beta_{N_n} d^2k_{\perp 1} \ldots d^2k_{\perp N_n} \,. \tag{82}$$

It is convenient to transform Eq. 81 from the momentum space to the impact parameter space. This is accomplished through the utilization of a Fourier expansion, which relates each of the $n-1$ transversal momentum coordinates with its respective transverse impact parameter variable $\boldsymbol{b}_{\perp j}$. The resulting equation is

$$M^2 = \sum_n \prod_{j=1}^{n-1} \int d\beta_j d^2\mathbf{b}_{\perp j} \psi_n^*\left(\beta_j, \mathbf{b}_{\perp j}\right) \sum_{a=1}^{n} \left(\frac{-\nabla_{\mathbf{b}_{\perp a}}^2 + m_a^2}{\beta_a} \right) \psi_n\left(\beta_j, \mathbf{b}_{\perp j}\right) + \text{ (interactions) } \,. \tag{83}$$

In order to obtain a solution for Eqs. 81 and 83, a simplification is implemented to reduce the multiparticle problem to a single variable problem. Therefore, the first step is to take the limit of $m_q \to 0$ in Eqs. 81 and 83. Subsequently, the invariant mass of the constituents in each n-particle Fock state,

$$M_n^2 = \left(\sum_{i=1}^{n} k_i^\mu\right)^2 = \left(\sum_{i=1}^{n} k_i^+\right)\left(\sum_{i=1}^{n} k_i^-\right) - \left(\sum_{i=1}^{n} \boldsymbol{k}_{\perp \boldsymbol{i}}\right)^2 = \sum_{i=1}^{n} \frac{\mathbf{k}_{\perp i}^2 + m_i^2}{\beta_i}, \tag{84}$$

is identified as the key variable that encodes all bound state dynamics. This simplification is named by Brodsky and de Téramond as semiclassical approximation.

Considering that the focus of this project is the study of vector mesons, it is inherent to examine Eqs. 81 and 83 for the case of $n = 2$, which leads to equations:

$$\begin{aligned} M^2 &= \int_0^1 d\beta \int \frac{d^2\mathbf{k}_\perp}{16\pi^3} \frac{\mathbf{k}_\perp^2}{\beta(1-\beta)} \left|\psi\left(\beta, \mathbf{k}_\perp\right)\right|^2 + (\text{ interactions }) \\ &= \int_0^1 \frac{d\beta}{\beta(1-\beta)} \int d^2\mathbf{b}_\perp \psi^*\left(\beta, \mathbf{b}_\perp\right) \left(-\nabla_{\mathbf{b}_\perp}^2\right) \psi\left(\beta, \mathbf{b}_\perp\right) + \text{ (interactions) } . \end{aligned} \tag{85}$$

In this instance, the invariant mass is $M_{qq}^2 = \frac{\mathbf{k}_\perp^2}{\beta(1-\beta)}$. And the corresponding variable on the impact-parameter space is the invariant separation of the $q\bar{q}$ pair $\zeta^2 = \beta(1-\beta)\mathbf{b}_\perp^2$. Consequently, as a first approximation, one can factorize the orbital and the longitudinal dependencies on the vector meson wave function:

$$\psi(\beta, \zeta, \varphi) = e^{iL\varphi} X(\beta) \frac{\phi(\zeta)}{\sqrt{2\pi\zeta}}. \tag{86}$$

In this case, $\phi(\zeta)$ stores all information about the hadronic dynamics, and $X(\beta) = \sqrt{\beta(1-\beta)}$ is obtained by mapping form factor calculations from AdS_5 to QCD space [131]. The normalization of these quantities is given by:

$$\begin{aligned} \langle \phi \mid \phi \rangle &= \int d\zeta \phi^2(\zeta) = 1 \\ \langle X \mid X \rangle &= \int_0^1 d\beta \beta^{-1}(1-\beta)^{-1} X^2(\beta) = 1 \, . \end{aligned} \tag{87}$$

After evaluating the β and the angular integrations in Eq. 85 (with the Laplacian written in polar coordinates), the squared hadron mass is given by:

$$M^2 = \int d\zeta \, \phi^*(\zeta) \sqrt{\zeta} \left(-\frac{d^2}{d\zeta^2} - \frac{1}{\zeta}\frac{d}{d\zeta} + \frac{L^2}{\zeta^2} \right) \frac{\phi(\zeta)}{\sqrt{\zeta}} + \int d\zeta \, \phi^*(\zeta) U(\zeta) \phi(\zeta) \, . \tag{88}$$

In this equation, the effective potential $U(\zeta)$ encompasses all the interaction terms of the QCD Hamiltonian and describes confinement at some infrared scale. Thus, after all these considerations, one finds that the wave equation in QCD space is given by:

$$\left(-\frac{d^2}{d\zeta^2} - \frac{1-4L^2}{4\zeta^2} + U(\zeta) \right) \phi(\zeta) = M^2 \phi(\zeta). \tag{89}$$

3.3.3 Holographic mapping

Now that the wave equations were obtained in both AdS and QCD spaces, it is possible to take advantage of their very similar structure to make a connection between the hadronic modes in AdS and the vector meson QCD wave function. Upon initial inspection, it becomes evident that both equations have the same eigenvalue M^2 and are frame-independent. However,

for an exact comparison, the spin-J hadronic modes have to be modified to put Eq. 71 in the same relativistic Schrödinger-like form[5] of Eq. 89. Thus, they will be written as:

$$\Phi_J(z) = \left(\frac{R}{z}\right)^{J-(d-1)/2} e^{-\varphi(z)/2}\phi_J(z)\,. \tag{90}$$

The substitution of the previous form into the d-dimensional wave equation in AdS space equation (71) results in the following expression:

$$\left\{-\frac{d^2}{dz^2} + \frac{\varphi''(z)}{2} + \frac{\varphi'(z)^2}{4} + \frac{\varphi'(z)}{2}\frac{(2J-d+1)}{z} + \frac{(d-2J+1)\,(d-2J-1)}{4z^2} + \frac{(mR)^2}{z^2}\right\}\phi_J(z) = M^2\phi_J(z)\,, \tag{91}$$

which for $d = 4$ is

$$\left\{-\frac{d^2}{dz^2} + \frac{\varphi''(z)}{2} + \frac{\varphi'(z)^2}{4} + \frac{\varphi'(z)}{2}\frac{(2J-3)}{z} + \frac{(2J-5)\,(2J-3)}{4z^2} + \frac{(mR)^2}{z^2}\right\}\phi_J(z) = M^2\phi_J(z)\,. \tag{92}$$

This equation has precisely the same form as Eq. 71, hence, the total mapping of the AdS_5 space into the QCD space is achieved when the holographic variable z corresponds exactly to the LF variable ζ. A direct comparison between Eqs. 92 and 89 permits the identification of the effective potential as a function of the dilaton field:

$$U(\zeta, J) = \frac{1}{2}\varphi''(\zeta) + \frac{1}{4}\varphi'(\zeta)^2 + \frac{2J-3}{2\zeta}\varphi'(\zeta)\,, \tag{93}$$

and the AdS mass as a function of the hadron total angular momentum J and the orbital angular momentum L:

$$(mR)^2 = -(2-J)^2 + L^2\,. \tag{94}$$

As was aforementioned, in the soft-wall model, the dilaton background field has the quadratic form $\varphi(z) = \kappa^2 z^2$, whose substitution into Eq. 93 leads to effective potential:

$$U(\zeta, J) = \kappa^4\zeta^2 + 2\kappa^2(J-1)\,. \tag{95}$$

The insertion of this potential into the LF QCD wave equation Eq. 89, turns the difficult problem of solving a relativistic equation for light bound-states into the problem of solving the Schrödinger equation for the harmonic oscillator potential in two dimensions. Therefore, the normalized solutions of Eq. 89 are:

$$\phi_{n,L}(\zeta) = \kappa^{1+L}\sqrt{\frac{2n!}{(n+L)!}}\zeta^{1/2+L}\exp\left(\frac{-\kappa^2\zeta^2}{2}\right)L_n^L\left(\kappa^2\zeta^2\right)\,, \tag{96}$$

[5] The LF approach leads to an equation that exhibits the same form as the simple non-relativistic Schrödinger equation, however, it is a fully relativistic approach, thus it produces a relativistic wave function.

where $L_n^L\left(\kappa^2\zeta^2\right)$ are the Laguerre polynomials, and the eigenvalues are

$$M^2 = 4\kappa^2\left(n + \frac{J}{2} + \frac{L}{2}\right). \tag{97}$$

These eigenvalues are responsible for the description of meson spectroscopy data. Thus, the value of the effective potential free parameter κ, which comes from the dilaton field, can be chosen in a way that best suits its purpose. In the original model [131, 132], κ is a universal constant parameter, which is fixed for all mesons. Its value was selected considering the Regge trajectories of the ρ vector meson family [133], however, this choice leads to the necessity of introducing a mass shift in Eq. 97 to describe the spectroscopy of other vector mesons, like the ϕ. As can be seen in Fig 16, this provides a good description of the ground states with $L = 0$ and $L = 2$, however, it fails to describe the first excited states with $L = 0$. Therefore, since one aim of this project is precisely to describe these excited states, we enable κ to depend on the vector meson ground state mass [6]. This choice is consistent with the fact that κ is related to the Regge slope [134]. Hence, for each vector family, we calculate a different κ parameter that is compatible with Eq. 97:

$$\kappa = \frac{M_{V\,(n=0)}}{\sqrt{2}}. \tag{98}$$

This parameterization provided a good description of the ground and the excited states of the three light vector mesons studied in this project (ρ, ω, and ϕ). The left panel of Fig. 16 shows the Regge curves obtained with Eq. 97 and the mass-dependent κ parameter for the ρ (gray solid curves) and ω (blue dashed curves) vector mesons and compared with spectroscopy data [136]. The results described well the data, which was expected since in this case κ is practically the same as the one found in the original model [12]. The right panel presents results for the ϕ spectroscopy obtained with the mass-dependent κ (blue dashed curves) and with the fixed $\kappa = 0.54$ GeV (gray solid lines). As was aforementioned, the non-fixed κ permitted a better description of the states with $L = 0$.

Returning to the vector meson wave function, it is worth recalling that Eq. 96 was obtained in the quark massless limit $m_q \to 0$. However, it is expected that the effective interaction of the constituents depends on the quark masses. A natural idea would be to include this interaction into the effective potential equation (93), since it encodes the state dynamics; however, it would break the conformal symmetry. Thus, following the original Brodsky- de Téramond model, the quark mass dependence can be included in the invariant mass (Eq. 84) by substituting:

$$M^2_{q\bar{q}} = \frac{\mathbf{k}_\perp^2}{\beta(1-\beta)} \to \frac{\mathbf{k}_\perp^2}{\beta(1-\beta)} + \frac{m_q^2}{\beta} + \frac{m_{\bar{q}}^2}{1-\beta}. \tag{99}$$

This leads to the inclusion of the exponential term $e^{\frac{m_q^2}{\beta}+\frac{m_{\bar{q}}^2}{1-\beta}}$ into Eq. 86, which now will have the form:

$$\psi(\beta,\zeta,\varphi) = e^{iL\varphi}X(\beta)e^{\frac{m_q^2}{\beta}+\frac{m_{\bar{q}}^2}{1-\beta}}\frac{\phi(\zeta)}{\sqrt{2\pi\zeta}}. \tag{100}$$

[6] There are other works that do not fix κ to a universal constant value, such as [134, 135]

Figure 16 – Spectroscopy of light vector mesons. The left panel shows the Regge trajectories calculated with the mass-dependent κ for ρ (gray solid curves) and ω (blue dashed curves) mesons. The right panel compares the results obtained with the mass-dependent κ (blue dashed curve) and the fixed-value κ (gray solid curve) for ϕ vector meson. The data shown in the plots were taken from [136]

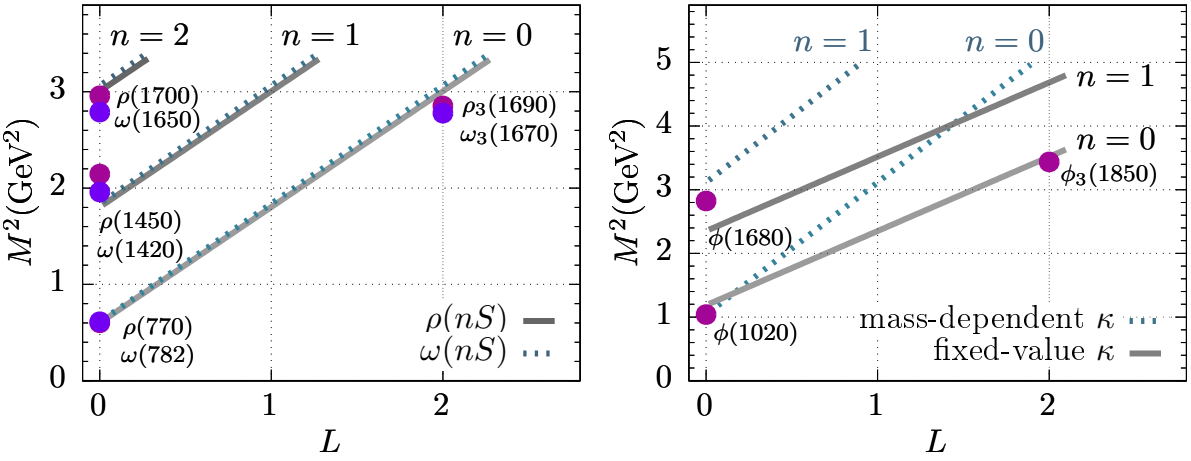

Source: Elaborated by the author.

The inclusion of the quark masses is a big obstacle that prevents the utilization of the holographic model to find wave equations for heavy vector mesons. Its high mass is responsible for strongly breaking the conformal symmetry, which makes the limit of massless quarks pointless. Thus, this theory is not suitable for heavy mesons. This is a good reason why the treatment for calculating the light and heavy vector meson wave functions needs to be different.

Finally, the hadronic bound state wave function shown in Eq. 100, represents only the scalar part of the vector meson wave function that appears in Eq. 10. Therefore, the full expressions for the vector meson wave functions, which contain the helicities of the quark $(h \pm \frac{1}{2})$ and antiquark $(\bar{h} \pm \frac{1}{2})$ and the polarization λ, are [137, 138]:

$$\Psi^{h,\bar{h}}_{V,L(\lambda=0)}(r,\beta) = \mathcal{N}_L \frac{1}{2\sqrt{2}} \delta_{h,-\bar{h}} \left(1 + \frac{m_f^2 - \nabla_r^2}{M^2\beta(1-\beta)}\right) \psi(\beta,\zeta) \tag{101}$$

$$\Psi^{h,\bar{h}}_{V,T(\lambda=\pm1)}(r,\beta) = \pm\mathcal{N}_T \left[ie^{\pm i\theta}\left(\beta\delta_{h,\pm}\delta_{\bar{h},\mp} - (1-\beta)\delta_{h,\mp}\delta_{\bar{h},\pm}\right)\partial_r + m_f\delta_{h,\pm}\delta_{\bar{h},\pm}\right] \frac{\psi(\beta,\zeta)}{2\beta(1-\beta)}\,. \tag{102}$$

It is worth mentioning that in these equations $\nabla_r^2 \equiv \frac{1}{r}\partial_r + \partial_r^2$ and that they are normalized to:

$$\sum_{h,\bar{h}} \int \mathrm{d}^2\mathbf{r}\mathrm{d}\beta \left|\Psi^{h,\bar{h}}_{\lambda}(r,\beta)\right|^2 = 1\,. \tag{103}$$

With this fundamental piece of the color dipole model, one can calculate cross sections for the three light vector mesons: ρ, ω, and ϕ.

3.4 LIGHT VECTOR MESON NUMERICAL RESULTS

The search for a universal theoretical approach able to describe all available observables is an important goal for all theoretical physicists. With this purpose, we decided to test the formalism presented in the previous chapter on light vector mesons, since their small masses make them a good tool for probing the non-perturbative QCD regime. Therefore, in this section, results for total and differential cross sections will be presented for the production of ρ, ω, and ϕ vector mesons in $\gamma^{(*)}p$ collision. To avoid confusion, let's clarify the notation used in the labels of the figures. The symbol γ represents real photons, while γ^* represents virtual photons. All calculations were performed using the AdS/QCD holographic wave functions, explained in the previous section. In addition, the results will be presented for two b-dependent partial dipole models: the bCGC and the bSat. This choice was taken based on the fact that there are a lot of uncertainties regarding which is the best model for describing the dipole-proton interactions [38, 139], since this part is very perturbative and, hence, very sensible to the modeling process. In a separate study, we tested a few parameterizations and found that the bCGC and the bSat were the ones that best described the available data for ρ, ω, and ϕ production cross sections.

In Fig. 17, results for the total cross section for ρ photoproduction are shown as a function of the center-of-mass energy W. As was aforementioned, the curves were obtained with the holographic wave function together with bCGC (blue solid line) and bSat (violet dashed line) b-dependent dipole parametrizations. The figure also includes experimental data from H1 [140, 141], ZEUS [142] and CMS [92] collaborations. As can be seen, the bSat model is more successful in describing the available data than the bCGC model, especially at lower W values. Unfortunately, for higher W, none of the models are capable of describing the few existing data points.

Figure 17 – Total cross section for the $\rho(1S)$ photoproduction as a function of γp center-of-mass energy W. The results are compared to data from H1 [140, 141], ZEUS [142] and CMS [92] collaborations.

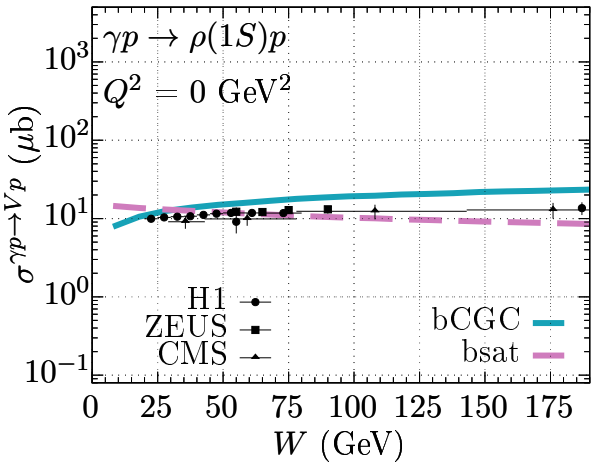

Source: Elaborated by the author and published in [41].

In the same way as Fig. 17, Fig. 18 presents the total cross section as a function of W. However, in this case, it is calculated for ρ electroproduction (which means $Q^2 > 0$). Here, the darker curves represent small Q^2 values while the lighter ones correspond to higher Q^2. The curves were obtained with the same setup of the previous figure and compared, on the left panel, to the H1 data [91] for five distinct values of Q^2 (from top to bottom, $Q^2 = 3.3$, 6.6, 11.9, 19.5, and 35.6 GeV^2, respectively) and, on the right panel, to the ZEUS data [85] for six values of Q^2 (from top to bottom, $Q^2 = 2.4$, 3.7, 6.0, 8.3, 13.5, and 32.0 GeV^2, respectively). This time, the bCGC model outperformed the bSat model in describing the experimental data for all available values of Q^2 and in all measured W ranges.

Figure 18 – Total cross section for $\rho(1S)$ electroproduction as a function of W. The results are compared, on the left, to the data from the H1 [91] collaboration for five values of Q^2 (from top to bottom, we have $Q^2 = 3.3$, 6.6, 11.9, 19.5 and 35.6 GeV^2, respectively) and, on the right, to the data from ZEUS [85] collaboration for six different values of Q^2 (from top to bottom, $Q^2 = 2.4$, 3.7, 6.0, 8.3, 13.5 and 32.0 GeV^2, respectively).

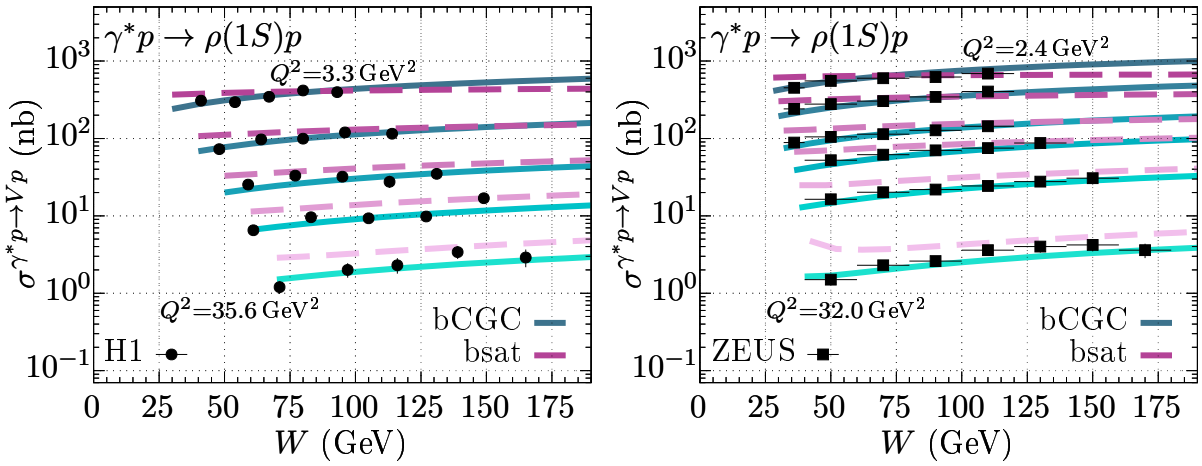

Source: Elaborated by the author and published in [41].

In addition to total cross sections, differential cross sections were also calculated with the dipole formalism using the holographic wave function and bCGC and bSat dipole models. An example is shown in Fig. 19 for $\rho(1S)$ photoproduction as a function of the momentum transfer squared $|t|$ for $W = 35.6, 108$ GeV (left panel), and for $W = 24, 65$ GeV (right panel). The results were compared to data from CMS [92] and H1 [141] collaborations, respectively. To prevent an overlap of the curves, in each panel, the curves with higher W values ($W = 108$ GeV, $W = 65$ GeV), indicated by darker colors, were multiplied by a factor of ten. Analyzing the plots, one might find that the bSat model provides a better overall description of the available data sets. However, a closer observation shows that H1 collaboration data points in the higher-t regime present big error bars and that in this regime the bCGC model comes closer to the central value of the measurement. At small $|t|$, one can see that the bSat model provides a better description of the data for higher W (represented by darker curves). Remarkably, at the same regime and for $W = 24$ GeV, the curve corresponding to the bCGC model becomes

closer to the data points than the bSat, and finally, bCGC and bSat models have very similar behaviors at $W = 35.6$ GeV. This observation emphasizes the fact that there is no single b-dependent partial dipole amplitude parametrization that perfectly describes all existing data for $\rho(1S)$ photoproduction.

Figure 19 – Differential cross section of $\rho(1S)$ photoproduction as a function of the momentum transfer squared $|t|$ and compared to data from the CMS collaboration [92] (left panel) and the H1 collaboration [141] (right panel). The darker upper curves were multiplied by a factor of ten in order to distinguish them from the lighter ones.

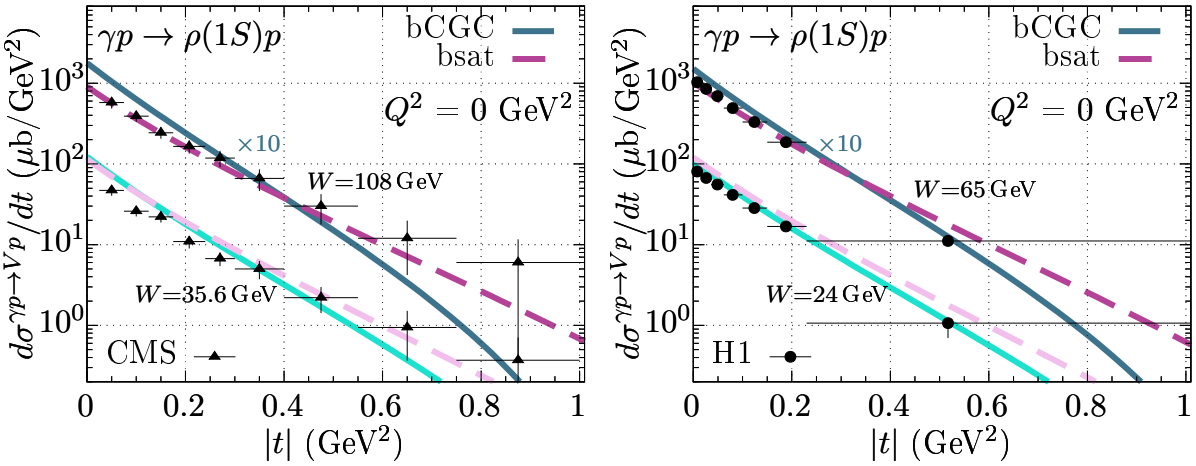

Source: Elaborated by the author and published in [41].

Fig. 20 presents the differential cross section as a function of the momentum transfer squared $|t|$ for $\rho(1S)$ electroproduction at $W = 75$ GeV. The left panel, shows a comparison between the results obtained with bCGC and bSat models and the corresponding H1 data [91] for three different values of Q^2 (from top to bottom, $Q^2 = 3.3$, 11.5 and 33.0 GeV^2, respectively). In this case, the bCGC model performs better in describing the experimental data. Consequently, on the right panel, more results are shown for five different Q^2 values (namely, from top to bottom, $Q^2 = 3.3$, 6.6, 11.5, 17.4 and 33.0 GeV^2, respectively), but calculated just with the bCGC model.

As was aforementioned, the use of the holographic model permits one to obtain wave functions for other mesons than ρ. Hence, the left panel of Fig. 21 exhibits the total cross section as a function of W for two distinct production scenarios: one with $Q^2 = 0$ GeV^2 (represented by the darker curve) and other with $Q^2 = 7$ GeV^2 (represented by the lighter curve). They are compared to data from fixed target experiments [143, 144, 145, 146, 147, 148, 149, 150, 151, 152, 153, 154] (a compilation of these data can be found in Ref. [155]), and from the ZEUS Collaboration [155, 156]. One can notice that the bCGC model exhibits a strong agreement with the available data (i.e. excluding the ZEUS data point for $Q^2 = 0$ GeV^2). The right panel of Fig. 21 shows the differential cross section for the $\omega(1S)$ photoproduction as a function of momentum transfer squared $|t|$ for $W = 80$ GeV compared to data from the ZEUS Collaboration [155]. The obtained curves are close to the experimental data, which is a

Figure 20 – Differential cross section for $\rho(1S)$ electroproduction as a function $|t|$ for $W = 75$ GeV. The left panel shows a comparison of the results obtained by using the bCGC and bSat models with the H1 data [91] for three distinct values of Q^2 (from top to bottom, $Q^2 = 3.3$, 11.5 and 33.0 GeV^2, respectively). The right panel presents the curves obtained only with the bCGC model and compared to the H1 data for five different Q^2 values (from top to bottom, $Q^2 = 3.3$, 6.6, 11.5, 17.4 and 33.0 GeV^2, respectively).

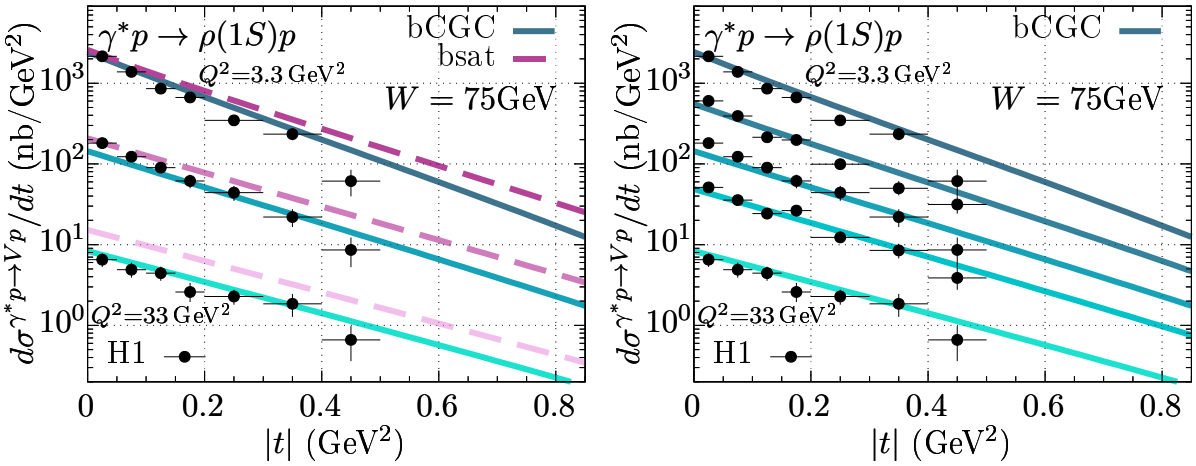

Source: Elaborated by the author and published in [41].

significant observation considering the difficulties of describing t-dependent differential cross sections with the dipole approach.

Figure 21 – Results for the $\omega(1S)$ photo- and electroproduction cross sections. On the left panel, the total cross section is shown as a function of W for $Q^2 = 0$ GeV^2 (darker curves) and $Q^2 = 7$ GeV^2 (lighter curves) and compared with the fixed target measurements [143, 144, 145, 146, 147, 148, 149, 150, 151, 152, 153, 154] (a compilation of these data can be found in Ref. [155]) and also with the data from the ZEUS Collaboration [155, 156]. On the right panel, the differential cross section is shown as a function of $|t|$ for $W = 80$ GeV and compared with ZEUS data [155].

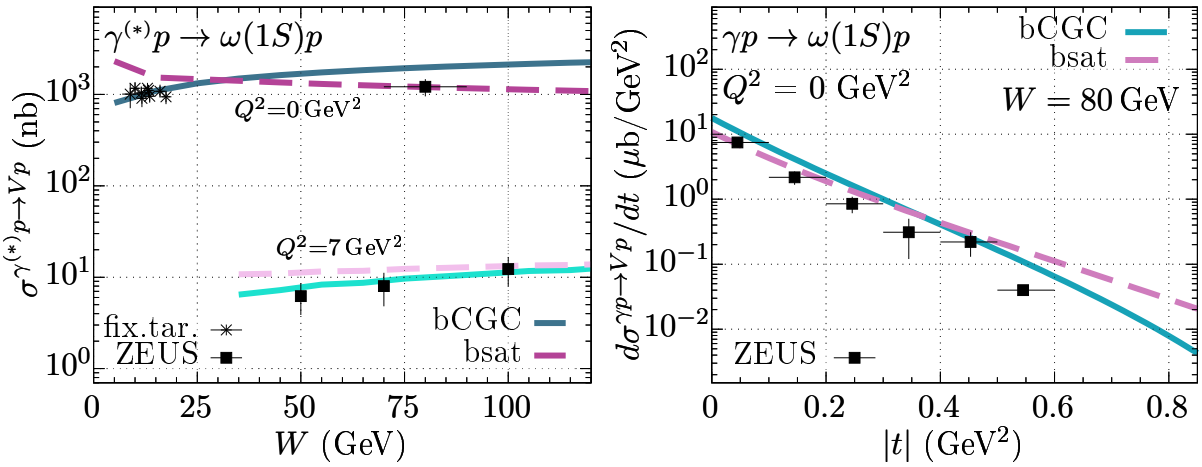

Source: Elaborated by the author and published in [41].

On the left panel of Fig. 22, the total cross section for the $\phi(1S)$ electroproduction is presented as a function of W and compared with experimental data from the ZEUS Collaboration [157]. Only the results obtained using the bCGC dipole parametrization are exhibited in this plot, as it proved to be the most successful in describing the vector meson electroproduction data. Similarly to the previous electroproduction cases, the curves exhibited a notable correspondence with the available data for four distinct Q^2 values (from top to bottom, $Q^2 = 2.4$, 3.8, 6.5 and 13.0 GeV^2, respectively). On the right panel, the differential cross section is shown as a function of $|t|$ for $W = 75$ GeV. In the same way, the available data for seven different sets of Q^2 values provided by the ZEUS Collaboration [157] (from top to bottom: $Q^2 = 2.4$, 3.6, 5.2, 6.9, 9.2, 12.6, and 19.7 GeV^2) are well described. It is a good point to mention that these excellent results were obtained with the mass-dependent κ parameter. Consequently, one can conclude that it can provide a good description of the experimental data sets for all three light vector mesons.

Figure 22 – Results for $\phi(1S)$ electroproduction cross sections compared with the ZEUS data [157]. The results were obtained only with the bCGC model. On the left panel, the total cross section is shown as a function of W and compared to four datasets with different Q^2 values (from top to bottom, $Q^2 = 2.4$, 3.8, 6.5 and 13.0 GeV^2, respectively). On the right panel, the differential cross section is shown as a function of $|t|$ for $W = 75$ GeV and compared with data points for seven different values of Q^2 (from top to bottom, $Q^2 = 2.4$, 3.6, 5.2, 6.9, 9.2, 12.6 and 19.7 GeV^2, respectively).

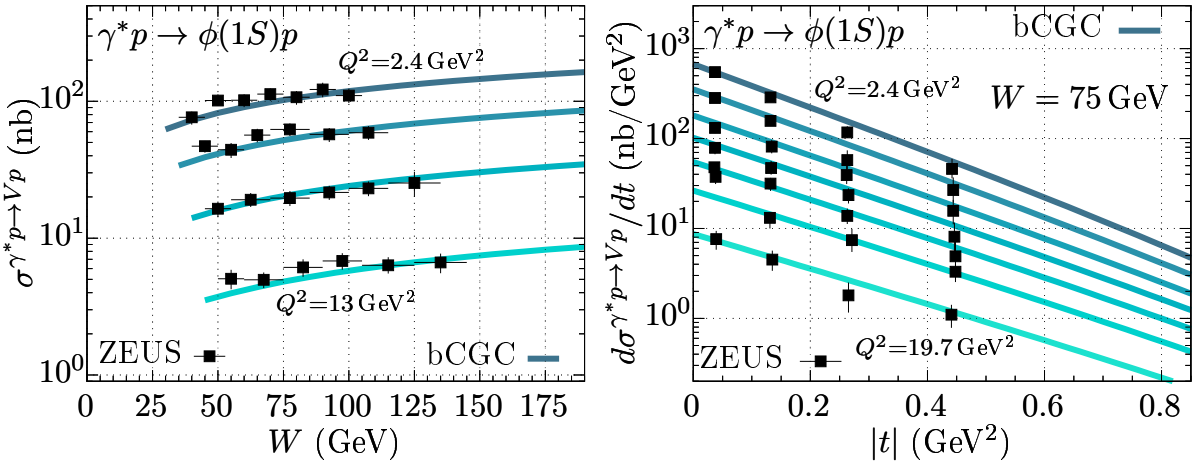

Source: Elaborated by the author and published in [41].

As was previously mentioned, one advantage of the holographic approach is that it enables obtaining wave functions for excited states. Therefore, predictions for the total cross section for $\rho(2S)$ (darker blue solid line), $\omega(2S)$ (medium shade of blue dotted line), and $\phi(2S)$ (lighter blue dashed line) photoproduction are presented in Fig. 23 as functions of W. Correspondingly, on the right panel, predictions for the differential cross sections as functions of $|t|$ are shown for a fixed $W = 108$ GeV. All these curves are obtained with the bCGC model, since it was most successful in describing the available data for ground-state electroproduction.

Figure 23 – Predictions for the total cross section as a function of W (left panel) and for the differential cross section as a function of $|t|$ (right panel) for $\rho(2S)$ (darker blue solid line), $\omega(2S)$ (medium shade of blue dotted line) and $\phi(2S)$ (lighter blue dashed line) photoproduction.

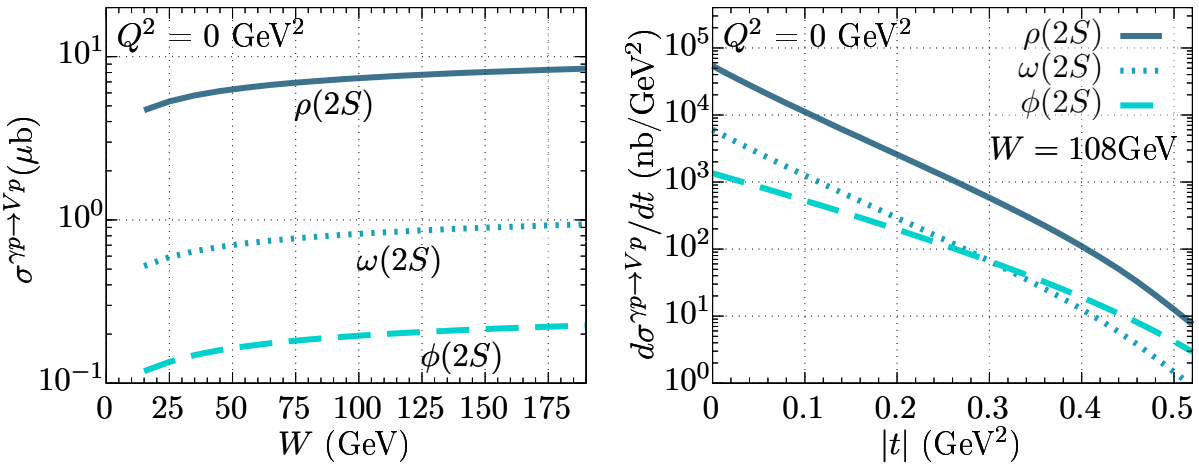

Source: Elaborated by the author and published in [41].

Given the significant discrepancies observed among the results obtained with different parametrizations of the partial dipole amplitude, particularly in the photoproduction case, we decided to present in Fig. 24 predictions for the ratio between the excited-state total cross section and its corresponding ground-state total cross section as a function of W (left panel), as well as the ratio between the excited-state differential cross section and the ground-state differential cross section as a function of $|t|$ for $W = 108$ GeV (right panel), for the three distinct light vector mesons. To enhance the visualization of the curves, different line types were used for different mesons (darker solid lines for ρ, medium shade dotted lines for ω, and lighter dashed lines for ϕ) and different colors were used for representing the results with different partial dipole parameterizations (blue shades were used for bCGC and violet shades correspond to bSat model). As can be seen on both panels, the results obtained with the bSat model are much higher than the ones obtained with the bCGC parametrization. This result corroborates the statement that there are still big uncertainties in the structure of partial dipole amplitudes, that come from the soft and non-perturbative domain [81]. Also, it shows the necessity of improvements on the dipole parametrizations to describe all existing exclusive processes for vector meson production. The forthcoming measurements of the excited states have the potential to play a pivotal role in constraining the dipole models, mostly within the non-perturbative regime.

Figure 24 – Predictions for the ratio of the excited-state total cross section to the ground-state total cross section as a function of W (left panel) and for the ratio of the excited-state differential cross section to the ground-state differential cross section as a function of momentum transfer squared $|t|$ (right panel) for ρ (solid lines), ω (dotted lines) and ϕ (dashed lines) mesons. The blue curves are obtained with the bCGC model, while the violet ones correspond to the bSat model.

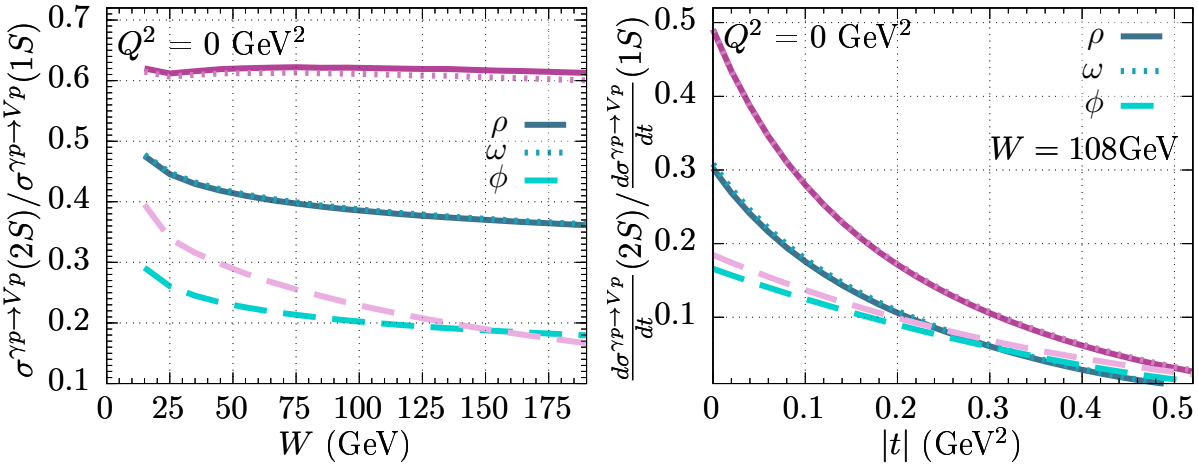

Source: Elaborated by the author and published in [41].

4 VECTOR MESON PHOTOPRODUCTION IN NUCLEAR TARGETS

In the context of nuclear ultraperipheral collisions (UPC), it is also possible to observe the occurrence of vector meson photoproduction. In the last few years, the LHC has released some data for the $\rho(1S)$, $\psi(1S)$, $\psi(2S)$, and $\Upsilon(1S)$ photoproduction in ultraperipheral PbPb collisions, which can be described by extending the color dipole model to the nuclear case considering the Glauber-Gribov formalism. For this purpose, the necessity of including some extra effects, such as gluon shadowing and finite coherence length (which will be explained later), has been verified. Furthermore, it has been speculated that with the construction of future colliders such as the Electron-Ion Collider (EIC) and the Future Circular Collider (FCC), new measurements with nuclear targets will be performed, which could provide relevant information for the processes and predictions studied in this work.

4.1 COHERENT PRODUCTION

The nuclear vector meson photoproduction occurs through the process $\gamma A \to VA$, which maintains the nucleus target intact (left panel of Fig. 25). The scattering cross section is determined by taking the average of the scattering amplitude $\mathcal{A}$ over the interaction eigenstates and then squaring the result

$$\frac{\mathrm{d}\sigma^{\gamma A \to VA}}{\mathrm{d}t} = \frac{1}{16\pi}\left|\left\langle \mathcal{A}^{\gamma A \to VA}(x,\Delta)\right\rangle\right|^2 . \tag{104}$$

Figure 25 – Coherent (left) and incoherent (right) vector meson production in a nuclei collision. In the left panel, one can see that the nucleus remains in the initial state A. Whereas in the right panel, the nucleus target changes from the initial state A to the final state A^*.

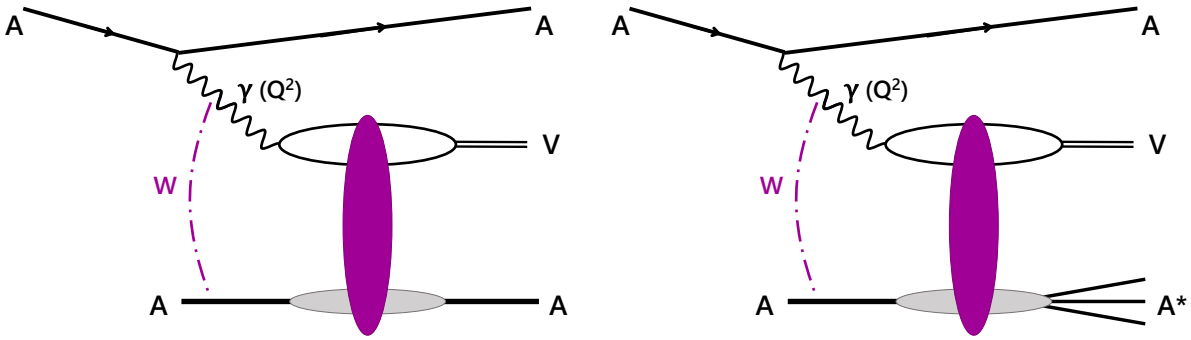

Source: Elaborated by the author.

Since this average is taken over all possible configurations of the nucleons inside the nucleus, this amplitude is sensible to the dipole-nucleus interaction, which probes the gluon distribution at small x. Consequently, the coherent cross section assumes an important role in analyzing the average shape of the target [158].

The Glauber model was the first one to incorporate the shadowing effect[1] in the elastic hadron-nucleus interaction [159]. This model considers that the incident hadron only experiences elastic scatterings with the nucleons inside the nucleus. Thus the hadron-nucleus scattering amplitude is given by the summation of all possible successive rescatterings with the single nucleons (Fig. 26). A more detailed explanation of this calculation can be found in Appendix G.

Figure 26 – Pictorial representation of the Glauber model. One can see that the projectile hadron only scatters elastically with the nucleons inside the nucleus.

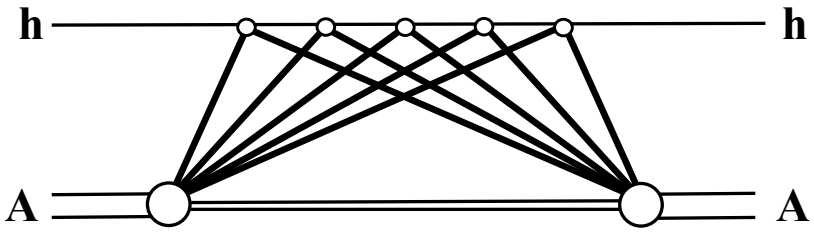

Source: Elaborated by the author.

This approximation of considering only elastic scatterings is reasonable for small energies when the average momenta of the nucleons within the nucleus are small, which prevents the collapse of the nucleus [160]. The problem with this model appears with the energy increase, because it leads to the possibility that particles produced in inelastic scatterings with nucleons inside the nucleus can subsequently be absorbed by other bound nucleons (Fig. 27), which makes the nucleus more transparent. These inelastic corrections were incorporated into the Glauber model by Gribov [160, 161] and lead to an increase of the elastic cross section of about 40%. Briefly, in Glauber model the incident hadron interacts with each nucleon independently, while the Gribov corrections allow for coherent interactions with more than one nucleon.

Figure 27 – Gribov's correction to Glauber's model. As can be seen in the picture, the projectile hadron can suffer diffractive excitations when interacting with a nucleon and undergoes intermediary states before returning to its initial state.

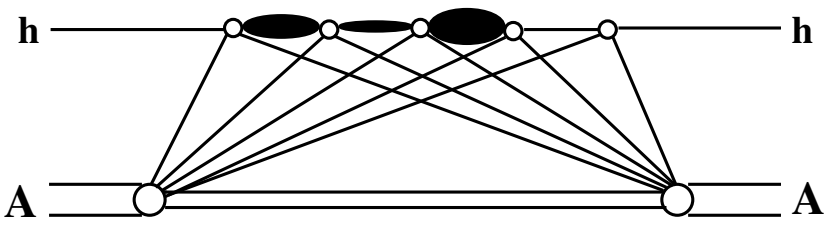

Source: Figure taken from [159].

[1] The term *"shadowing"* is frequently used in the literature to make reference to a reduction of the cross section due to the interaction of the constituents inside the particles that participate in the collision. It comes from the idea that a particle can hide others behind its shadow.

In a modern language, instead of hadrons, a color dipole can be used as an interaction eigenstate. This allows for the calculation of Gribov inelastic corrections to all orders. This occurs because, in this regime, the quark-antiquark pair lifetime, which is called coherence length,

$$l_c = \frac{2\omega'}{M_V^2}\,, \tag{105}$$

is considered to be much bigger than the nucleus radius ($l_c \gg R_A$). In this case, the transverse distance between the quarks remains approximately constant (which is often referred to as "frozen"), which means that the photon does not fluctuate into the $q\bar{q}$ pair during its passage through the nucleus, but rather a long time before (Fig. 28). In this equation, ω' is the photon energy in the nucleus target rest frame and M_V is the vector meson mass.

Figure 28 – Pictoric representation of the coherence length in the high energy limit, i.e., when $l_c \gg R_A$. In this regime, it is considered that the $q\bar{q}$ pair was created a long time before its passage through the nucleus and will transform itself into the vector meson very much time later.

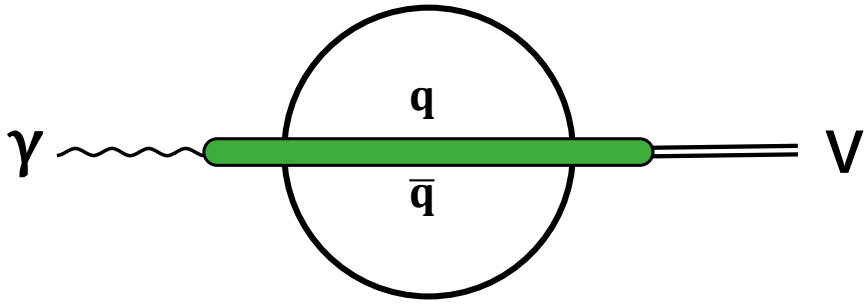

Source: Elaborated by the author. Adapted from [162].

The adoption of the "frozen" approximation enables the determination of an asymptotic expression for the averaged diffractive scattering amplitude [38].

$$\begin{aligned}\left\langle \mathcal{A}^{\gamma A\to VA}(x,\Delta)\right\rangle =& i\int \mathrm{d}^2\mathbf{r}\int_0^1 \mathrm{d}\beta \int \mathrm{d}^2\mathbf{b}\, e^{-i[\mathbf{b}-(1-z)\mathbf{r}]\cdot\boldsymbol{\Delta}} \\ &\times \Sigma_T(r,\beta)\, 2\left[1-\exp\left(-\frac{AT_A(b)\sigma_{q\bar{q}}(x,r)}{2}\right)\right]\,,\end{aligned} \tag{106}$$

with $\Sigma_T = \Sigma^{(1)} + \Sigma^{(2)}\frac{\mathrm{d}}{\mathrm{d}r}$, which was defined in the previous chapter. In this equation, as was discussed previously, $\sigma_{q\bar{q}}$ is the dipole-proton interaction total cross section, A is the mass number, and $T_A(b)$ is the nuclear thickness function, which is defined as the integral of the nuclear density $\rho_A(b,z)$ over the longitudinal coordinate z with fixed impact parameter:

$$T_A(b) = \int_{-\infty}^{+\infty} \mathrm{d}z\, \rho_A(b,z)\,, \qquad \int \mathrm{d}^2\boldsymbol{b}\, T_A(b) = 1\,. \tag{107}$$

In the present study, the Woods-Saxon distribution was employed to represent the nuclear density, which is characterized by the following form [163]:

$$\rho_A(b,z) = \frac{N_A}{1+\exp[\frac{\ell(b,z)-R_C}{\delta}]}\,, \tag{108}$$

where $\ell \equiv |\boldsymbol{\ell}|$ is the distance from the nucleus center to a generic point inside it (defined as $\ell(b,z) = \sqrt{b^2+z^2}$), N_A is a general normalization factor, and the parameters for lead $R_C = 6.62$ fm and $\delta = 0.546$ fm were taken from Ref. [164].

The expression 106 enables not only to calculate the t differential cross section for the $\gamma A \to VA$ process (Eq. 104) but also to calculate the total cross section, given by:

$$\sigma^{\gamma A\to VA} = \int \mathrm{d}^2\boldsymbol{b}\left|\int \mathrm{d}\beta\,\mathrm{d}^2\boldsymbol{r}\,\Sigma_T(r,\beta)\left[1-\exp\left(-\frac{AT_A(b)\sigma_{q\bar{q}}(x,r)}{2}\right)\right]\right|^2 . \tag{109}$$

This is a fundamental piece for the coherent cross section calculation in ultraperipheral collisions, thus it will be used in the upcoming numerical calculations.

4.2 INCOHERENT PRODUCTION

Another possible way to produce vector mesons in nuclear collisions is the one called incoherent production. This consists in a process $\gamma A \to VA^*$ whose nucleus does not remain intact after the collision. In this case, the nucleus passes through a transition to an excited state, composed of nucleons and nuclear fragments, however without any other hadron (it is shown on the right side of Fig. 25).

The scattering amplitude that describes events with initial state $|i\rangle$ and final state $|f\rangle$ is $\langle f\,|\mathcal{A}|\,i\rangle$ (the superscript caption $\gamma A \to VA$ was omitted to make the notation clearer in the next equation). Since in this case the final state must be different than the initial one and what goes into the cross section is the transition amplitude squared, it is convenient to write [158]

$$\sum_{f\neq i}|\langle f\,|\mathcal{A}|\,i\rangle|^2 = \sum_f \langle i\,|\mathcal{A}^*|\,f\rangle\,\langle f\,|\mathcal{A}|\,i\rangle - \langle i\,|\mathcal{A}^*|\,i\rangle\,\langle i\,|\mathcal{A}|\,i\rangle \tag{110}$$

$$= \langle i\,|\mathcal{A}^*\mathcal{A}|\,i\rangle - |\langle i\,|\mathcal{A}|\,i\rangle|^2 . \tag{111}$$

The last line was obtained with the completeness relation $\sum_f |f\rangle\langle f| = \mathbb{1}$. One can identify the first term of this equation as the average, over the initial states, of the absolute value of the scattering amplitude squared, while the second one is the square of the averaged amplitude, which can be identified as the coherent part of the scattering. This makes the vector meson incoherent production cross section to be given by:

$$\frac{\mathrm{d}\sigma^{\gamma A\to VA^*}}{\mathrm{d}t} = \frac{1}{16\pi}\left(\left\langle\left|\mathcal{A}^{\gamma A\to VA}\right|^2\right\rangle - \left|\left\langle\mathcal{A}^{\gamma A\to VA}\right\rangle\right|^2\right). \tag{112}$$

Since the incoherent cross section is proportional to the variance of the diffractive scattering amplitude, it can measure how sensitive the amplitude is to fluctuations, which can

be probed at different length scales. This occurs because the impact parameter is the Fourier conjugate of the transferred momentum Δ, which can be accessed by measurements. As a result, it can be utilized to restrict the geometry of the fluctuations.

In the same way, as was explained in the previous subsection, the Glauber-Gribov model can be employed to compute the averages indicated in Eq. 112, which can be utilized to derive an expression for the incoherent cross section [165, 166, 167].

$$\begin{aligned}\sigma^{\gamma A\to VA^*} = &\int \mathrm{d}^2\boldsymbol{b}\int \mathrm{d}^2\boldsymbol{r_1}\int_0^1 \mathrm{d}\beta_1\Sigma_T\left(r_1,\beta_1\right)\exp\left[-\frac{A}{2}\sigma_{q\bar{q}}\left(r_1,x\right)T_A(b)\right]\\ &\times\int \mathrm{d}^2\boldsymbol{r_2}\int_0^1 \mathrm{d}\beta_2\Sigma_T\left(r_2,\beta_2\right)\exp\left[-\frac{A}{2}\sigma_{q\bar{q}}\left(r_2,x\right)T_A(b)\right]\\ &\times\left\{\exp\left[\frac{\sigma_{q\bar{q}}\left(r_1,x\right)\sigma_{q\bar{q}}\left(r_2,x\right)}{16\pi B}AT_A(b)\right]-1\right\}.\end{aligned} \tag{113}$$

The elastic cross section of dipole-nucleon interaction ($\sigma_{q\bar{q}}$) is considerably small for heavy quarks [165]. Consequently, the exponential function present in the last line of this equation can be expanded, leading to the following expression:

$$\sigma^{\gamma A\to VA^*} = \int \mathrm{d}^2\boldsymbol{b}\,\frac{AT_A(b)}{16\pi B}\left|\int \mathrm{d}\beta\,\mathrm{d}^2\boldsymbol{r}\,\Sigma_T(r,\beta)\,\sigma_{q\bar{q}}\left(x,r\right)\exp\left(-\frac{AT_A(b)\sigma_{q\bar{q}}\left(x,r\right)}{2}\right)\right|^2. \tag{114}$$

It is worth mentioning that all this formalism was constructed over the supposition that the diffractive scattering amplitude (Eq. 106) was purely imaginary. The real part is taken into account by substituting the dipole cross section in Eqs. 109 and 114 by [168]:

$$\sigma_{q\bar{q}}(x,r) \Rightarrow \sigma_{q\bar{q}}(x,r)\left(1-i\frac{\pi}{2}\frac{\partial\ln\sigma_{q\bar{q}}(x,r)}{\partial\ln\left(1/x\right)}\right), \tag{115}$$

which is included in the numerical calculations.

4.3 FINITE COHERENCE LENGTH

All the formalism described previously was constructed in the limit of long coherence length ($l_c \gg R_A$). Nevertheless, it is necessary to consider the case in which the coherence length is smaller than the nucleus radius ($l_c \lesssim R_A$). In this regime, the photon can propagate through the nucleus without undergoing any attenuation until it fluctuates into a $q\bar{q}$ pair. Accordingly to [165], an adequate form to describe this propagation is by using a Green function that satisfies the bidimensional Schödinger equation [169]. However, since the solution of this equation is only known for the harmonic oscillator potential and with the supposition that the dipole cross section has a simplified and non-realistic form $\sigma_{q\bar{q}} \propto r^2$, it was decided, in this work, to include this effect through the multiplication of the cross sections 109 and 114 by a form factor [168]:

$$\sigma^{\gamma A\to VA^*}(W^2) \Rightarrow \sigma^{\gamma A\to VA^*}(W^2)\,\mathrm{F}^{\mathrm{inc}}(W^2,l_c), \tag{116}$$

$$\sigma^{\gamma A\to VA}(W^2) \Rightarrow \sigma^{\gamma A\to VA}(W^2)\,\mathrm{F}^{\mathrm{coh}}(W^2,l_c). \tag{117}$$

In the incoherent case, the form factor is given by:

$$\mathrm{F}^{\mathrm{inc}}(W^2, l_c) = \int \mathrm{d}^2\boldsymbol{b} \int_{-\infty}^{\infty} \mathrm{d}z \rho_A(b,z) \Big| F_1(W^2,b,z) - F_2(W^2,b,z,l_c) \Big|^2 \Big/ \Big(...\Big)\Big|_{l_c\to\infty} \quad (118)$$

where the term $\Big(...\Big)\Big|_{l_c\to\infty}$ represents the numerator in the infinite coherence length limit. The factor

$$F_1(W^2,b,z) = \exp\left(-\frac{1}{2}\sigma_{\mathrm{VN}}(W^2)\int_z^{\infty}\mathrm{d}z'\rho_A(b,z')\right), \quad (119)$$

represents the probability of the vector meson be produced in the point z and leave the nucleus without experiencing any inelastic interaction (Fig. 29.a). It depends on the total vector meson-nucleon cross section $\sigma_{\mathrm{VN}}(W^2)$, which depends on the center of mass energy W [42]. The second term in Eq. 118,

$$F_2(W^2,b,z,l_c) = \frac{1}{2}\sigma_{\mathrm{VN}}(W^2)\int_{-\infty}^{z}\mathrm{d}z'\rho_A(b,z')F_1(W^2,b,z')e^{i(z'-z)/l_c}, \quad (120)$$

considers that the photon can first produce elastically a bound state in the point z', which will propagate through the nucleus until it interacts quasielastically with another bound nucleon in the point $z > z'$, turning itself into a vector meson (Fig. 29.b).

Figure 29 – Representation of the finite coherence length case. On the left, a virtual photon interacts with a nucleon at z and incoherently produces the $q\bar{q}$ pair, which propagates through the nucleus and then transforms into the vector meson. On the right, the photon first produces elastically the $q\bar{q}$ pair at point z', which propagates through the nucleus until it interacts quasielastically at z, where it transforms into the vector meson.

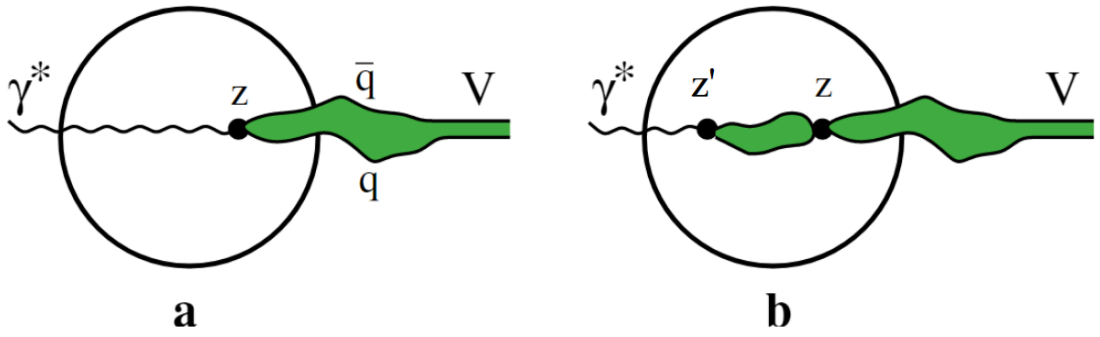

Source: Figure taken from [169].

The form factor for the coherent production presents a much simpler expression that the one seen previously:

$$\mathrm{F}^{\mathrm{coh}}(W^2, l_c) = \int \mathrm{d}^2\boldsymbol{b} \left| \int_{-\infty}^{\infty} \mathrm{d}z \rho_A(b,z) F_1(W^2,b,z) e^{iz/l_c} \right|^2 \Big/ \Big(...\Big)\Big|_{l_c\to\infty}. \quad (121)$$

This occurs because the interaction amplitudes of the vector mesons produced at different longitudinal coordinates add up coherently, which prevents a $q\bar{q}$ pair from interacting with two nucleons before transforming into a vector meson (as can be seen in Fig.29.b).

The authors of the paper [165] exposed that this approach is more appropriate in the description of lighter vector meson photoproduction, like the ρ meson. Although, since this effect is evident only at high rapidities, where there is no experimental data at the present moment, it is not possible to analyze how adequate the finite coherence length procedure is. Moreover, as can be seen in Eq. 105, this effect becomes less noticeable with the energy increase, thus it will be less relevant in future measurements at the upcoming colliders, like the FCC (which promises to reach energies close to 100 TeV [170]).

4.4 GLUON SHADOWING

At the high energy regime, the nuclei experience Lorentz contraction, as also do the nucleons inside them. Nevertheless, the gluon density inside these nucleons exhibits a smaller contraction in comparison to the remaining constituents of the system, because they carry a smaller momentum fraction, which is proportional to x. Consequently, gluons originated from different nucleons can fuse, making the gluon density inside the nucleus smaller than the one of free nucleons. This effect is named gluon shadowing.

Figure 30 – Diagrams of the photon-nucleon interaction with a gluon emission, i.e., for the $\gamma N \to q\bar{q}GN$ process.

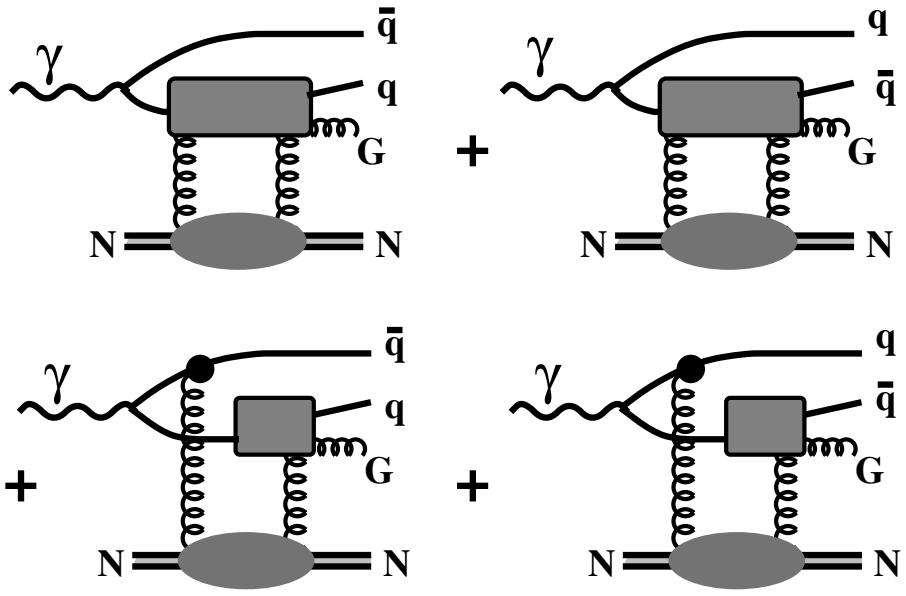

Source: Figure taken from [49].

In the nucleus rest frame, this phenomenon is seen as the inclusion of higher states that comprehend gluon radiations, i.e., $|q\bar{q}G\rangle$, $|q\bar{q}2G\rangle$, ... , $|q\bar{q}nG\rangle$ (the first state diagrams, that include the radiation of one gluon are shown in Fig. 30). The expressions for the nuclear cross section (109 and 114) consider only that the lowest state created by the photon splitting $|q\bar{q}\rangle$ participates of the multiple scatterings in the nucleus [168]. As aforementioned, the dipole cross section $\sigma_{q\bar{q}}$ already considers the higher states with gluon emission, however, it only

describes the dipole-nucleon interaction and not the interaction with the whole nucleus, case where the states with gluon emission should have a smaller coherence length than the one that just produces the $q\bar{q}$ pair $l_c^g < l_c$. Thus, it is expected that the states with gluon radiation will survive less time in nuclear targets than in proton targets, generating a shadowing effect in the nuclear cross section.

Since the gluon radiation is taken into account in the dipole cross section, the most suitable way to incorporate this change in the gluon distribution is by renormalizing it through fits to data:

$$\sigma_{q\bar{q}}(r,x) \to \sigma_{q\bar{q}}(r,x) R_G(x,\mu^2)\,. \tag{122}$$

In this modification, the R_G factor is the ratio between the gluon density inside a nucleon in a nucleus and the one found in a free nucleon

$$R_G(x,\mu^2) = \frac{x g_A(x,\mu^2)}{A x g_p(x,\mu^2)}\,. \tag{123}$$

Instead of using the analytic calculations found in the literature [168, 169, 171], it was decided, in this project, to use the nuclear parton distribution EPPS16 [172], and the proton parton distribution CT14 [58], adjusted to LHC data and including next to leading order correction, to evaluate this ratio. This approach privileges the universality of this part of the process, which is intrinsically non-perturbative. Similar to previous studies [171], the factorization scale chosen to be used in the PDFs is $\mu = M_V/2$.

4.5 PHOTON FLUX AND ULTRAPERIPHERAL COLLISIONS

Hitherto, it was only studied interactions of photons with nucleus and the effects that arise from it, for this reason, this section will present a discussion about the origin of the photons in nuclear collisions. In the large particle accelerators, like the LHC, the nuclei are accelerated to velocities very close to the speed of light. Since these nuclei have a non-zero electric charge, its movement is responsible for the generation of strong electromagnetic fields.

In 1924, Enrico Fermi formulated the equivalent (or virtual) photon method, which basically states that the electromagnetic fields generated by a moving charge can be described by a photon flux [173, 174]. Ten years later, Weizsäcker and Williams independently extended this idea to the ultrarelativistic particles case, which was named Weizsäcker-Williams method.

They realized that when a charged particle is moving in the limit of $v \sim c$, a symmetry of the electric and magnetic fields generated by its motion arises. This symmetry is a characteristic of electromagnetic fields and makes an inertial observer unable to distinguish the origin of these fields, whether they come from a charged particle with ultrarelativistic velocity or they come from a radiation pulse propagating in the same direction.

This radiation pulse can be seen as a flux of virtual photons, which is defined as the Fourier transform of the time-dependent electric fields. The complete procedure to obtain this quantity can be found in the appendix B, where one can verify that the equivalent photon flux

per unit area and photon energy is:

$$\frac{d^3N_\gamma(\omega, \boldsymbol{b_\gamma})}{d\omega d^2 b_\gamma} = \frac{Z^2\alpha_{\text{em}}\zeta^2}{\pi^2\omega b_\gamma^2}\left[K_1^2(\zeta) + \frac{1}{\gamma^2}K_0^2(\zeta)\right], \qquad \zeta = \frac{b_\gamma\,\omega}{\gamma}, \tag{124}$$

in which $\gamma = \sqrt{s/2m_p}$ is the Lorentz factor for a proton inside the projectile nucleus with mass equal to $m_p = 0.938$ GeV, Z is the atomic number (which in the lead case is 82) and b_γ is the photon impact parameter. It is worth mentioning that in this equation ω is the photon energy in the collision center of mass frame, which is related to ω' (Eq. 105) by $\omega' = 2\gamma\omega$.

From this point of view, it is possible to substitute the incident particle with the photon flux shown previously. Therefore, using the factorization, a cross section for a hadronic process can be written as a convolution of the photon flux and the photon-target cross section [175]:

$$\sigma^{AA\to AVX} = \int \mathrm{d}\omega \frac{\mathrm{d}N(\omega)}{\mathrm{d}\omega}\sigma^{\gamma A\to VX}. \tag{125}$$

This equation is very suitable for describing ultraperipheral collisions between two nuclei (AA), defined as those in which the impact parameter exceeds the sum of the nuclei radius ($b > 2R_A$), because for large b-values the strong interactions are suppressed and the photoproduction processes become dominant (Fig. 31).

Figure 31 – Schematic representation of an ultraperipheral collision involving two lead nuclei.

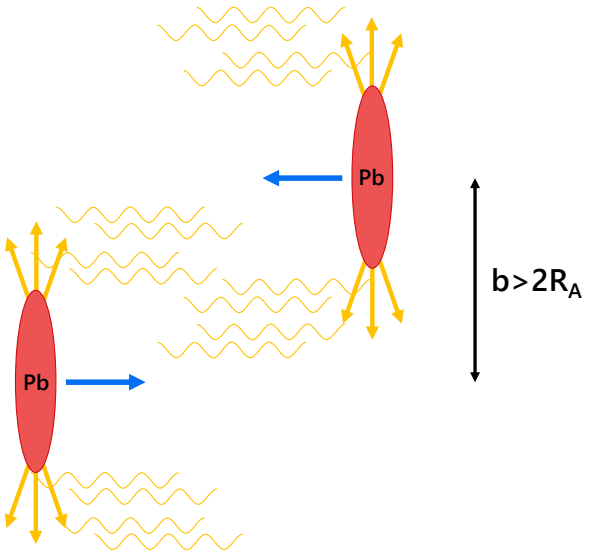

Source: Elaborated by the author.

Since 2010, the LHC has been studying ultraperipheral collisions with lead nuclei. However, the most recent data published by this collider are not presented in terms of the photon energy but in terms of the final state rapidity. There it is convenient to rewrite Eq. 125 as a rapidity distribution. The relation between the rapidity and the photon energy is $y = \ln\frac{2\omega}{M_V}$, which enables Eq. 125 to be written in the following way:

$$\frac{\mathrm{d}\sigma^{AA\to AVX}}{dy} = \omega\frac{\mathrm{d}N(\omega)}{\mathrm{d}\omega}\sigma^{\gamma A\to VX}. \tag{126}$$

Since the two nuclei that participate in the collision can act both as the source of the virtual photons and as the target, it is necessary to include in the last equation a term identic to the one shown in the right part of Eq. 126, but replacing $y \to -y$. Besides that, given that the photon flux obtained in Eq. 124 depends on the impact parameter, as well as the photon-nucleus cross section, it is more appropriate to add impact parameter integrals to Eq. 126, thus obtaining:

$$\frac{d\sigma^{AA\to AVX}}{dy} = \int \mathrm{d}^2b \int \mathrm{d}^2b'\, \omega \frac{dN_\gamma(\omega, \boldsymbol{b_\gamma})}{d\omega d^2b_\gamma} \frac{d\sigma^{\gamma A\to VX}(\omega, \boldsymbol{b'})}{d^2b'} \,. \tag{127}$$

In this equation, $\mathbf{b}$ is the distance between the center of the two nuclei, and $\mathbf{b}'$ is the distance between the nucleus target center and the interaction point. Consequently, it is possible to relate these two quantities to the photon impact parameter $\boldsymbol{b_\gamma} = \boldsymbol{b'} - \boldsymbol{b}$ (Fig. 32).

Figure 32 – Schematic representation of the impact parameter relation $\boldsymbol{b_\gamma} = \boldsymbol{b'} - \boldsymbol{b}$ in the transverse plane of the collision.

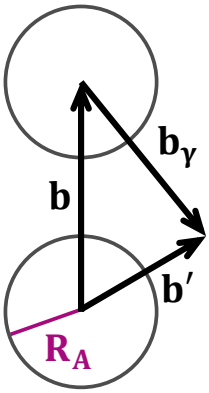

Source: Figure adapted from [176].

It is noteworthy that, as was aforementioned, the integral with respect to the impact parameter b should have its lower limit equal to $2R_A$, to ensure that there is no overlap between the nuclei. Even if that was not the case, this integral can never start from zero, due to a constraint imposed by quantum mechanics. It is known that each particle can be described by a wave packet with a width of at least $\Delta x \geq \hbar/p_{max}$, where p_{max} represents the maximum momentum transferred during the collision. Hence, it just makes sense to consider the collision impact parameter if it satisfies the condition $b > \Delta x$ [174].

4.6 NUMERICAL RESULTS

This chapter presents a methodology to obtain the rapidity distributions for the vector meson photoproduction in ultraperipheral collisions. Based on this mathematical development, several numerical results have been obtained, which will be shown below.

4.6.1 t- integrated heavy vector meson y- distributions

Following the steps taken in the previous chapter, we computed the t-integrated cross sections for the heavy vector meson photoproduction in lead-lead (PbPb) collisions at the LHC energies, employing two dipole models, namely, the GBW and the KST parametrizations.

Fig. 33 shows the differential cross section as a function of the rapidity for the coherent photoproduction of $\psi(1S)$ and $\psi(2S)$ in ultraperipheral collisions at 2.76 TeV (left) and $\psi(1S)$ at 5.02 TeV (right). In both panels, the results were obtained using all five $q\bar{q}$ pair interaction potentials, mentioned earlier, and the GBW model for the color dipole cross section.

In the left graph, the results evaluated at 2.76 TeV for the ground state were compared to CMS [5] and ALICE [6, 7] data, while the results for the excited states were compared to ALICE data [8]. One can notice that for the $\psi(1S)$ case, the data can be well described by all five curves. However, this does not occur for $\psi(2S)$, where only the oscillator potential curve lies within the error bars.

On the right graph, the $\psi(1S)$ results at an energy of 5.02 TeV were compared with experimental data from ALICE [9] and preliminary results from LHCb [10]. As one can see in the figure, a satisfactory agreement with the LHCb data was achieved, whereas, for the ALICE data, it was not. Nevertheless, it should be noted that a huge tension exists between the measurements of the two groups, making it practically impossible to describe both datasets simultaneously.

Figure 33 – Rapidity distribution for the coherent ψ photoproduction in PbPb UPCs at 2.76 TeV (left) and 5.02 TeV (right). The results obtained for 2.76 TeV were compared to data from CMS [5] and ALICE [6, 7] collaborations for J/ψ and from ALICE [8] for ψ'. The results for 5.02 were compared to data from ALICE [9] and with LHCb preliminary results [10].

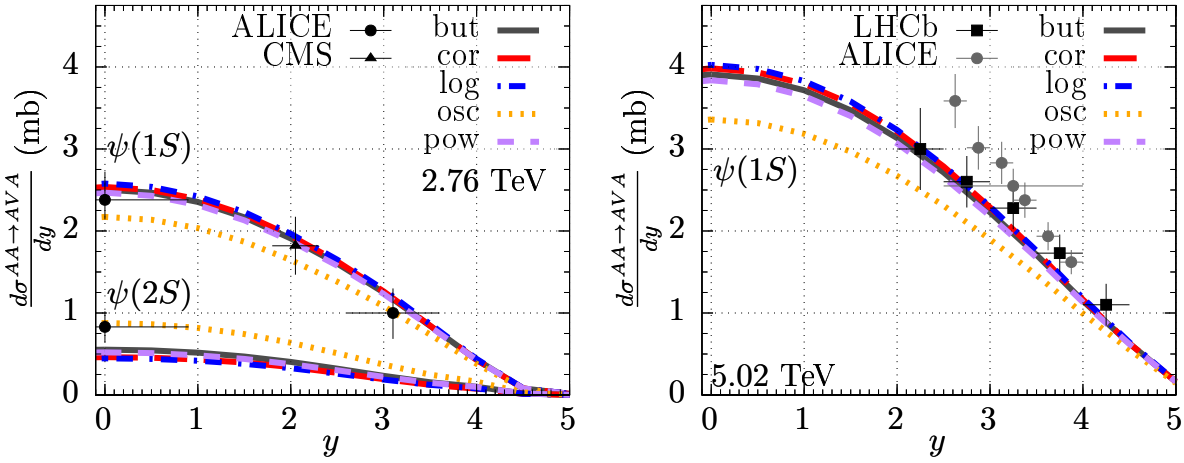

Source: Elaborated by the author and published in [11].

In Fig. 34, predictions for the differential cross section are shown as a function of the rapidity for the coherent photoproduction of $\Upsilon(1S)$ (left) and $\Upsilon(2S)$ (right) at 5.02 TeV in PbPb collisions. In the same way as in Fig. 33, the results were obtained for the five potentials

aforementioned, the only difference is the color dipole cross section, which for this case it was used the KST model.

Upon analyzing the curves depicted in the left panel of this figure, a significant spread is observed, mainly at small rapidity values. This effect comes from the shape of the $\Upsilon(1S)$ wave function [4], which differs more among themselves than the other studied bound states. This can be noted on the right graph, which shows a significant resemblance between the potential curves, except for the harmonic oscillator potential, which is responsible for a curve that is nearly twice as high as the others.

Figure 34 – Predictions for the rapidity distribution for the coherent $\Upsilon(1S)$ (left) and $\Upsilon(2S)$ (right) photoproduction in PbPb UPCs at 5.02 TeV.

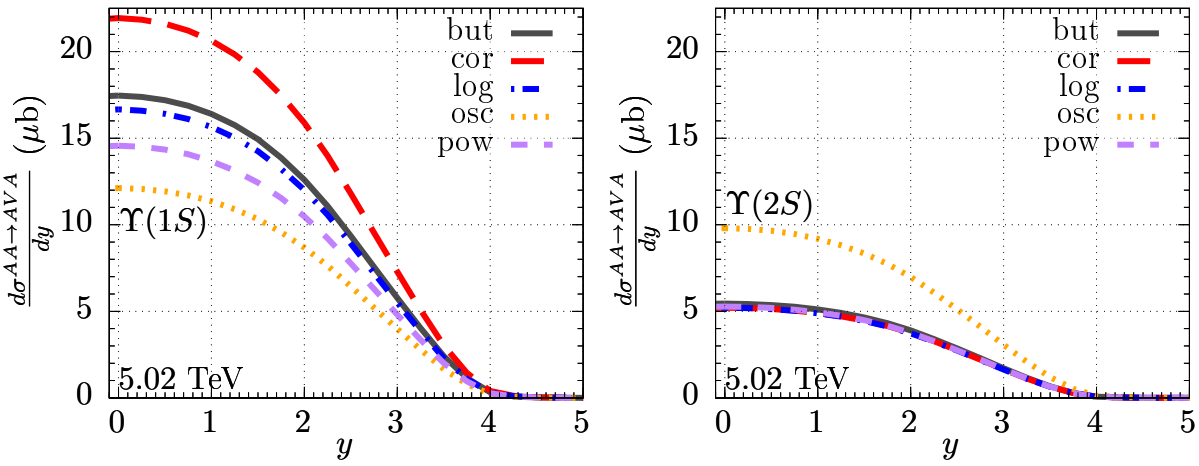

Source: Elaborated by the author and published in [11].

In order to analyze the impact of the model choice on the calculations, Fig. 35 presents the results for the $\Upsilon(1S)$ coherent photoproduction at 5.02 TeV using all five different color dipole parameterizations aforementioned. It was chosen to use the vector meson wave functions calculated with the Cornell (darker curves) and harmonic oscillator (lighter curves) potentials because, in this case, they yield the most discrepant results (as evident from the left panel of Fig. 34). It is very clear that the model choice significantly affects the cross section results, thus this is a substantial source of uncertainties in the dipole formalism, showing the necessity of further studies regarding this part of the model. Additionally, it is worth noting that the results obtained with the solution of the BK equation are constrained to $y < 1.5$ due to limitations stemming from the finite grid range in [63].

In Fig. 36, the differential cross section is displayed as a function of the rapidity for the incoherent $\psi(1S)$ (left) and $\psi(2S)$ (right) photoproduction at 2.76 TeV. Again, it was used in the calculations the GBW model together with the five potentials. The results for the ground state were compared with the single data point available at the moment from the ALICE collaboration [6]. In this case, one can see that the curves were not capable of describing the data point shown in the left panel of the figure. This evidences that the developed formalism was not enough to deal with the incoherent production, ergo, new studies and theoretical

Figure 35 – Predictions for the rapidity distribution for the coherent $\Upsilon(1S)$ photoproduction in PbPb UPCs at 5.02 TeV. The results were obtained with 5 parameterizations for the dipole cross section together with vector meson wave functions obtained with 2 different potentials: the Cornell (darker curves) and the harmonic oscillator (lighter curves).

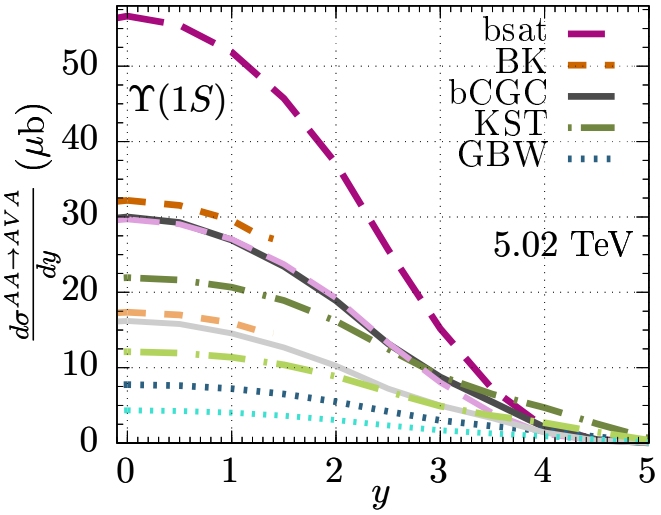

Source: Elaborated by the author.

analyses must be undertaken to solve this problem.

Figure 36 – Rapidity distribution for the incoherent $\psi(1S)$ (left) and $\psi(2S)$ (right) photoproduction in PbPb UPCs at 2.76 TeV. The ground state results were compared to the only available datapoint from ALICE collaboration [6].

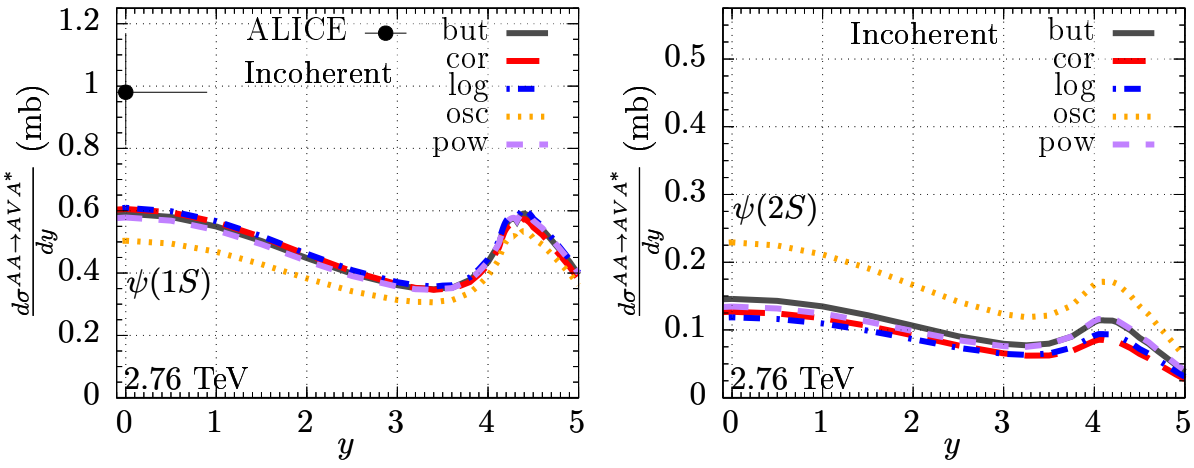

Source: Elaborated by the author and published in [11].

Lastly, Fig. 37 presents predictions for the differential cross section as a function of the rapidity for the incoherent $\Upsilon(1S)$ (left) and $\Upsilon(2S)$ (right) photoproduction at 5.02 TeV at PbPb collisions. Once again, a spread can be observed among the curves computed with distinct potentials, which reinforces the previous statement that the $\Upsilon(1S)$ wave functions are considerably distinct from one another.

Figure 37 – Predictions for the rapidity distribution for the incoherent $\Upsilon(1S)$ (left) and $\Upsilon(2S)$ (right) photoproduction in PbPb UPCs at 5.02 TeV.

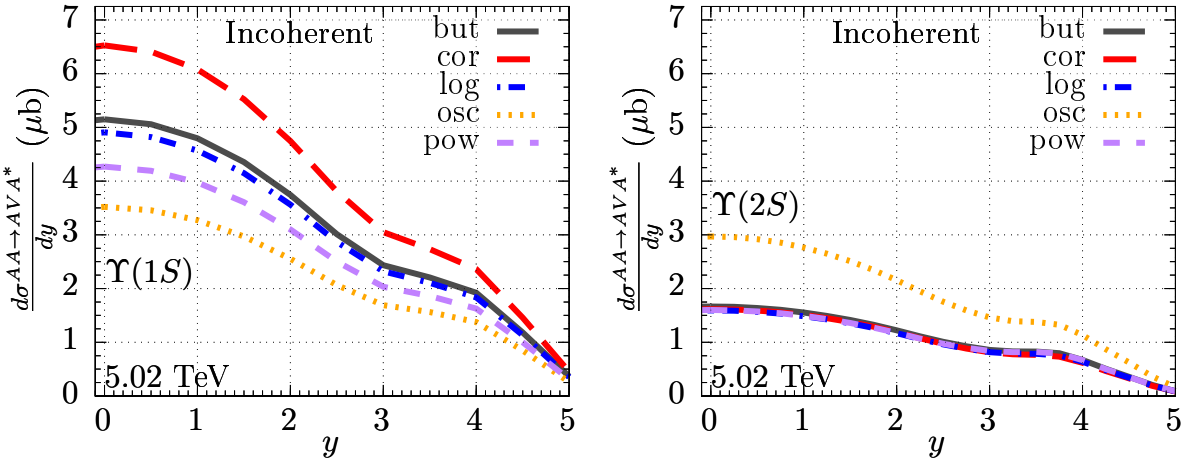

Source: Elaborated by the author and published in [11].

4.6.2 t- dependent heavy vector meson y- distributions

In this section, an extension of the previously discussed formalism will be presented for the computation of nuclear differential cross sections as a function of the transferred momentum t. The main motivation for this undertaking is the absence, in the literature, of any calculation of this quantity using the potential model for the vector meson wave function. Moreover, we wanted to investigate the impact of the gluon shadowing effect on such observables. Notably, this part of the work is original from this project, while the previous one (t-independent) was carried out in collaboration with another student; thus, it can also be seen in his dissertation [176].

In light of this, we will now present numerical results for the differential cross sections of coherent vector meson photoproduction as a function of $|t|$. Analogously to the previous section, the vector meson wave functions were computed with the potential approach and incorporating the Melosh spin rotation. However, since there were no noticeable differences between the curves obtained with different potentials, we chose only to display the ones obtained with the Buchmüller-Tye potential. The dipole-nucleus scattering amplitude was built up with the Glauber-Gribov approach and considering three parameterizations for the dipole-nucleon interaction cross section: the numerical solution of the BK-equation, the well-known phenomenological GBW model, and the saturated b-Sat model. Additionally, the gluon shadowing effect was taken into account through a phenomenological renormalization of the color dipole cross section.

The left panel of Fig. 38 presents a comparison between the results obtained for the differential cross section for $\psi(1S)$ coherent photoproduction and the recent ALICE data [177] at $\sqrt{s} = 5.02$ TeV. One can see that the curves slightly underestimate the data at very small $|t|$ values, whereas, for higher $|t|$, the results describe very well the available data. The right panel shows predictions for $\psi(2S)$ excited state, with the same setup and at the same energy.

Figure 38 – Differential cross sections for the $\gamma Pb \to \psi(nS)Pb$ process as functions of $|t|$. The results were obtained using the Buchmüller-Tye potential and three parameterizations for the $q\bar{q}$-nucleon interaction: BK, bSat, and GBW models. For the $\psi(1S)$ case, they were compared to the recent ALICE data [177].

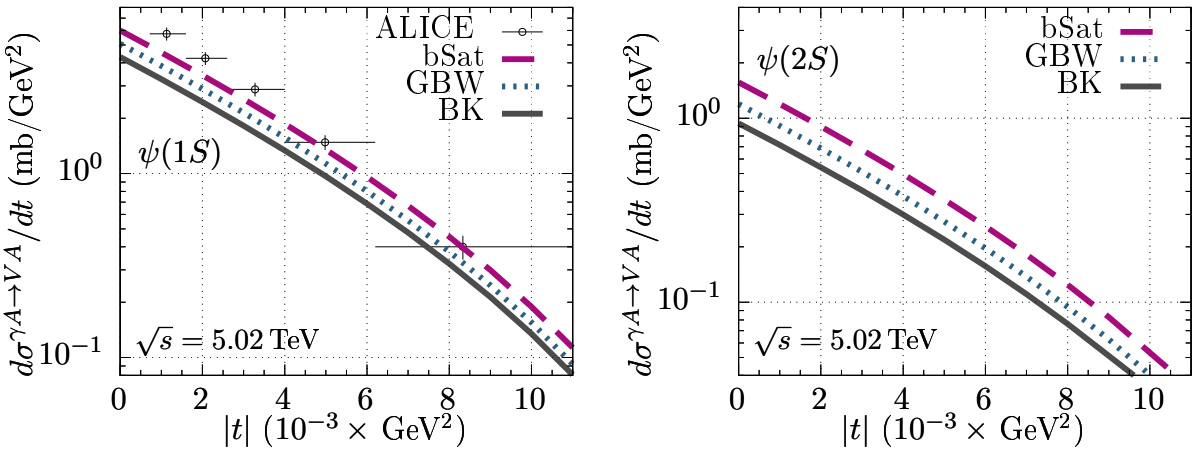

Source: Elaborated by the author and published in [38].

The left and right panels of Fig. 39 show the predicted differential cross section for coherent photoproduction of ψ and Υ states, respectively, in γPb collisions at $\sqrt{s} = 5.02$ TeV over a broader range of $|t|$. The nearly identical positions of the dips in both $\psi(1S, 2S)$ and $\Upsilon(1S, 2S)$ can be observed due to the destructive interference of individual nucleon scatterings within the nucleus. This shape only appears in coherent scatterings because, in this case, the photon interacts with the entire nucleus, allowing it to interact with all nucleons within it and ultimately result in a negative phase.

Figure 39 – Predictions for the differential cross section for the coherent photoproduction of ψ (left) and Υ (right) states in $\gamma Pb \to VPb$ collisions at $\sqrt{s} = 5.02$ TeV.

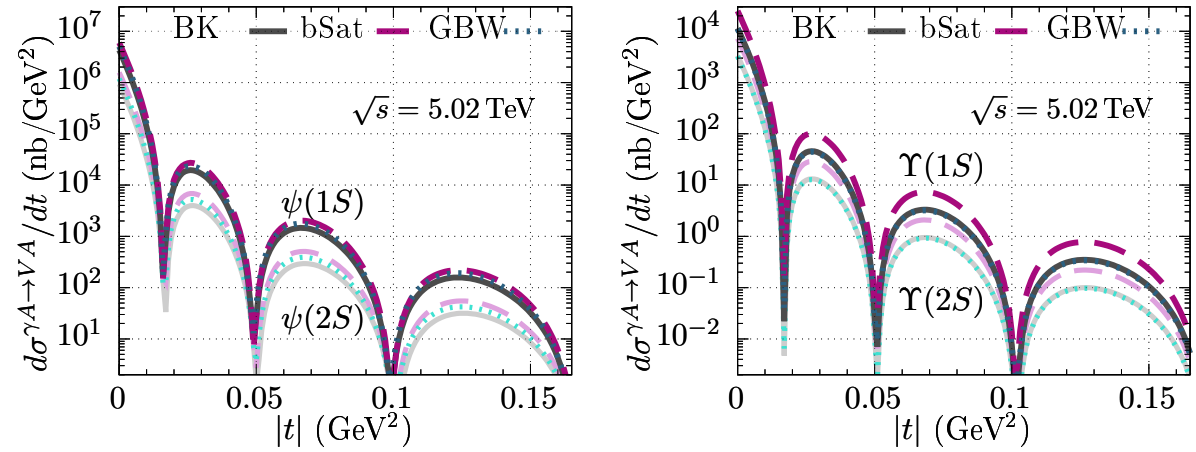

Source: Elaborated by the author and published in [38].

Lastly, in Fig. 40, predictions for the differential cross section for ψ (left) and Υ (right) states are presented for $PbPb \to VPbPb$ collisions at $\sqrt{s} = 5.02$ TeV and $y = 0$. These energy and rapidity values are compatible with those used in LHC, enhancing the chances of

being measured. A trivial thing to be noted is that these results have exactly the same shape as those found in Fig. 39, but are three orders of magnitude larger, which is caused by the Weizsäcker-Williams photon flux.

Figure 40 – Predictions for the differential cross section for the coherent photoproduction of ψ (left) and Υ (right) states in $PbPb \to VPbPb$ collisions at $\sqrt{s} = 5.02$ TeV and $y = 0$.

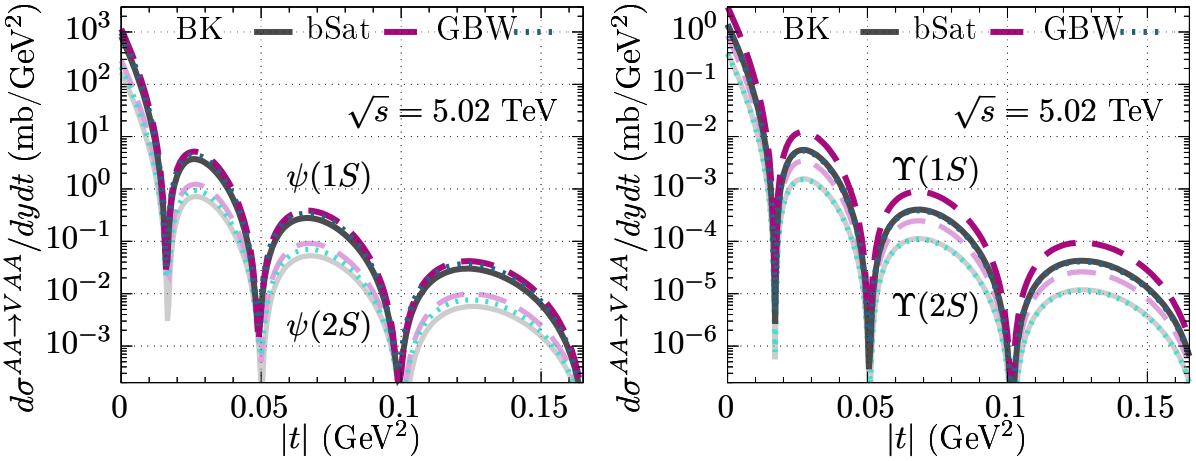

Source: Elaborated by the author and published in [38].

5 CONCLUSION

The main focus of this thesis was the study of exclusive photo and electroproduction of vector mesons with proton and nucleus targets through the color dipole formalism. An ideal goal would be to describe all five vector mesons presented in the text, ρ, ω, ϕ, ψ, and Υ, in both ground and excited states, with exactly the same model. However, the fact that these mesons have very different masses makes it necessary to study them separately and adjust the general formalism to each regime. This adjustment is made in the vector meson wave function, which is responsible for describing the combination of the $q\bar{q}$ pair into the vector meson. Thus, in this work, it was used two models for the wave function: the AdS/QCD holographic model for the light vector mesons and a potential approach (which consists of finding a solution for the Schrödinger equation in the $q\bar{q}$ rest frame for several interquark potentials and then boost it to the infinite momentum frame including the Melosh spin rotation) for the heavy ones. It is worth emphasizing that one of the main goals of the project was to study these vector meson cross sections using wave functions based on the theoretical fundaments of QCD. Another one was to obtain wave functions for the excited states. Both objectives were successfully accomplished with these two models.

For the light vector meson case, this formalism resulted in a very good description of the available data for $\rho(1S)$, $\omega(1S)$, and $\phi(1S)$ electroproduction cross sections. This showed the importance of a mass-dependent κ parameter in the effective confining potential, mostly for the obtention of the excellent ϕ results. In the photoproduction case, the differential cross section calculated with the same setup provided a good description of the available ZEUS data for the $\omega(1S)$ and the CMS data for $\rho(1S)$ production at small t. The calculation of total cross sections has revealed the existence of significant uncertainties related to the b-dependent partial dipole amplitude model employed. This highlights that the construction of such models should be improved considering these data and future measurements, like the production of excited states. For this reason, predictions were evaluated for the $\rho(2S)$, $\omega(2S)$, and $\phi(2S)$ photoproduction, which to the best of our knowledge, have not been found in the literature until the present moment.

With this formalism, it was possible to obtain an excellent description of all available data for the total cross section of $\psi(1S)$, $\psi(2S)$, and $\Upsilon(1S)$ photoproduction with a proton target using the GBW and KST dipole models. Despite the lack of data, predictions were made for the excited state $\Upsilon(2S)$ for completeness. Additionally, differential cross sections in t were calculated for the same four-vector mesons. However, to do so, it was necessary to utilize impact parameter-dependent partial dipole amplitude parameterizations. Thus, the b-Sat model and a solution of the BK equation were used to reproduce the H1 data (only available for J/ψ photoproduction), and it was observed that the latter achieved a better description.

Once the formalism for the proton target case had been well-established, it was decided

to extend it to the nucleus target case. For this purpose, the Glauber-Gribov model was used to account for the multiple scatterings of the dipole with the nucleus, including the effects of finite coherence length and gluon shadowing (adjusted to data). A summary with all models used in the present text can be found in Appendix A. Initially, the study focused on the coherent t-independent case, where the photon interacts with the entire nucleus. Remarkably, an excellent description of the J/ψ data from the CMS and ALICE experiments was obtained for ultraperipheral PbPb collisions at 2.76 TeV. However, for the ψ' state, only the harmonic potential was able to describe the single available data point from ALICE. For higher energies, a successful description was achieved only for LHCb data at 5.02 TeV, but it is important to note the tension between these data and those from ALICE. Predictions were also made for $\Upsilon(1S)$ and $\Upsilon(2S)$ at LHC energies, with the hope that future measurements could help determine the best interquark potential.

In the incoherent case, t-independent calculations were also performed for the same four vector mesons; however, they could only be compared to the single available data point for J/ψ photoproduction obtained by ALICE, which did not agree with the results. Nevertheless, it was deemed important to present these predictions, considering the well-known difficulty of describing incoherent processes in the literature. Therefore, the best description achieved with the formalism developed in this work was presented.

Finally, predictions were made for the t-dependent differential cross section for the coherent photoproduction of both ground and excited ψ and Υ states in nuclear collisions at central rapidity. The recently published ALICE data for J/ψ photoproduction made it possible to test the developed approach. They showed that, in contrast to the results obtained for proton targets, the bSat model provided a better description of this nuclear data than the other models, which once more evidenced the existent significant uncertainties in modeling the b-dependent color dipole cross section. These findings led to the publication of three articles [11, 38, 41]. Furthermore, given the success of this formalism in describing the coherent data from the LHC, it is expected that these predictions will play an important role in understanding future measurements of vector meson exclusive production at the LHC and at other future colliders, such as the EIC and the FCC.

6 FORTHCOMING RESEARCH

A natural continuation of the current work is the extension of the presented formalism to the coherent photoproduction of light vector mesons in nuclear collisions. However, in this scenario, their small mass poses a challenge for using the available parton distribution functions to evaluate the gluon shadowing effect, since the current fits only have an initial evolution scale $\mu_0 = m_c$. Thus, an adequate approach must be developed to accurately describe the gluon shadowing in light vector mesons. The recent measurements [178, 179, 180] from ALICE collaboration for coherent ρ photoproduction can serve as a valuable testbed for validating the proposed formalism.

Since the formalism adopted in this work did not provide a satisfactory description of the single available incoherent data in ultraperipheral collisions, it is evident that an improvement in the theoretical approach is necessary. Some recent works have attempted to incorporate the description of the fluctuations of the nucleus constituents [158, 181] into their models. While this approach may provide a suitable solution for the incoherent case, it leads to a worsened description of the coherent case. Thus, a model refinement is crucial to enable the description of this and the forthcoming data for both incoherent and coherent processes within the dipole formalism.

Finally, the advanced understanding of the dipole formalism can be useful in developing a theoretical model capable of describing a phenomenon observed in pp collisions at TOTEM [182] and ATLAS [183], known as "hollowness" [184, 185, 186, 187, 188]. This phenomenon reveals that at high energies, the inelasticity density does not reach its maximum when the impact parameter is zero but when it is small.

BIBLIOGRAPHY

[1] M. Klein and R. Yoshida. "Collider Physics at HERA". *Prog. Part. Nucl. Phys.* 61 2008, pp. 343–393. DOI: 10.1016/j.ppnp.2008.05.002. arXiv: 0805.3334 [hep-ex].

[2] H. Kowalski, L. Motyka, and G. Watt. "Exclusive diffractive processes at HERA within the dipole picture". *Phys. Rev. D* 74 074016, 2006. DOI: 10.1103/PhysRevD.74.074016. arXiv: hep-ph/0606272.

[3] A. H. Rezaeian and I. Schmidt. "Impact-parameter dependent Color Glass Condensate dipole model and new combined HERA data". *Phys. Rev. D* 88 2013, p. 074016. DOI: 10.1103/PhysRevD.88.074016. arXiv: 1307.0825 [hep-ph].

[4] J. Cepila, J. Nemchik, M. Krelina, and R. Pasechnik. "Theoretical uncertainties in exclusive electroproduction of S-wave heavy quarkonia". *Eur. Phys. J. C* 79.6 2019, p. 495. DOI: 10.1140/epjc/s10052-019-7016-9. arXiv: 1901.02664 [hep-ph].

[5] V. Khachatryan et al. [CMS]. "Coherent J/ψ photoproduction in ultra-peripheral PbPb collisions at $\sqrt{s_{NN}} = 2.76$ TeV with the CMS experiment". *Phys. Lett. B* 772 2017, pp. 489–511. DOI: 10.1016/j.physletb.2017.07.001. arXiv: 1605.06966 [nucl-ex].

[6] E. Abbas et al. [ALICE]. "Charmonium and e^+e^- pair photoproduction at mid-rapidity in ultra-peripheral Pb-Pb collisions at $\sqrt{s_{\mathrm{NN}}} = 2.76$ TeV". *Eur. Phys. J. C* 73.11 2013, p. 2617. DOI: 10.1140/epjc/s10052-013-2617-1. arXiv: 1305.1467 [nucl-ex].

[7] B. Abelev et al. [ALICE]. "Coherent J/ψ photoproduction in ultra-peripheral Pb-Pb collisions at $\sqrt{s_{NN}} = 2.76$ TeV". *Phys. Lett. B* 718 2013, pp. 1273–1283. DOI: 10.1016/j.physletb.2012.11.059. arXiv: 1209.3715 [nucl-ex].

[8] J. Adam et al. [ALICE]. "Coherent ψ(2S) photoproduction in ultra-peripheral PbPb collisions at $\sqrt{s_{\mathrm{NN}}} = 2.76$ TeV". *Phys. Lett. B* 751 2015, pp. 358–370. DOI: 10.1016/j.physletb.2015.10.040. arXiv: 1508.05076 [nucl-ex].

[9] S. Acharya et al. [ALICE]. "Coherent J/ψ photoproduction at forward rapidity in ultra-peripheral Pb-Pb collisions at $\sqrt{s_{\mathrm{NN}}} = 5.02$ TeV". *Phys. Lett. B* 798 134926, 2019. DOI: 10.1016/j.physletb.2019.134926. arXiv: 1904.06272 [nucl-ex].

[10] A. Bursche [LHCb]. "Study of coherent J/ψ production in lead-lead collisions at $\sqrt{s_{\mathrm{NN}}} = 5$ TeV with the LHCb experiment". *Nucl. Phys. A* 982 2019, pp. 247–250. DOI: 10.1016/j.nuclphysa.2018.10.069.

[11] C. Henkels, E. G. de Oliveira, R. Pasechnik, and H. Trebien. "Exclusive photoproduction of excited quarkonia in ultraperipheral collisions". *Phys. Rev. D* 102.1 014024, 2020. DOI: 10.1103/PhysRevD.102.014024. arXiv: 2004.00607 [hep-ph].

[12] S. J. Brodsky, G. F. de Teramond, H. G. Dosch, and J. Erlich. "Light-Front Holographic QCD and Emerging Confinement". *Phys. Rept.* 584 2015, pp. 1–105. DOI: 10.1016/j.physrep.2015.05.001. arXiv: 1407.8131 [hep-ph].

[13] S. J. Brodsky and G. F. de Teramond. "Light-Front Holography and Novel Effects in QCD". *AIP Conf. Proc.* 1116.1 2009, pp. 311–326. DOI: 10.1063/1.3131569. arXiv: 0812.3192 [hep-ph].

[14] E. M. Riordan. "The Discovery of quarks". *Science* 256 1992, pp. 1287–1293. DOI: 10.1126/science.256.5061.1287.

[15] A. Arbuzov. "Quantum Field Theory and the Electroweak Standard Model". *Proceedings, 2015 European School of High-Energy Physics (ESHEP2015)*. CERN Yellow Reports: School Proceedings 4 2017, pp. 1–34. DOI: 10.23730/CYRSP-2017-004.1. arXiv: 1801.05670 [hep-ph].

[16] D. J. Griffiths. *Introduction to electrodynamics; 4th ed.* Re-published by Cambridge University Press in 2017. Boston, MA: Pearson, 2013. DOI: 1108420419.

[17] G. Elert. "The Physics Hypertextbook". 1998–2020. Chap. standard.

[18] J. E. Ottoni. "Teorias de Calibre e Modelos de Unificação". Dissertação de Mestrado. UFMG, 2002.

[19] Z. Conesa Del Valle. "Performance of the ALICE muon spectrometer. Weak boson production and measurement in heavy-ion collisions at LHC". PhD thesis. Nantes U., 2007.

[20] P. Zyla et al. [Particle Data Group]. "Review of Particle Physics". *PTEP* 2020.8 083C01, 2020. DOI: 10.1093/ptep/ptaa104.

[21] S. Glazov [H1]. "Measurement of DIS cross section at HERA". *Braz. J. Phys.* 37 2007, pp. 793–797. DOI: 10.1590/S0103-97332007000500030.

[22] R. Devenish and A. Cooper-Sarkar. *Deep inelastic scattering*. 2004. DOI: 10.1093/acprof:oso/9780198506713.001.0001.

[23] G. M. Peccini. "Exclusive processes described by QCD at electron-ion colliders*". PhD thesis. UFRGS, 2022.

[24] R. D. Ball et al. [PDF4LHC Working Group]. "The PDF4LHC21 combination of global PDF fits for the LHC Run III". *J. Phys. G* 49.8 2022, p. 080501. DOI: 10.1088/1361-6471/ac7216. arXiv: 2203.05506 [hep-ph].

[25] I. P. Ivanov, N. N. Nikolaev, and A. A. Savin. "Diffractive vector meson production at HERA: From soft to hard QCD". *Phys. Part. Nucl.* 37 2006, pp. 1–85. DOI: 10.1134/S1063779606010011. arXiv: hep-ph/0501034.

[26] J. Nemchik, N. N. Nikolaev, E. Predazzi, and B. G. Zakharov. "Color dipole phenomenology of diffractive electroproduction of light vector mesons at HERA". *Z. Phys. C* 75 1997, pp. 71–87. DOI: 10.1007/s002880050448. arXiv: hep-ph/9605231.

[27] S. Navin. "Diffraction in Pythia" 2010. arXiv: 1005.3894 [hep-ph].

[28] A. Watson. "HERA Physicists Finally Put Flesh on a Putative Particle". *Science* 269.5226 1995, pp. 919–920. DOI: 10.1126/science.269.5226.919.

[29] B. Kopeliovich, L. Lapidus, and A. Zamolodchikov. "Dynamics of Color in Hadron Diffraction on Nuclei". *JETP Lett.* 33 1981, pp. 595–597.

[30] R. Aaij et al. [LHCb]. "Central exclusive production of J/ψ and $\psi(2S)$ mesons in pp collisions at $\sqrt{s} = 13$ TeV". *JHEP* 10 2018, p. 167. DOI: 10.1007/JHEP10(2018)167. arXiv: 1806.04079 [hep-ex].

[31] F. Willeke. "Electron Ion Collider Conceptual Design Report 2021" 2021. DOI: 10.2172/1765663.

[32] B. Z. Kopeliovich, M. Krelina, J. Nemchik, and I. K. Potashnikova. "Coherent photoproduction of heavy quarkonia on nuclei". *Phys. Rev. D* 105.5 2022, p. 054023. DOI: 10.1103/PhysRevD.105.054023. arXiv: 2201.13021 [hep-ph].

[33] V. Barone and E. Predazzi. *High-Energy Particle Diffraction*. Vol. 565. Texts and Monographs in Physics. Berlin Heidelberg: Springer-Verlag, 2002.

[34] V. P. Gonçalves, M. V. T. Machado, B. D. Moreira, F. S. Navarra, and G. S. dos Santos. "Color dipole predictions for the exclusive vector meson photoproduction in pp , pPb , and PbPb collisions at run 2 LHC energies". *Phys. Rev. D* 96.9 2017, p. 094027. DOI: 10.1103/PhysRevD.96.094027. arXiv: 1710.10070 [hep-ph].

[35] V. P. Gonçalves and B. D. Moreira. "A phenomenological analysis of the nonperturbative QCD contributions for the photon wave function". *Eur. Phys. J. C* 80.6 2020, p. 492. DOI: 10.1140/epjc/s10052-020-8043-2. arXiv: 2003.11438 [hep-ph].

[36] H. Mäntysaari and B. Schenke. "Probing subnucleon scale fluctuations in ultraperipheral heavy ion collisions". *Phys. Lett. B* 772 2017, pp. 832–838. DOI: 10.1016/j.physletb.2017.07.063. arXiv: 1703.09256 [hep-ph].

[37] T. Toll and T. Ullrich. "Exclusive diffractive processes in electron-ion collisions". *Phys. Rev. C* 87.2 2013, p. 024913. DOI: 10.1103/PhysRevC.87.024913. arXiv: 1211.3048 [hep-ph].

[38] C. Henkels, E. G. de Oliveira, R. Pasechnik, and H. Trebien. "Momentum transfer squared dependence of exclusive quarkonia photoproduction in ultraperipheral collisions". *Phys. Rev. D* 104.5 2021, p. 054008. DOI: 10.1103/PhysRevD.104.054008. arXiv: 2009.14158 [hep-ph].

[39] Y. Hatta, B.-W. Xiao, and F. Yuan. "Gluon Tomography from Deeply Virtual Compton Scattering at Small-x". *Phys. Rev. D* 95.11 2017, p. 114026. DOI: 10.1103/PhysRevD.95.114026. arXiv: 1703.02085 [hep-ph].

[40] J. Bartels, K. J. Golec-Biernat, and K. Peters. "On the dipole picture in the nonforward direction". *Acta Phys. Polon. B* 34 2003, pp. 3051–3068. arXiv: hep-ph/0301192.

[41] C. Henkels, E. G. de Oliveira, R. Pasechnik, and H. Trebien. "Exclusive photo- and electroproduction of excited light vector mesons via holographic model". *Eur. Phys. J. C* 83.6 2023, p. 551. DOI: 10.1140/epjc/s10052-023-11706-5. arXiv: 2207.13756 [hep-ph].

[42] J. Hufner, Y. Ivanov, B. Kopeliovich, and A. Tarasov. "Photoproduction of charmonia and total charmonium proton cross-sections". *Phys. Rev. D* 62 094022, 2000. DOI: 10.1103/PhysRevD.62.094022. arXiv: hep-ph/0007111.

[43] J. Bronzan, G. L. Kane, and U. P. Sukhatme. "Obtaining Real Parts of Scattering Amplitudes Directly from Cross-Section Data Using Derivative Analyticity Relations". *Phys. Lett. B* 49 1974, pp. 272–276. DOI: 10.1016/0370-2693(74)90432-8.

[44] R. Avila, E. Luna, and M. Menon. "High-energy proton proton forward scattering and derivative analyticity relations". *Braz. J. Phys.* 31 2001, pp. 567–576. DOI: 10.1590/S0103-97332001000400007. arXiv: hep-ph/0105065.

[45] A. Shuvaev, K. J. Golec-Biernat, A. D. Martin, and M. Ryskin. "Off diagonal distributions fixed by diagonal partons at small x and ξ". *Phys. Rev. D* 60 014015, 1999. DOI: 10.1103/PhysRevD.60.014015. arXiv: hep-ph/9902410.

[46] K. J. Golec-Biernat and M. Wusthoff. "Saturation effects in deep inelastic scattering at low Q^2 and its implications on diffraction". *Phys. Rev. D* 59 014017, 1998. DOI: 10.1103/PhysRevD.59.014017. arXiv: hep-ph/9807513 [hep-ph].

[47] K. J. Golec-Biernat and M. Wusthoff. "Saturation in diffractive deep inelastic scattering". *Phys. Rev. D* 60 114023, 1999. DOI: 10.1103/PhysRevD.60.114023. arXiv: hep-ph/9903358 [hep-ph].

[48] K. Golec-Biernat and S. Sapeta. "Saturation model of DIS : an update". *JHEP* 03 2018, p. 102. DOI: 10.1007/JHEP03(2018)102. arXiv: 1711.11360 [hep-ph].

[49] B. Z. Kopeliovich, A. Schafer, and A. V. Tarasov. "Nonperturbative effects in gluon radiation and photoproduction of quark pairs". *Phys. Rev. D* 62 054022, 2000. DOI: 10.1103/PhysRevD.62.054022. arXiv: hep-ph/9908245.

[50] B. Z. Kopeliovich, I. K. Potashnikova, I. Schmidt, and J. Soffer. "Damping of forward neutrons in pp collisions". *Phys. Rev. D* 78 2008, p. 014031. DOI: 10.1103/PhysRevD.78.014031. arXiv: 0805.4534 [hep-ph].

[51] S. R. Amendolia et al. "A Measurement of the Pion Charge Radius". *Phys. Lett. B* 146 1984, pp. 116–120. DOI: 10.1016/0370-2693(84)90655-5.

[52] H. Kowalski and D. Teaney. "An Impact parameter dipole saturation model". *Phys. Rev. D* 68 114005, 2003. DOI: 10.1103/PhysRevD.68.114005. arXiv: hep-ph/0304189.

[53] S. Chekanov et al. [ZEUS]. "Measurement of the neutral current cross-section and F(2) structure function for deep inelastic e^+p scattering at HERA". *Eur. Phys. J. C* 21 2001, pp. 443–471. DOI: 10.1007/s100520100749. arXiv: hep-ex/0105090.

[54] C. Adloff et al. [H1]. "Deep inelastic inclusive ep scattering at low x and a determination of $\alpha(s)$". *Eur. Phys. J. C* 21 2001, pp. 33–61. DOI: 10.1007/s100520100720. arXiv: hep-ex/0012053.

[55] Y. L. Dokshitzer. "Calculation of the Structure Functions for Deep Inelastic Scattering and e^+e^- Annihilation by Perturbation Theory in Quantum Chromodynamics." *Sov. Phys. JETP* 46 1977, pp. 641–653.

[56] V. Gribov and L. Lipatov. "Deep inelastic e p scattering in perturbation theory". *Sov. J. Nucl. Phys.* 15 1972, pp. 438–450.

[57] G. Altarelli and G. Parisi. "Asymptotic Freedom in Parton Language". *Nucl. Phys. B* 126 1977, pp. 298–318. DOI: 10.1016/0550-3213(77)90384-4.

[58] S. Dulat et al. "New parton distribution functions from a global analysis of quantum chromodynamics". *Phys. Rev. D* 93.3 033006, 2016. DOI: 10.1103/PhysRevD.93.033006. arXiv: 1506.07443 [hep-ph].

[59] V. P. Gonçalves. "QCD at high parton density". *Brazilian Journal of Physics* 34 2004, pp. 1406–1415. DOI: 10.1590/S0103-97332004000700018.

[60] I. Balitsky. "Operator expansion for high-energy scattering". *Nucl. Phys. B* 463 1996, pp. 99–160. DOI: 10.1016/0550-3213(95)00638-9. arXiv: hep-ph/9509348.

[61] Y. V. Kovchegov. "Unitarization of the BFKL pomeron on a nucleus". *Phys. Rev. D* 61 074018, 2000. DOI: 10.1103/PhysRevD.61.074018. arXiv: hep-ph/9905214.

[62] Y. V. Kovchegov. "Small $xF(2)$ structure function of a nucleus including multiple pomeron exchanges". *Phys. Rev. D* 60 034008, 1999. DOI: 10.1103/PhysRevD.60.034008. arXiv: hep-ph/9901281.

[63] D. Bendova, J. Cepila, J. Contreras, and M. Matas. "Solution to the Balitsky-Kovchegov equation with the collinearly improved kernel including impact-parameter dependence". *Phys. Rev. D* 100.5 054015, 2019. DOI: 10.1103/PhysRevD.100.054015. arXiv: 1907.12123 [hep-ph].

[64] E. Iancu, J. D. Madrigal, A. H. Mueller, G. Soyez, and D. N. Triantafyllopoulos. "Collinearly-improved BK evolution meets the HERA data". *Phys. Lett. B* 750 2015,

pp. 643–652. DOI: 10.1016/j.physletb.2015.09.071. arXiv: 1507.03651 [hep-ph].

[65] E. Iancu, K. Itakura, and S. Munier. "Saturation and BFKL dynamics in the HERA data at small x". *Phys. Lett. B* 590 2004, pp. 199–208. DOI: 10.1016/j.physletb.2004.02.040. arXiv: hep-ph/0310338.

[66] E. Levin and K. Tuchin. "Solution to the evolution equation for high parton density QCD". *Nucl. Phys. B* 573 2000, pp. 833–852. DOI: 10.1016/S0550-3213(99)00825-1. arXiv: hep-ph/9908317.

[67] G. Watt and H. Kowalski. "Impact parameter dependent colour glass condensate dipole model". *Phys. Rev. D* 78 2008, p. 014016. DOI: 10.1103/PhysRevD.78.014016. arXiv: 0712.2670 [hep-ph].

[68] S. D. Drell and T.-M. Yan. "Connection of Elastic Electromagnetic Nucleon Form-Factors at Large Q^2 and Deep Inelastic Structure Functions Near Threshold". *Phys. Rev. Lett.* 24 1970, pp. 181–185. DOI: 10.1103/PhysRevLett.24.181.

[69] G. B. West. "Phenomenological model for the electromagnetic structure of the proton". *Phys. Rev. Lett.* 24 1970, pp. 1206–1209. DOI: 10.1103/PhysRevLett.24.1206.

[70] S. J. Brodsky and G. R. Farrar. "Scaling Laws at Large Transverse Momentum". *Phys. Rev. Lett.* 31 1973, pp. 1153–1156. DOI: 10.1103/PhysRevLett.31.1153.

[71] J. Raufeisen, J.-C. Peng, and G. C. Nayak. "Parton model versus color dipole formulation of the Drell-Yan process". *Phys. Rev. D* 66 034024, 2002. DOI: 10.1103/PhysRevD.66.034024. arXiv: hep-ph/0204095 [hep-ph].

[72] K. Kutak and J. Kwiecinski. "Screening effects in the ultrahigh-energy neutrino interactions". *Eur. Phys. J. C* 29 2003, p. 521. DOI: 10.1140/epjc/s2003-01236-y. arXiv: hep-ph/0303209 [hep-ph].

[73] J. B. Kogut and D. E. Soper. "Quantum Electrodynamics in the Infinite Momentum Frame". *Phys. Rev. D* 1 1970, pp. 2901–2913. DOI: 10.1103/PhysRevD.1.2901.

[74] J. Bjorken, J. B. Kogut, and D. E. Soper. "Quantum Electrodynamics at Infinite Momentum: Scattering from an External Field". *Phys. Rev. D* 3 1971, p. 1382. DOI: 10.1103/PhysRevD.3.1382.

[75] H. G. Dosch, T. Gousset, G. Kulzinger, and H. Pirner. "Vector meson leptoproduction and nonperturbative gluon fluctuations in QCD". *Phys. Rev. D* 55 1997, pp. 2602–2615. DOI: 10.1103/PhysRevD.55.2602. arXiv: hep-ph/9608203.

[76] J. R. Forshaw, R. Sandapen, and G. Shaw. "Color dipoles and ρ, ϕ electroproduction". *Phys. Rev. D* 69 094013, 2004. DOI: 10.1103/PhysRevD.69.094013. arXiv: hep-ph/0312172.

[77] G. P. Lepage and S. J. Brodsky. "Exclusive Processes in Perturbative Quantum Chromodynamics". *Phys. Rev. D* 22 1980, p. 2157. DOI: 10.1103/PhysRevD.22.2157.

[78] N. N. Nikolaev and B. G. Zakharov. "Color transparency and scaling properties of nuclear shadowing in deep inelastic scattering". *Z. Phys. C* 49 1991, pp. 607–618. DOI: 10.1007/BF01483577.

[79] T. Lappi, H. Mäntysaari, and J. Penttala. "Relativistic corrections to the vector meson light front wave function". *Phys. Rev. D* 102.5 2020, p. 054020. DOI: 10.1103/PhysRevD.102.054020. arXiv: 2006.02830 [hep-ph].

[80] T. Lappi, H. Mäntysaari, and J. Penttala. "Higher-order corrections to exclusive heavy vector meson production". *SciPost Phys. Proc.* 8 2022, p. 133. DOI: 10.21468/SciPostPhysProc.8.133. arXiv: 2106.12825 [hep-ph].

[81] G. Sampaio dos Santos and M. V. T. Machado. "Light vector meson photoproduction in hadron-hadron and nucleus-nucleus collisions at energies available at the CERN Large Hadron Collider". *Phys. Rev. C* 91.2 2015, p. 025203. DOI: 10.1103/PhysRevC.91.025203. arXiv: 1407.4148 [hep-ph].

[82] I. P. Ivanov. "Diffractive production of S and D wave vector mesons in deep inelastic scattering". Other thesis. 1999. arXiv: hep-ph/9909394.

[83] L. Frankfurt, W. Koepf, and M. Strikman. "Diffractive heavy quarkonium photoproduction and electroproduction in QCD". *Phys. Rev. D* 57 1998, pp. 512–526. DOI: 10.1103/PhysRevD.57.512. arXiv: hep-ph/9702216.

[84] J. R. Forshaw and D. A. Ross. *Diffraction*. Cambridge Lecture Notes in Physics. Cambridge: Cambridge University Press, 1997, pp. 175–203. DOI: 10.1017/CBO9780511524387.008.

[85] S. Chekanov et al. [ZEUS]. "Exclusive rho0 production in deep inelastic scattering at HERA". *PMC Phys. A* 1 2007, p. 6. DOI: 10.1186/1754-0410-1-6. arXiv: 0708.1478 [hep-ex].

[86] T. Berndt. "Exclusive pomeron and odderon induced photoproduction of omega and f2 mesons at HERA". Dissertação de Mestrado. 2002. DOI: 10.3204/DESY-THESIS-2002-031.

[87] C. Alexa et al. [H1]. "Elastic and Proton-Dissociative Photoproduction of J/ψ Mesons at HERA". *Eur. Phys. J. C* 73.6 2013, p. 2466. DOI: 10.1140/epjc/s10052-013-2466-y. arXiv: 1304.5162 [hep-ex].

[88] A. Aktas et al. [H1]. "Elastic J/ψ production at HERA". *Eur. Phys. J. C* 46 2006, pp. 585–603. DOI: 10.1140/epjc/s2006-02519-5. arXiv: hep-ex/0510016 [hep-ex].

[89] S. Chekanov et al. [ZEUS]. "Exclusive photoproduction of J/ψ mesons at HERA". *Eur. Phys. J. C* 24 2002, pp. 345–360. DOI: 10.1007/s10052-002-0953-7. arXiv: hep-ex/0201043 [hep-ex].

[90] S. Chekanov et al. [ZEUS]. "Exclusive electroproduction of J/ψ mesons at HERA". *Nucl. Phys. B* 695 2004, pp. 3–37. DOI: 10.1016/j.nuclphysb.2004.06.034. arXiv: hep-ex/0404008.

[91] F. D. Aaron et al. [H1]. "Diffractive Electroproduction of rho and phi Mesons at HERA". *JHEP* 05 2010, p. 032. DOI: 10.1007/JHEP05(2010)032. arXiv: 0910.5831 [hep-ex].

[92] A. M. Sirunyan et al. [CMS]. "Measurement of exclusive $\rho(770)^0$ photoproduction in ultraperipheral pPb collisions at $\sqrt{s_{\mathrm{NN}}} = 5.02$ TeV". *Eur. Phys. J. C* 79.8 2019, p. 702. DOI: 10.1140/epjc/s10052-019-7202-9. arXiv: 1902.01339 [hep-ex].

[93] J. Nemchik, N. N. Nikolaev, E. Predazzi, B. G. Zakharov, and V. R. Zoller. "The Diffraction cone for exclusive vector meson production in deep inelastic scattering". *J. Exp. Theor. Phys.* 86 1998, pp. 1054–1073. DOI: 10.1134/1.558573. arXiv: hep-ph/9712469.

[94] J. R. Forshaw and R. Sandapen. "Extracting the rho meson wavefunction from HERA data". *JHEP* 11 2010, p. 037. DOI: 10.1007/JHEP11(2010)037. arXiv: 1007.1990 [hep-ph].

[95] M. Ahmady, R. Sandapen, and N. Sharma. "Diffractive ρ and ϕ production at HERA using a holographic AdS/QCD light-front meson wave function". *Phys. Rev. D* 94.7 2016, p. 074018. DOI: 10.1103/PhysRevD.94.074018. arXiv: 1605.07665 [hep-ph].

[96] J. R. Forshaw and R. Sandapen. "Extracting the Distribution Amplitudes of the rho meson from the Color Glass Condensate". *JHEP* 10 2011, p. 093. DOI: 10.1007/JHEP10(2011)093. arXiv: 1104.4753 [hep-ph].

[97] A. C. Caldwell and M. S. Soares. "Vector meson production in the Golec-Biernat Wusthoff model". *Nucl. Phys. A* 696 2001, pp. 125–137. DOI: 10.1016/S0375-9474(01)01117-4. arXiv: hep-ph/0101085.

[98] S. J. Brodsky, T. Huang, and G. P. Lepage. "Hadronic and nuclear interactions in QCD". *Springer Tracts Mod. Phys.* 100 1982, pp. 81–144.

[99] T. Huang, B.-Q. Ma, and Q.-X. Shen. "Analysis of the pion wave function in light cone formalism". *Phys. Rev. D* 49 1994, pp. 1490–1499. DOI: 10.1103/PhysRevD.49.1490. arXiv: hep-ph/9402285.

[100] M. Terentev. "On the Structure of Wave Functions of Mesons as Bound States of Relativistic Quarks". *Sov. J. Nucl. Phys.* 24 1976, p. 106.

[101] O. Benhar, B. Z. Kopeliovich, C. Mariotti, N. N. Nicolaev, and B. G. Zakharov. "Why photoproduction of charmonium on nuclei does not measure the charmonium nucleon total cross-section". *Phys. Rev. Lett.* 69 1992, pp. 1156–1159. DOI: 10.1103/PhysRevLett.69.1156.

[102] E. Schrödinger. "Quantisierung als Eigenwertproblem". *Annalen Phys.* 384.4 1926, pp. 361–376. DOI: 10.1002/andp.19263840404.

[103] W. Buchmuller and S. Tye. "Quarkonia and Quantum Chromodynamics". *Phys. Rev. D* 24 1981, p. 132. DOI: 10.1103/PhysRevD.24.132.

[104] E. Eichten, K. Gottfried, T. Kinoshita, K. Lane, and T.-M. Yan. "Charmonium: Comparison with Experiment". *Phys. Rev. D* 21 1980, p. 203. DOI: 10.1103/PhysRevD.21.203.

[105] C. Quigg and J. L. Rosner. "Quarkonium Level Spacings". *Phys. Lett. B* 71 1977, pp. 153–157. DOI: 10.1016/0370-2693(77)90765-1.

[106] A. Martin. "A FIT of Υ and Charmonium Spectra". *Phys. Lett. B* 93 1980, pp. 338–342. DOI: 10.1016/0370-2693(80)90527-4.

[107] A. M. Sirunyan et al. [CMS]. "Measurement of exclusive Υ photoproduction from protons in pPb collisions at $\sqrt{s_{\mathrm{NN}}} = 5.02$ TeV". *Eur. Phys. J. C* 79.3 2019, p. 277. DOI: 10.1140/epjc/s10052-019-6774-8. arXiv: 1809.11080 [hep-ex].

[108] P. L. Frabetti et al. [E687]. "A Measurement of elastic J/ψ photoproduction cross-section at fermilab E687". *Phys. Lett.B* 316 1993, pp. 197–206. DOI: 10.1016/0370-2693(93)90679-C.

[109] B. H. Denby et al. "Inelastic and Elastic Photoproduction of J/ψ (3097)". *Phys. Rev. Lett.* 52 1984, pp. 795–798. DOI: 10.1103/PhysRevLett.52.795.

[110] M. E. Binkley et al. "J/ψ Photoproduction from 60-GeV/c to 300-GeV/c". *Phys. Rev. Lett.* 48 1982, p. 73. DOI: 10.1103/PhysRevLett.48.73.

[111] C. Adloff et al. [H1]. "Elastic photoproduction of J/ψ and Υ mesons at HERA". *Phys. Lett. B* 483 2000, pp. 23–35. DOI: 10.1016/S0370-2693(00)00530-X. arXiv: hep-ex/0003020 [hep-ex].

[112] J. Breitweg et al. [ZEUS]. "Measurement of elastic Υ photoproduction at HERA". *Phys. Lett. B* 437 1998, pp. 432–444. DOI: 10.1016/S0370-2693(98)01081-8. arXiv: hep-ex/9807020 [hep-ex].

[113] S. Chekanov et al. [ZEUS]. "Exclusive photoproduction of Υ mesons at HERA". *Phys. Lett. B* 680 2009, pp. 4–12. DOI: 10.1016/j.physletb.2009.07.066. arXiv: 0903.4205 [hep-ex].

[114] R. Aaij et al. [LHCb]. "Measurement of the exclusive Υ production cross-section in pp collisions at $\sqrt{s} = 7$ TeV and 8 TeV". *JHEP* 09 084, 2015. DOI: 10.1007/JHEP09(2015)084. arXiv: 1505.08139 [hep-ex].

[115] B. Z. Kopeliovich, M. Krelina, and J. Nemchik. "Electroproduction of heavy quarkonia: significance of dipole orientation". *Phys. Rev. D* 103.9 2021, p. 094027. DOI: 10.1103/PhysRevD.103.094027. arXiv: 2102.06106 [hep-ph].

[116] J. Nemchik, N. N. Nikolaev, and B. G. Zakharov. "Scanning the BFKL pomeron in elastic production of vector mesons at HERA". *Phys. Lett. B* 341 1994, pp. 228–237. DOI: 10.1016/0370-2693(94)90314-X. arXiv: hep-ph/9405355.

[117] G. 't Hooft. "Dimensional reduction in quantum gravity". *Conf. Proc. C* 930308 1993, pp. 284–296. arXiv: gr-qc/9310026.

[118] L. Susskind. "The World as a hologram". *J. Math. Phys.* 36 1995, pp. 6377–6396. DOI: 10.1063/1.531249. arXiv: hep-th/9409089.

[119] G. Mack and A. Salam. "Finite component field representations of the conformal group". *Annals Phys.* 53 1969, pp. 174–202. DOI: 10.1016/0003-4916(69)90278-4.

[120] A. Deur, V. Burkert, J.-P. Chen, and W. Korsch. "Experimental determination of the effective strong coupling constant". *Phys. Lett. B* 650 2007, pp. 244–248. DOI: 10.1016/j.physletb.2007.05.015. arXiv: hep-ph/0509113.

[121] D. Binosi and J. Papavassiliou. "Pinch Technique: Theory and Applications". *Phys. Rept.* 479 2009, pp. 1–152. DOI: 10.1016/j.physrep.2009.05.001. arXiv: 0909.2536 [hep-ph].

[122] L. von Smekal, R. Alkofer, and A. Hauck. "The Infrared behavior of gluon and ghost propagators in Landau gauge QCD". *Phys. Rev. Lett.* 79 1997, pp. 3591–3594. DOI: 10.1103/PhysRevLett.79.3591. arXiv: hep-ph/9705242.

[123] S. Furui and H. Nakajima. "Infrared features of unquenched finite temperature lattice Landau gauge QCD". *Phys. Rev. D* 76 2007, p. 054509. DOI: 10.1103/PhysRevD.76.054509. arXiv: hep-lat/0612009.

[124] A. Karch, E. Katz, D. T. Son, and M. A. Stephanov. "Linear confinement and AdS/QCD". *Phys. Rev. D* 74 2006, p. 015005. DOI: 10.1103/PhysRevD.74.015005. arXiv: hep-ph/0602229.

[125] R. Brustein. "The Role of the superstring dilaton in cosmology and particle physics". *29th Rencontres de Moriond: Electroweak Interactions and Unified Theories*. 1994, pp. 301–310. arXiv: hep-th/9405066.

[126] S. J. Brodsky and G. F. de Teramond. "AdS/CFT and Light-Front QCD". *Subnucl. Ser.* 45 2009, pp. 139–183. DOI: 10.1142/9789814293242_0008. arXiv: 0802.0514 [hep-ph].

[127] P. A. M. Dirac. "Forms of Relativistic Dynamics". *Rev. Mod. Phys.* 21 1949, pp. 392–399. DOI: 10.1103/RevModPhys.21.392.

[128] S. J. Brodsky, H.-C. Pauli, and S. S. Pinsky. "Quantum chromodynamics and other field theories on the light cone". *Phys. Rept.* 301 1998, pp. 299–486. DOI: 10.1016/S0370-1573(97)00089-6. arXiv: hep-ph/9705477.

[129] R. Jackiw and N. S. Manton. "Symmetries and Conservation Laws in Gauge Theories". *Annals Phys.* 127 1980, p. 257. DOI: 10.1016/0003-4916(80)90098-6.

[130] G. F. de Teramond and S. J. Brodsky. "Light-Front Holography: A First Approximation to QCD". *Phys. Rev. Lett.* 102 2009, p. 081601. DOI: 10.1103/PhysRevLett.102.081601. arXiv: 0809.4899 [hep-ph].

[131] S. J. Brodsky and G. F. de Teramond. "Hadronic spectra and light-front wavefunctions in holographic QCD". *Phys. Rev. Lett.* 96 2006, p. 201601. DOI: 10.1103/PhysRevLett.96.201601. arXiv: hep-ph/0602252.

[132] S. J. Brodsky and G. F. de Teramond. "Light-Front Dynamics and AdS/QCD Correspondence: The Pion Form Factor in the Space- and Time-Like Regions". *Phys. Rev. D* 77 2008, p. 056007. DOI: 10.1103/PhysRevD.77.056007. arXiv: 0707.3859 [hep-ph].

[133] A. Deur, S. J. Brodsky, and G. F. de Teramond. "Connecting the Hadron Mass Scale to the Fundamental Mass Scale of Quantum Chromodynamics". *Phys. Lett. B* 750 2015, pp. 528–532. DOI: 10.1016/j.physletb.2015.09.063. arXiv: 1409.5488 [hep-ph].

[134] A. Vega, I. Schmidt, T. Branz, T. Gutsche, and V. E. Lyubovitskij. "Meson wave function from holographic models". *Phys. Rev. D* 80 2009, p. 055014. DOI: 10.1103/PhysRevD.80.055014. arXiv: 0906.1220 [hep-ph].

[135] C. H. Lee, H.-Y. Ryu, and I. Zahed. "Diffractive Vector Photoproduction using Holographic QCD". *Phys. Rev. D* 98.5 2018, p. 056006. DOI: 10.1103/PhysRevD.98.056006. arXiv: 1804.09300 [hep-ph].

[136] R. L. Workman et al. [Particle Data Group]. "Review of Particle Physics". *PTEP* 2022 2022, p. 083C01. DOI: 10.1093/ptep/ptac097.

[137] J. R. Forshaw and R. Sandapen. "An AdS/QCD holographic wavefunction for the rho meson and diffractive rho meson electroproduction". *Phys. Rev. Lett.* 109 2012, p. 081601. DOI: 10.1103/PhysRevLett.109.081601. arXiv: 1203.6088 [hep-ph].

[138] J. R. Forshaw and R. Sandapen. "An AdS/QCD holographic wavefunction for the rho meson". *20th International Workshop on Deep-Inelastic Scattering and Related Subjects*. 2012, pp. 531–534. DOI: 10.3204/DESY-PROC-2012-02/265. arXiv: 1207.4358 [hep-ph].

[139] V. P. Gonçalves, D. E. Martins, and C. R. Sena. "Coherent and incoherent deeply virtual Compton scattering in electron–ion collisions at the EIC and LHeC". *Eur. Phys. J. A* 58.2 2022, p. 18. DOI: 10.1140/epja/s10050-022-00664-3.

[140] S. Aid et al. [H1]. "Elastic photoproduction of rho0 mesons at HERA". *Nucl. Phys. B* 463 1996, pp. 3–32. DOI: 10.1016/0550-3213(96)00045-4. arXiv: hep-ex/9601004.

[141] V. Andreev et al. [H1]. "Measurement of Exclusive $\pi^+\pi^-$ and ρ^0 Meson Photoproduction at HERA". *Eur. Phys. J. C* 80.12 2020, p. 1189. DOI: 10.1140/epjc/s10052-020-08587-3. arXiv: 2005.14471 [hep-ex].

[142] J. Breitweg et al. [ZEUS]. "Elastic and proton dissociative ρ^0 photoproduction at HERA". *Eur. Phys. J. C* 2 1998, pp. 247–267. DOI: 10.1007/s100520050136. arXiv: hep-ex/9712020.

[143] H. R. Crouch et al. [Brown-Harvard-MIT-Padova-Weizmann Institute Bubble Chamber Group]. "Photoproduction of ω^0 Mesons". *Phys. Rev.* 155 5, 1967, pp. 1468–1476. DOI: 10.1103/PhysRev.155.1468. Disponível em: https://link.aps.org/doi/10.1103/PhysRev.155.1468.

[144] R. Erbe et al. [Aachen-Berlin-Bonn-Hamburg-Heidelberg-Munich Collaboration]. "Photoproduction of Meson and Baryon Resonances at Energies up to 5.8 GEV". *Phys. Rev.* 175 1968, pp. 1669–1696. DOI: 10.1103/PhysRev.175.1669.

[145] M. Davier, I. Derado, D. J. Drickey, D. E. C. Fries, R. F. Mozley, A. Odian, F. Villa, and D. Yount. "MULTIBODY PHOTOPRODUCTION BETWEEN 2-GeV AND 16-GeV". *Phys. Rev. D* 1 1970, pp. 790–812. DOI: 10.1103/PhysRevD.1.790.

[146] J. Ballam et al. "STUDY OF HIGH-ENERGY PHOTOPRODUCTION WITH POSITRON ANNIHILATION RADIATION: I THREE PRONG EVENTS". *Phys. Rev. D* 5 1972, p. 15. DOI: 10.1103/PhysRevD.5.15.

[147] J. Ballam et al. "Vector Meson Production by Polarized Photons at 2.8-GeV, 4.7-GeV, and 9.3-GeV". *Phys. Rev. D* 7 1973, p. 3150. DOI: 10.1103/PhysRevD.7.3150.

[148] W. Struczinski et al. [Aachen-Hamburg-Heidelberg-Munich]. "Study of photoproduction on hydrogen in a streamer chamber with tagged photons for 1.6 GeV $< E_\gamma <$ 6.3 GeV Topological and reaction cross sections". *Nucl. Phys. B* 108 1976, pp. 45–74. DOI: 10.1016/0550-3213(76)90123-1.

[149] R. M. Egloff et al. "Measurement of ω Meson Photoproduction on Protons From 46 GeV to 180 GeV". *Phys. Rev. Lett.* 43 1979. [Erratum: Phys.Rev.Lett. 44, 690 (1980)], p. 1545. DOI: 10.1103/PhysRevLett.43.1545.

[150] A. M. Breakstone, D. C. Cheng, D. E. Dorfan, A. A. Grillo, C. A. Heusch, V. Palladino, T. Schalk, A. Seiden, and D. B. Smith. "QUASIELASTIC OMEGA PHOTOPRODUCTION

AT 50-GEV - 130-GEV". *Phys. Rev. Lett.* 47 1981, pp. 1782–1785. DOI: 10.1103/PhysRevLett.47.1782.

[151] D. Aston et al. [Bonn-CERN-EcolePoly-Glasgow-Lancaster-Manchester-Orsay-Paris-Rutherford-Sheffield]. "Photoproduction of ρ^0 and ω on Hydrogen at Photon Energies of 20-GeV to 70-GeV". *Nucl. Phys. B* 209 1982, pp. 56–76. DOI: 10.1016/0550-3213(82)90102-X.

[152] D. P. Barber et al. [LAMP2 Group]. "A STUDY OF THE REACTIONS GAMMA P —> OMEGA P AND GAMMA P —> OMEGA DELTA+". *Z. Phys. C* 26 1984, pp. 343–351. DOI: 10.1007/BF01452559.

[153] M. Atkinson et al. [Omega Photon Collaboration]. "Photoproduction of $\pi^+\pi^-\pi^0$ on Hydrogen With Linearly Polarized Photons of Energy 20-GeV - 70-GeV". *Nucl. Phys. B* 231 1984, pp. 15–39. DOI: 10.1016/0550-3213(84)90304-3.

[154] J. Busenitz et al. "High-energy Photoproduction of $\pi^+\pi^-\pi^0$, K^+K^-, and $P\bar{P}$ States". *Phys. Rev. D* 40 1989, pp. 1–21. DOI: 10.1103/PhysRevD.40.1.

[155] M. Derrick et al. [ZEUS]. "Measurement of elastic omega photoproduction at HERA". *Z. Phys. C* 73 1996, pp. 73–84. DOI: 10.1007/s002880050297. arXiv: hep-ex/9608010.

[156] J. Breitweg et al. [ZEUS]. "Measurement of exclusive omega electroproduction at HERA". *Phys. Lett. B* 487 2000, pp. 273–288. DOI: 10.1016/S0370-2693(00)00794-2. arXiv: hep-ex/0006013.

[157] S. Chekanov et al. [ZEUS]. "Exclusive electroproduction of phi mesons at HERA". *Nucl. Phys. B* 718 2005, pp. 3–31. DOI: 10.1016/j.nuclphysb.2005.04.009. arXiv: hep-ex/0504010.

[158] H. Mäntysaari. "Review of proton and nuclear shape fluctuations at high energy". *Rept. Prog. Phys.* 83.8 082201, 2020. DOI: 10.1088/1361-6633/aba347. arXiv: 2001.10705 [hep-ph].

[159] B. Kopeliovich. "Gribov inelastic shadowing in the dipole representation". *Int. J. Mod. Phys. A* 31.28n29 1645021, 2016. DOI: 10.1142/S0217751X16450214. arXiv: 1602.00298 [hep-ph].

[160] V. N. Gribov. "Interaction of gamma quanta and electrons with nuclei at high-energies". *Zh. Eksp. Teor. Fiz.* 57 1969, pp. 1306–1323.

[161] V. N. Gribov. "Glauber corrections and the interaction between high-energy hadrons and nuclei". *Sov. Phys. JETP* 29 1969, pp. 483–487.

[162] B. Kopeliovich and B. Zakharov. "Quantum effects and color transparency in charmonium photoproduction on nuclei". *Phys. Rev. D* 44 1991, pp. 3466–3472. DOI: 10.1103/PhysRevD.44.3466.

[163] R. D. Woods and D. S. Saxon. "Diffuse Surface Optical Model for Nucleon-Nuclei Scattering". *Phys. Rev.* 95 1954, pp. 577–578. DOI: 10.1103/PhysRev.95.577.

[164] H. Euteneuer, J. Friedrich, and N. Vogler. "The Charge Distribution Differences of Bi-209, Pb-208, Pb-207, Pb-206, Pb-204 and Tl-205, Tl-203 Investigated by Elastic electron Scattering and Muonic x-Ray Data". *Nucl. Phys. A* 298 1978, pp. 452–476. DOI: 10.1016/0375-9474(78)90143-4.

[165] B. Kopeliovich, M. Krelina, J. Nemchik, and I. Potashnikova. "Heavy quarkonium production in ultraperipheral nuclear collisions" 2020. arXiv: 2008.05116 [hep-ph].

[166] B. Kopeliovich, I. Potashnikova, and I. Schmidt. "Large rapidity gap processes in proton-nucleus collisions". *Phys. Rev. C* 73 034901, 2006. DOI: 10.1103/PhysRevC.73.034901. arXiv: hep-ph/0508277.

[167] Y. P. Ivanov, B. Kopeliovich, A. Tarasov, and J. Hufner. "Electroproduction of charmonia off protons and nuclei". *AIP Conf. Proc.* 660.1 2003, pp. 283–295. DOI: 10.1063/1.1570580. arXiv: hep-ph/0212322.

[168] Y. Ivanov, B. Kopeliovich, A. Tarasov, and J. Hufner. "Electroproduction of charmonia off nuclei". *Phys. Rev. C* 66 024903, 2002. DOI: 10.1103/PhysRevC.66.024903. arXiv: hep-ph/0202216.

[169] B. Kopeliovich, J. Nemchik, A. Schafer, and A. Tarasov. "Color transparency versus quantum coherence in electroproduction of vector mesons off nuclei". *Phys. Rev. C* 65 035201, 2002. DOI: 10.1103/PhysRevC.65.035201. arXiv: hep-ph/0107227.

[170] A. Abada et al. [FCC]. "FCC Physics Opportunities: Future Circular Collider Conceptual Design Report Volume 1". *Eur. Phys. J. C* 79.6 2019, p. 474. DOI: 10.1140/epjc/s10052-019-6904-3.

[171] V. Guzey, E. Kryshen, and M. Zhalov. "Coherent photoproduction of vector mesons in ultraperipheral heavy ion collisions: Update for run 2 at the CERN Large Hadron Collider". *Phys. Rev. C* 93.5 055206, 2016. DOI: 10.1103/PhysRevC.93.055206. arXiv: 1602.01456 [nucl-th].

[172] K. J. Eskola, P. Paakkinen, H. Paukkunen, and C. A. Salgado. "EPPS16: Nuclear parton distributions with LHC data". *Eur. Phys. J. C* 77.3 2017, p. 163. DOI: 10.1140/epjc/s10052-017-4725-9. arXiv: 1612.05741 [hep-ph].

[173] E. Fermi. "On the Theory of the impact between atoms and electrically charged particles". *Z. Phys.* 29 1924, pp. 315–327. DOI: 10.1007/BF03184853.

[174] J. D. Jackson. *Classical electrodynamics*. 3 ed. New York, NY: Wiley, 1999. Disponível em: http://cdsweb.cern.ch/record/490457.

[175] C. A. Bertulani, S. R. Klein, and J. Nystrand. "Physics of ultra-peripheral nuclear collisions". *Ann. Rev. Nucl. Part. Sci.* 55 2005, pp. 271–310. DOI: 10.1146/annurev.nucl.55.090704.151526. arXiv: nucl-ex/0502005.

[176] H. O. M. Trebien. "Fotoprodução exclusiva de quarkônios pesados em colisões ultra-periféricas". Dissertação de Mestrado. UFSC, 2020.

[177] S. Acharya et al. [ALICE]. "First measurement of the $|t|$-dependence of coherent J/ψ photonuclear production". *Phys. Lett. B* 817 2021, p. 136280. DOI: 10.1016/j.physletb.2021.136280. arXiv: 2101.04623 [nucl-ex].

[178] J. Adam et al. [ALICE]. "Coherent ρ^0 photoproduction in ultra-peripheral Pb-Pb collisions at $\sqrt{s_{\mathrm{NN}}} = 2.76$ TeV". *JHEP* 09 2015, p. 095. DOI: 10.1007/JHEP09(2015)095. arXiv: 1503.09177 [nucl-ex].

[179] S. Acharya et al. [ALICE]. "Coherent photoproduction of ρ^0 vector mesons in ultra-peripheral Pb-Pb collisions at $\sqrt{\mathrm{s_{NN}}} = 5.02$ TeV". *JHEP* 06 2020, p. 035. DOI: 10.1007/JHEP06(2020)035. arXiv: 2002.10897 [nucl-ex].

[180] S. Acharya et al. [ALICE]. "First measurement of coherent ρ0 photoproduction in ultra-peripheral Xe–Xe collisions at sNN=5.44 TeV". *Phys. Lett. B* 820 2021, p. 136481. DOI: 10.1016/j.physletb.2021.136481. arXiv: 2101.02581 [nucl-ex].

[181] H. Mäntysaari, F. Salazar, and B. Schenke. "Nuclear geometry at high energy from exclusive vector meson production". *Phys. Rev. D* 106.7 2022, p. 074019. DOI: 10.1103/PhysRevD.106.074019. arXiv: 2207.03712 [hep-ph].

[182] G. Antchev et al. [TOTEM]. "Proton-proton elastic scattering at the LHC energy of s** (1/2) = 7-TeV". *EPL* 95.4 2011, p. 41001. DOI: 10.1209/0295-5075/95/41001. arXiv: 1110.1385 [hep-ex].

[183] G. Aad et al. [ATLAS]. "Measurement of the total cross section from elastic scattering in pp collisions at $\sqrt{s} = 7$ TeV with the ATLAS detector". *Nucl. Phys. B* 889 2014, pp. 486–548. DOI: 10.1016/j.nuclphysb.2014.10.019. arXiv: 1408.5778 [hep-ex].

[184] J. L. Albacete and A. Soto-Ontoso. "Hot spots and the hollowness of proton–proton interactions at high energies". *Phys. Lett. B* 770 2017, pp. 149–153. DOI: 10.1016/j.physletb.2017.04.055. arXiv: 1605.09176 [hep-ph].

[185] S. D. Campos and V. A. Okorokov. "Hollowness effect and entropy in high energy elastic scattering". *Phys. Scripta* 95.9 2020, p. 095305. DOI: 10.1088/1402-4896/abaf8d. arXiv: 1807.02061 [hep-ph].

[186] W. Broniowski and E. Ruiz Arriola. "Hollowness in pp scattering". *Acta Phys. Polon. B* 48 2017, p. 927. DOI: 10.5506/APhysPolB.48.927. arXiv: 1704.03271 [hep-ph].

[187] V. A. Petrov and A. P. Samokhin. "Is There a Hollow Inside the Proton?" *Int. J. Mod. Phys. Conf. Ser.* 47 2018, p. 1860097. DOI: 10.1142/S2010194518600972. arXiv: 1801.03809 [hep-ph].

[188] V. M. Abazov et al. [TOTEM, D0]. "Odderon Exchange from Elastic Scattering Differences between pp and $p\bar{p}$ Data at 1.96 TeV and from pp Forward Scattering Measurements". *Phys. Rev. Lett.* 127.6 2021, p. 062003. DOI: 10.1103/PhysRevLett.127.062003. arXiv: 2012.03981 [hep-ex].

[189] S. Martins. "Fotoprodução de Mésons Vetoriais Pesados em Colisões Ultraperiferais e Periferais". PhD thesis. UFRGS, 2018.

[190] R. Glauber et al. *Lectures in theoretical physics*. Vol. 1. United States of America: Interscience, New York London, 1959, pp. 315–413.

[191] R. J. Glauber and G. Matthiae. "High-energy scattering of protons by nuclei". *Nucl. Phys. B* 21 1970, pp. 135–157. DOI: 10.1016/0550-3213(70)90511-0.

APPENDIX A – SUMMARY OF EMPLOYED MODELS

Model	**Explanation**	**References**
Photon flux	The Weizsäcker-Williams method consists of relating the electromagnetic fields produced by a charged particle moving with ultrarelativistic velocity with a flux of virtual photons. It is important in nuclear UPCs because it describes the origin of the photons that participate in the photon-nucleus collisions.	[173, 174]
Photon wave function	Part of the scattering amplitude that carries the information about the photon fluctuation into the $q\bar{q}$ pair.	[42, 73, 74, 75, 76, 77, 78]
Color dipole parameterization	Part of the scattering amplitude that describes the interaction of the $q\bar{q}$ pair with the target nucleon.	GBW [46, 47, 48], KST [49], bSat [52], BK [63], bCGC [65, 2, 3, 67]
Real part	Term that considers the contribution of the real part of the scattering amplitude.	[42]
Skewness	Correction that takes into account the fact that the gluons exchanged between the $q\bar{q}$ pair and the target nucleon can carry different momentum fractions.	[45]
Vector meson wave function	Part of the scattering amplitude that carries the information about the combination of the $q\bar{q}$ pair into the vector meson. For heavy vector mesons, a non-relativistic Schrödinger equation is solved in the $q\bar{q}$ rest frame with different interquark potentials to obtain the vector meson wave functions for ψ and Υ. For light vector mesons, the Brodsky-de Téramond approach (based on the AdS/QCD correspondence) can be used to obtain the vector meson wave functions for ρ, ω, and ϕ.	Potential approach [4, 42], AdS/QCD holographic model [12, 126]
Melosh spin rotation	Transformation that is responsible for the spin boost. It is necessary for heavy vector mesons.	[100, 101]
Coherent production	Vector meson production through the process $\gamma A \to VA$, which maintains the nucleus target intact.	[158, 38]
Incoherent production	Vector meson production through the process $\gamma A \to VA^*$ whose nucleus does not remain intact after the collision	[165, 166, 167]
Glauber–Gribov model	Model used to calculate the dipole-nucleus scattering amplitude by the summation of all possible successive rescatterings with the nucleons inside the nucleus.	[159, 160, 161]

Nuclear profile	The Woods-Saxon considers a homogeneous distribution of the nucleons inside the nucleus.	[163]
Gluon shadowing	Effect that reduces the nuclear cross section and is related to the presence of higher states with gluon inclusions that survive a shorter time than the $\|q\bar{q}\rangle$ state.	[32, 168, 169, 171]
Finite coherence length	Effect related to the finiteness lifetime of the quark-antiquark pair. It is relevant when the coherence length is smaller than the nucleus radius $l_c \lesssim R_A$.	[168]

APPENDIX B – WEIZSÄCKER-WILLIAMS METHOD FOR THE PHOTON FLUX

To calculate the flux factor of a charged particle moving in the x_1 direction with a constant velocity v relative to the inertial reference frame S, one will first write the relationship between the electromagnetic fields in the particle rest frame S' and the frame S.

$$\begin{aligned} E_1 &= E'_1 & B_1 &= B'_1 \\ E_2 &= \gamma(E'_2 + \beta B'_3) & B_2 &= \gamma(B'_2 - \beta E'_3) \\ E_3 &= \gamma(E'_3 - \beta B'_2) & B_3 &= \gamma(B'_3 + \beta E'_2) \end{aligned} \tag{128}$$

Figure 41 – Relation between the reference frame S' (where the punctual charge q is at rest) and S (where the charge moves with velocity v in the x_1 direction)

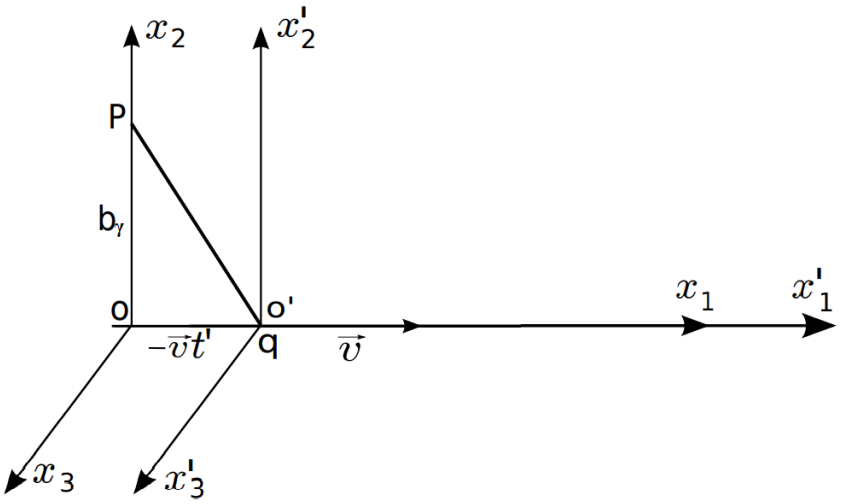

Source: Figure adapted from [189].

Considering the existence of an observer at a point P with coordinates $r' = (-vt', b, 0)$ in S' (Fig. 41), it is possible to see that only the fields

$$E'_1 = \frac{-qvt'}{r'^3} \qquad E'_2 = \frac{qb_\gamma}{r'^3} \tag{129}$$

are non-zero. However, by performing a Lorentz transformation on these fields, one finds that the intensity of the electromagnetic field generated by a charged particle as measured in P is given by:

$$E_1 = \frac{-q\gamma vt}{\left(b_\gamma^2 + (\gamma vt)^2\right)^{3/2}} \qquad E_2 = \frac{q\gamma b_\gamma}{\left(b_\gamma^2 + (\gamma vt)^2\right)^{3/2}} \qquad B_3 = \beta E_2. \tag{130}$$

In the limit of relativistic velocities, where $\beta \sim 1$, the magnetic field B_3 tends to the same value as E_2, creating a symmetry between these two fields that is characteristic of electromagnetic waves. This means that in reference frame S, these two fields behave like a radiation pulse

P_1 propagating in the direction of the charged particle (Fig. 42). However, it does not exist a magnetic field in S that can be associated with E_1 to form another pulse. To resolve this impasse, it is worth noting that if the charge does not exhibit relativistic motion in S, it is possible to introduce a magnetic field without affecting the physics of the problem, as in this reference frame, particles only respond to the electric field. Consequently, a second pulse P_2 propagating in the x_2 direction can be formed (Fig. 42).

Figure 42 – Equivalent radiation pulses P_1 and P_2 as saw by an observer at a point P in the rest frame S.

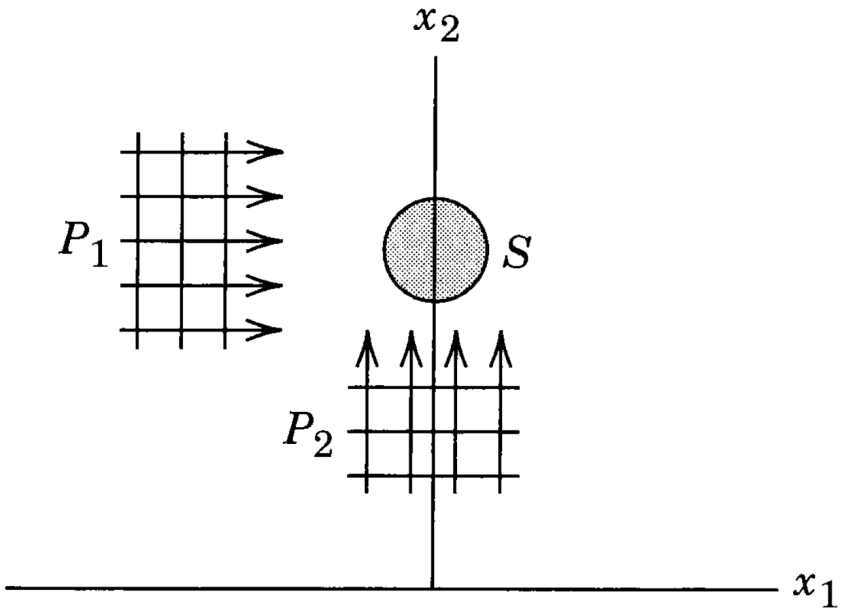

Source: Figure taken from [174].

After an analysis of the system, it is possible to establish a relationship between each of the pulses and a frequency spectrum [174]

$$\frac{\mathrm{d}^3 I(\omega, b_\gamma)}{\mathrm{d}\omega \mathrm{d}^2 b_\gamma} = \frac{c}{2\pi}|E(\omega)|^2, \tag{131}$$

where $E(\omega)$ is the Fourier transform of the time-dependent electric field. This quantity can be obtained by eq. 130, and the calculation of E_2 is shown below:

$$E_2(\omega) = \frac{1}{\sqrt{2\pi}} \int_{-\infty}^{\infty} \frac{q\gamma b_\gamma}{\left(b_\gamma^2 + (\gamma v t)^2\right)^{3/2}} e^{i\omega t} \mathrm{d}t = \frac{1}{\sqrt{2\pi}} \frac{q}{bv} \int_{-\infty}^{\infty} \frac{e^{i\alpha\zeta}}{\left(1+\zeta^2\right)^{3/2}} \mathrm{d}\zeta, \tag{132}$$

where $\zeta = \frac{\gamma v t}{b_\gamma}$ and $\alpha = \frac{\omega b}{\gamma v}$.

For a moment, let's just focus on the integral presented in the previous equation,

$$\begin{aligned} I &= \int_{-\infty}^{\infty} \frac{e^{i\alpha\zeta}}{\left(1+\zeta^2\right)^{3/2}} \mathrm{d}\zeta \\ &= \int_{-\infty}^{\infty} \frac{\cos(\alpha\zeta)}{\left(1+\zeta^2\right)^{3/2}} \mathrm{d}\zeta + i \int_{-\infty}^{\infty} \frac{\sin(\alpha\zeta)}{\left(1+\zeta^2\right)^{3/2}} \mathrm{d}\zeta \\ &= 2 \int_{0}^{\infty} \frac{\cos(\alpha\zeta)}{\left(1+\zeta^2\right)^{3/2}} \mathrm{d}\zeta \,. \end{aligned} \tag{133}$$

The derivation of the last line comes from the fact that the integrand of the first term is even, while the integrand of the second term is odd (which makes the integral identically zero). This final result can be expressed more elegantly in terms of the Bessel function. To do so, we employ the following property:

$$K_\nu(xz) = \frac{\Gamma\left(\nu+\frac{1}{2}\right)(2z)^\nu}{\pi^{1/2}x^\nu} \int_0^\infty \frac{\cos(xt)}{\left(t^2+z^2\right)^{\nu+1/2}} \mathrm{d}t, \tag{134}$$

taking $\nu = 1$ and $z = 1$

$$K_1(x) = \frac{1}{x} \int_0^\infty \frac{\cos(xt)}{\left(t^2+1\right)^{3/2}} \mathrm{d}t. \tag{135}$$

Replacing this result in 132, one finds the final expression for the electric field E_2:

$$E_2(\omega) = \frac{1}{\sqrt{2\pi}} \frac{q}{bv} 2\alpha K_1(\alpha). \tag{136}$$

The calculation of the electric field E_1 can be done by simply following the same steps as shown earlier. However, in this case, the integral obtained will be slightly different from 133, and an additional algebraic manipulation will be required.

$$E_1(\omega) = \frac{1}{\sqrt{2\pi}} \int_{-\infty}^{\infty} \frac{-q\gamma v t}{\left(b_\gamma^2 + (\gamma v t)^2\right)^{3/2}} e^{i\omega t} \mathrm{d}t = -\frac{1}{\sqrt{2\pi}} \frac{q}{b_\gamma \gamma v} \int_{-\infty}^{\infty} \frac{\zeta e^{i\alpha\zeta}}{\left(1+\zeta^2\right)^{3/2}} \mathrm{d}\zeta. \tag{137}$$

This time, the integral to be calculated is:

$$\begin{aligned} I' &= \int_{-\infty}^{\infty} \frac{\zeta e^{i\alpha\zeta}}{\left(1+\zeta^2\right)^{3/2}} \mathrm{d}\zeta \\ &= i \int_{-\infty}^{\infty} \frac{\zeta \sin(\alpha\zeta)}{\left(1+\zeta^2\right)^{3/2}} \mathrm{d}\zeta \\ &= 2i \int_{0}^{\infty} \frac{\alpha \cos(\alpha\zeta)}{\left(1+\zeta^2\right)^{3/2}} \mathrm{d}\zeta, \end{aligned} \tag{138}$$

in which the function parity was used again to eliminate the term proportional to $\cos(\alpha\zeta)$ in the second line. Additionally, integration by parts was performed to obtain the expression in

the third line. After this procedure, it is possible to use the property 134 with $\nu = 0$ and $z = 1$ to substitute this integral in 137, and thus, find:

$$E_1(\omega) = -\frac{1}{\sqrt{2\pi}} \frac{q}{b_\gamma \gamma v} 2i\alpha K_0(\alpha). \tag{139}$$

Once the expressions for the electric fields are obtained as a function of the frequency, they can be summed and substituted into 131, resulting in the total frequency spectrum experienced at point P:

$$\frac{\mathrm{d}^3 I(\omega, b_\gamma)}{\mathrm{d}\omega \mathrm{d}^2 b} = \frac{c\, q^2}{v^2 \pi^2} \frac{\alpha^2}{b_\gamma^2} \left(K_1^2(\alpha) + \frac{K_0^2(\alpha)}{\gamma^2} \right). \tag{140}$$

It is worth noting that we are interested in the high-energy limit, so it is convenient to approximate $v \sim c$ and introduce a quantity called the flux of equivalent photons per unit area and frequency

$$\frac{\mathrm{d}^3 N(\omega, b_\gamma)}{\mathrm{d}\omega \mathrm{d}^2 b} = \frac{1}{\omega} \frac{\mathrm{d}^3 I(\omega, b_\gamma)}{\mathrm{d}\omega \mathrm{d}^2 b} = \frac{q^2}{\pi^2} \frac{\alpha^2}{b_\gamma^2} \left(K_1^2(\alpha) + \frac{K_0^2(\alpha)}{\gamma^2} \right), \tag{141}$$

where $\alpha = \frac{\omega b_\gamma}{\gamma}$.

APPENDIX C – DERIVATIVE ANALICITY RELATIONS

Dispersion relations are an effective tool to obtain an expression of the real part of an amplitude in terms of its imaginary part. Following the derivation presented in [43, 44] for pp scatterings, one starts with the subtracted dispersion relation [43] for an even amplitude f_+ in terms of the center-of-mass energy squared s:

$$\mathrm{Re}\, f_+(s,t) = \frac{2s^2}{\pi} P \int_{s_0}^{\infty} \frac{ds'}{s'\left(s^2 - s^2\right)} \mathrm{Im}\, f_+\left(s',t\right) , \tag{142}$$

where P represents the Cauchy's principal value (which appears because of the explicit divergence).

To solve this problem, let's first concentrate on the evaluation of the integral:

$$I = P \int_{s_0}^{\infty} \frac{ds'}{s'\left(s^2 - s^2\right)} \mathrm{Im}\, f_+\left(s',t\right) . \tag{143}$$

It can be solved by multiplying the r.h.s by $\frac{s^\alpha}{s^\alpha}$ (α is a real parameter) and integrating by parts with:

$$u = \frac{\mathrm{Im}\, f_+\left(s',t\right)}{s'} \frac{s'}{s'} , \qquad v' = \frac{1}{s'^2 - s^2}$$

Thus,

$$I = \frac{\mathrm{Im}\, f_+\left(s',t\right)}{s'\, 2s} \ln\left|\frac{s-s'}{s+s'}\right|\Bigg|_{s_0}^{\infty} - \int_{s_0}^{\infty} ds' \frac{1}{2s} \ln\left|\frac{s-s'}{s+s'}\right| \frac{d}{ds'}\left(\frac{\mathrm{Im}\, f_+\left(s',t\right)}{s'^\alpha} s'^{\alpha-1}\right) . \tag{144}$$

In the high energy limit ($s >> s_0$), the first term vanishes, remaining only:

$$I = -\frac{1}{2s} \int_{s_0}^{\infty} ds' \ln\left|\frac{s-s'}{s+s'}\right| s'^{\alpha-1} \left[\frac{\alpha-1}{s'} + \frac{d}{ds'}\right] \frac{\mathrm{Im}\, f_+\left(s',t\right)}{s'^\alpha} . \tag{145}$$

Now, one can perform a change of variable $s = e^\xi$ and $s' = e^{\xi'}$ and use the relation:

$$\ln\left(\frac{e^\xi + e^{\xi'}}{e^\xi - e^{\xi'}}\right) = \ln\left(\frac{\xi' - \xi}{2}\right) \tag{146}$$

to rewrite Eq. 145 as:

$$I = -\frac{1}{2s} \int_{\ln s_0}^{\infty} d\xi' e^{\xi'(\alpha-1)} \ln\left(\coth\left|\frac{\xi-\xi'}{2}\right|\right) \left[\alpha - 1 + \frac{d}{d\xi'}\right] \frac{\mathrm{Im}\, f_+\left(e^{\xi'},t\right)}{e^{\xi'\alpha}} . \tag{147}$$

Now, one can expand $\frac{\mathrm{Im}\, f_+(s',t)}{s'^\alpha}$ in powers of $(\xi' - \xi)$:

$$\frac{\mathrm{Im}\, f_+\left(s',t\right)}{s'^\alpha} = \sum_{n=0}^{\infty} \frac{1}{n!} \left(\frac{d^{(n)}}{d \ln s'^{(n)}} \frac{\mathrm{Im}\, f_+\left(s',t\right)}{s'^\alpha}\right)\Bigg|_{\xi'=\xi} (\xi' - \xi)^n , \tag{148}$$

and change the order of the integration and the summation. Since the calculations are evaluated in the high energy region ($s >> s_0$), one can take the limit of $s_0 \to 0 \Rightarrow \ln s_0 \to -\infty$, which leads to the expression:

$$I = \frac{s^{\alpha-2}}{2} \sum_{n=0}^{\infty} \frac{1}{n!} \left(\frac{d^{(n)}}{d \ln s^{(n)}} \frac{\mathrm{Im}\, f_+\left(s,t\right)}{s^\alpha}\right) I_n \tag{149}$$

with

$$I_n = \int_{-\infty}^{\infty} d\xi' e^{(\xi'-\xi)(\alpha-1)} \ln\left(\coth\left|\frac{\xi-\xi'}{2}\right|\right)\left[\alpha - 1 + \frac{d}{d\xi'}\right](\xi'-\xi)^n \tag{150}$$

Let's consider that the series can be integrated term by term. Therefore, using $y \equiv \xi' - \xi$, one can evaluate the integral I_n (Eq. 150) by integrating by parts:

$$u = \ln\left(\coth\left|\frac{y}{2}\right|\right) \Rightarrow u' = -\frac{1}{\sinh y} \quad \text{and} \quad v' = e^{(\alpha-1)y}\left[\alpha - 1 + \frac{d}{dy}\right] y^n \Rightarrow v = e^{(\alpha-1)y} y^n$$

leads to

$$I_n = \ln\left(\coth\left|\frac{y}{2}\right|\right) e^{(\alpha-1)y} y^n \Big|_{-\infty}^{\infty} + \int_{-\infty}^{\infty} dy \frac{e^{(\alpha-1)y} y^n}{\sinh y}\,. \tag{151}$$

An important point to highlight is that the first term on the r.h.s approaches zero only when $0 < \alpha < 2$, since $\ln\left(\coth\left|\frac{y}{2}\right|\right)$ decreases like $2e^{-|y|}$ for large values of y. Consequently, just the second term is relevant for I_n, and it can be expressed as a recursive relation in terms of α:

$$\begin{aligned} \frac{dI_n}{d\alpha} &= \int_{-\infty}^{\infty} dy \frac{e^{(\alpha-1)y} y^{n+1}}{\sinh y} = I_{n+1} \\ \frac{dI_{n+1}}{d\alpha} &= \int_{-\infty}^{\infty} dy \frac{e^{(\alpha-1)y} y^{n+2}}{\sinh y} = I_{n+2} \end{aligned} \tag{152}$$

Thus, $I_{n+2} = \frac{d^2 I_n}{d\alpha^2}$ and for the n^{th} term $I_n = \frac{d^n I_0}{d\alpha^n}$, with I_0 being integrated in the complex plane:

$$I_0 = \int_{-\infty}^{\infty} dy \frac{e^{(\alpha-1)y}}{\sinh y} = \pi \tan\left[\frac{\pi}{2}(\alpha-1)\right]\,. \tag{153}$$

Substituting this result (Eq. 153) into Eq. 149, one obtains:

$$I = \frac{s^{\alpha-2}\pi}{2} \sum_{n=0}^{\infty} \frac{1}{n!} \left(\frac{d^{(n)}}{d\ln s^{(n)}} \frac{\operatorname{Im} f_+(s,t)}{s^\alpha}\right) \frac{d^n}{d\alpha^n} \tan\left[\frac{\pi}{2}(\alpha-1)\right]\,. \tag{154}$$

Then, one can replace this equation into the expression for the real part of the even amplitude (Eq. 142) and write the first terms of the series:

$$\operatorname{Re} f_+(s,t) = s^\alpha \frac{\operatorname{Im} f_+(s,t)}{s^\alpha} \tan\left[\frac{\pi}{2}(\alpha-1)\right] + s^\alpha \left(\frac{d}{d\ln s} \frac{\operatorname{Im} f_+(s,t)}{s^\alpha}\right) \sec^2\left[\frac{\pi}{2}(\alpha-1)\right] \frac{\pi}{2} + \cdots \tag{155}$$

which correspond exactly to the first terms of the Taylor expansion of the function

$$\operatorname{Re} f_+(s,t) = \frac{s^\alpha}{\pi} \tan\left[\frac{\pi}{2}\left(\alpha - 1 + \frac{d}{d\ln s}\right)\right] \frac{\operatorname{Im}\ f_+(s,t)}{s^\alpha}\,. \tag{156}$$

According to [43], the choice of the α value is not very relevant, since the results do not depend strongly on this parameter. A standard choice is to put $\alpha = 1$ [44], which is also appropriate for hadronic scatterings with a pomeron exchange [43]. Thus, following this conventional choice,

the first term in Eq. 155 vanishes, remaining only the second term (along with higher-order terms, which will not be considered in this analysis)

$$\mathrm{Re}\, f_+(s,t) = \frac{\pi s}{2}\left(\frac{d}{d\ln s}\frac{\mathrm{Im}\, f_+(s,t)}{s}\right) \tag{157}$$

The main purpose of these calculations is to find an expression for the ratio of the real to imaginary parts of the forward elastic scattering amplitude

$$\rho(s) = \frac{\mathrm{Re}\,\mathcal{A}(s,t=0)}{\mathrm{Im}\,\mathcal{A}(s,t=0)}\,, \tag{158}$$

which is related to the even amplitude by:

$$\mathcal{A}(s,t=0) \equiv \frac{f_+(s,t=0)}{s}\,. \tag{159}$$

Therefore, substituting Eq. 157 into Eq. 159, one obtains the real part of the forward elastic scattering amplitude

$$\mathrm{Re}\,\mathcal{A}(s,0) = \frac{\pi}{2}\left(\frac{d}{d\ln s}\frac{\mathrm{Im}\,\mathcal{A}(s,0)}{s}\right)\,, \tag{160}$$

and, consequently, replacing it on the expression of the ratio (Eq. 158), one finally gets the derivative analyticity relation (DAR):

$$\rho(s) = \frac{\pi}{2}\frac{d\ln\mathcal{A}(s)}{d\ln s}\,. \tag{161}$$

APPENDIX D – LIGHT-FRONT COORDINATES AND KINEMATICS

In the ordinary four-dimension Minkowski space-time, an event is defined by a time coordinate (x^0) and three space coordinates (x^1, x^2, x^3). In this space, any four-vector can be written as $A^\mu = (A^0, A^1, A^2, A^3) = (A^0, \boldsymbol{A})$ and the Minkowski metric is given by :

$$g^{\mu\nu} = g_{\mu\nu} = \text{diag}(+1, -1 - 1 - 1)\,. \tag{162}$$

The light-front coordinates are defined as:

$$A^\pm = \left(A^0 \pm A^3\right)\,, \tag{163}$$

which enables a four-vector to be expressed as $A^\mu = (A^+, A^-, \boldsymbol{A_T})$, where $\boldsymbol{A_T}$ is the transverse component of the vector (A^1, A^2). The four-vector squared can be written as:

$$A^2 = \left(A^0\right)^2 - (\boldsymbol{A})^2 = A^+A^- - (\boldsymbol{A_T})^2\,. \tag{164}$$

One can use these relations to write the shell relation $P^2 = M^2$ as $P^2 = P^+P^- - (\boldsymbol{P_T})^2$, which leads to the dispersion relation for the minus component of the light-front momentum:

$$P^- = \frac{\boldsymbol{P_T^2} + M^2}{P^+}\,. \tag{165}$$

APPENDIX E – COLOR DIPOLE KINEMATICS

Considering a photon with four-momentum $q = (q^+, q^-, \boldsymbol{q_T})$, one can define the plus component of the quark and antiquark momentum, respectively, as:

$$\begin{aligned} k^+ &= \beta q^+ \\ k'^+ &= (1-\beta) q^+ \,, \end{aligned} \tag{166}$$

where β is a parameter that varies from 0 to 1. Hence, regarding that these two particles are on-shell,

$$\begin{aligned} k^2 &= m_q^2 \\ k'^2 &= m_{\bar{q}}^2 \,, \end{aligned} \tag{167}$$

one can use Eq. 165 (Appendix D) to write the quark and antiquark four-momentum as:

$$\begin{aligned} k &= \left(\beta q^+, \frac{m_T^2}{\beta q^+}, \boldsymbol{p_T} \right) \\ k' &= \left((1-\beta) q^+, \frac{m_T^2}{(1-\beta) q^+}, -\boldsymbol{p_T} \right) \,, \end{aligned} \tag{168}$$

with $m_T^2 = m_q^2 + p_T^2$.

The square of the sum of these two four-momenta gives the squared invariant mass in the $q\bar{q}$-pair infinite momentum frame:

$$\begin{aligned} M_{Q\bar{Q}}^2 &= \left[k + k' \right]^2 \\ &= \left[\left(q^+, \frac{m_T^2}{\beta(1-\beta) q^+}, \mathbf{0} \right) \right]^2 \\ &= \frac{m_T^2}{\beta(1-\beta)} \,. \end{aligned} \tag{169}$$

In the $q\bar{q}$ rest frame, the pair tri-momentum vanishes $\boldsymbol{P_{Q\bar{Q}}} = 0$, thus the squared invariant mass is exactly the dipole energy squared:

$$M_{Q\bar{Q}}^2 = P_{Q\bar{Q}}^{\mu} P_{Q\bar{Q}\,\mu} = E_{Q\bar{Q}}^2 - \cancelto{0}{\boldsymbol{P_{Q\bar{Q}}} \cdot \boldsymbol{P_{Q\bar{Q}}}} \,. \tag{170}$$

Besides that, in this frame, the pair energy is just the sum of the energy of the constituents:

$$\begin{aligned} E_{Q\bar{Q}} &= E_q + E_{\bar{q}} = 2E_q \\ E_{Q\bar{Q}}^2 &= 4E_q^2 \,. \end{aligned} \tag{171}$$

Finally, substituting it in Eq. 170 and using the dispersion relation, one obtains the squared invariant mass in the $q\bar{q}$ rest frame:

$$M_{Q\bar{Q}}^2 = 4(p^2 + m_q^2) \,. \tag{172}$$

APPENDIX F – KINEMATICS OF A TWO-BODY ELASTIC SCATTERING

Figure 43 – Schematic representation of the kinematic variables in a two-body scattering in the CMS frame.

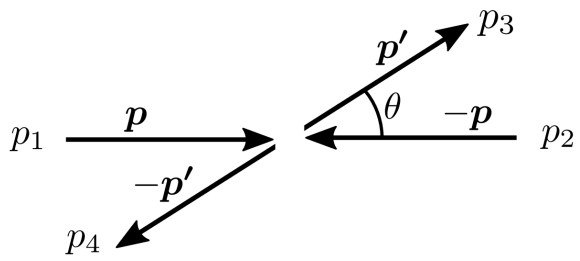

Source: Figure taken from [189].

This appendix will present the kinematics of a generic two-body elastic scattering (Fig. 43)

$$1 + 2 \to 3 + 4 \tag{173}$$

in the center-of-mass system (CMS) frame [33, 189]. This means that the three-momentum of the incident particles is related as:

$$\boldsymbol{p_1} + \boldsymbol{p_2} = 0 \tag{174}$$

Assuming that the initial particles only move in the longitudinal direction z, the four-momentum of each one of these particles is given by:

$$\begin{aligned} p_1 &= (E_1, \boldsymbol{p}) = (E_1, 0, 0, p_z) \\ p_2 &= (E_2, -\boldsymbol{p}) = (E_2, 0, 0, -p_z) \\ p_3 &= (E_3, \boldsymbol{p'}) = (E_3, \boldsymbol{p_T}, p'_z) \\ p_4 &= (E_4, -\boldsymbol{p'}) = (E_4, -\boldsymbol{p_T}, -p'_z)\,, \end{aligned} \tag{175}$$

where the final particles were allowed to have transverse momentum $\boldsymbol{p_T}$.

The number of independent variables in a $(1 + 2 \to 3 + 4)$ problem is two, thus one can choose as independent variables the absolute value of the initial state particles $|\boldsymbol{p}| = p_z$ (this equality comes from the fact that particles 1 and 2 move only in the z-direction) and the scattering angle θ. Hence, with respect to the variables in Eq. 175, they can be written as:

$$\begin{aligned} p'_z &= |p'| \cos\theta \\ |\boldsymbol{p_T}| &= |p'| \sin\theta\,. \end{aligned} \tag{176}$$

The energies in Eq. 175 can be written in terms of the CM energy squared $s = (p_1 + p_2)^2$, or

$$\sqrt{s} = E_1 + E_2\,. \tag{177}$$

To find the energy of the particle 2 (E_2) in terms of the energy of the particle 1 (E_1), one can use the on-shell relation $E_{1,2}^2 = m_{1,2}^2 + p_z^2$ combined with the fact that both particles have the same p_z^2. This leads to the following expression:

$$\begin{aligned} E_1^2 - m_1^2 &= E_2^2 - m_2^2 \\ E_2 &= \sqrt{E_1^2 - m_1^2 - m_2^2}\,, \end{aligned} \tag{178}$$

which when substituted in Eq. 177, leads to

$$\begin{aligned} \sqrt{s} &= E_1 + \sqrt{E_1^2 - m_1^2 - m_2^2} \\ \sqrt{s} - E_1 &= \sqrt{E_1^2 - m_1^2 - m_2^2} \\ s - 2\sqrt{s}E_1 + E_1^2 &= E_1^2 - m_1^2 - m_2^2 \\ E_1 &= \frac{s + m_1^2 + m_2^2}{2\sqrt{s}}\,. \end{aligned} \tag{179}$$

The same procedure can be done for the other energies, giving:

$$\begin{aligned} E_2 &= \frac{1}{2\sqrt{s}}\left[s + m_2^2 - m_1^2\right] \\ E_3 &= \frac{1}{2\sqrt{s}}\left[s + m_3^2 - m_4^2\right] \\ E_4 &= \frac{1}{2\sqrt{s}}\left[s + m_4^2 - m_3^2\right]\,. \end{aligned} \tag{180}$$

Now, one can use again the on-shell relation together with Eq. 179 to calculate the momentum $\boldsymbol{p^2}$ in terms of s:

$$\begin{aligned} \boldsymbol{p}^2 &= E_1^2 - m_1^2 \\ &= \frac{s + m_1^2 - m_2^2}{4s} - m_1^2 \\ &= \frac{\left[s + (m_1 + m_2)\,(m_1 - m_2)\right]^2 - 4sm_1^2}{4s} \\ &= \frac{s^2 + 2s\,(m_1 + m_2)\,(m_1 - m_2) + (m_1 + m_2)^2\,(m_1 - m_2)^2 - 4sm_1^2}{4s} \\ &= \frac{s^2 - s\,(m_1 - m_2)^2 - s\,(m_1 + m_2)^2 + (m_1 + m_2)^2\,(m_1 - m_2)^2}{4s} \\ &= \frac{\left[s - (m_1 + m_2)^2\right]\left[s - (m_1 - m_2)^2\right]}{4s} \\ &= \frac{1}{4s}\lambda\left(s, m_1^2, m_2^2\right)\,, \end{aligned} \tag{181}$$

where $\lambda(x, y, z) = x^2 + y^2 + z^2 - 2xy - 2yz - 2xz$. Analogously, the momentum $\boldsymbol{p'}$ is given by:

$$\begin{aligned} \boldsymbol{p'}^2 = \boldsymbol{p}_T^2 + p_z^2 &= E_3^2 - m_3^2 \\ &= \frac{\left[s - (m_3 + m_4)^2\right]\left[s - (m_3 - m_4)^2\right]}{4s} \\ &= \frac{1}{4s}\lambda\left(s, m_3^2, m_4^2\right)\,. \end{aligned} \tag{182}$$

Finally, taking the limit $s \to 0$ in the previous equations, one finds the high energy limit of the energies and the momenta:

$$\begin{aligned} E_1, E_2, E_3, E_4 &\underset{s\to\infty}{\simeq} \frac{\sqrt{s}}{2} \\ |\boldsymbol{p}|, |\boldsymbol{p}'| &\underset{s\to\infty}{\simeq} \frac{\sqrt{s}}{2}\,. \end{aligned} \tag{183}$$

APPENDIX G – GLAUBER MODEL

In the original work [190, 191], Glauber used the diffraction approximation to write the proton-nucleon scattering amplitude as:

$$f_j\left(\boldsymbol{k}-\boldsymbol{k}'\right)=\frac{ik}{2\pi}\int e^{i(\boldsymbol{k}-\boldsymbol{k}')\cdot\boldsymbol{b}}\Gamma_j(\boldsymbol{b})d^2b. \tag{184}$$

In this equation, f is the Fourier transform of the profile function $\Gamma(\boldsymbol{b})$, which may be expressed in terms of the phase-shift function $\chi(b)$

$$\Gamma(\boldsymbol{b})=1-e^{i\chi(\boldsymbol{b})} \tag{185}$$

For the case of proton-nucleus collision, the corresponding scattering amplitude is given by:

$$F_{\mathrm{fi}}(\Delta)=\frac{ik}{2\pi}\int \mathrm{e}^{i\Delta\cdot\boldsymbol{b}}\psi_{\mathrm{f}}^{*}\left(\{\boldsymbol{r}_j\}\right)\Gamma\left(\boldsymbol{b},s_1\ldots s_A\right)\psi_{\mathrm{i}}\left(\{\boldsymbol{r}_j\}\right)\prod_{j=1}^{A}\mathrm{d}^3r_j\;\mathrm{d}^2b\,, \tag{186}$$

where ψ_{i} and ψ_{f} are, respectively, the initial and final state wave functions of the nucleus and $\boldsymbol{\Delta}=\boldsymbol{k}-\boldsymbol{k}'$. The position of a nucleon j that compounds the nucleus is denoted by $\boldsymbol{r_j}$, $j=1,\ldots,A$, and its projection into the perpendicular plane (where lies the impact parameter vector $\boldsymbol{b}$) is $\boldsymbol{s_j}$

In the diffraction approximation, it is assumed that the overall phase-shift function $\chi(\boldsymbol{b},\boldsymbol{s_1},\ldots,\boldsymbol{s_A})$ is the sum of phase-shift functions of the individual nucleon collision $\chi_j(\boldsymbol{b},\boldsymbol{s_j})$. Thus, one can write the nuclear profile function as:

$$\Gamma\left(\boldsymbol{b},\boldsymbol{s_1},\ldots,\boldsymbol{s_A}\right)\equiv 1-\mathrm{e}^{i\chi(\boldsymbol{b},\boldsymbol{s_1},\ldots,\boldsymbol{s_A})}=1-\mathrm{e}^{i\sum_{j=1}^{A}\chi_j(\boldsymbol{b}-\boldsymbol{s}_j)}=1-\prod_{j=1}^{A}\left[1-\Gamma_j\left(\boldsymbol{b}-\boldsymbol{s_j}\right)\right]. \tag{187}$$

For the nucleus ground state wave function, the independent particle model will be assumed, which basically neglects the existence of correlations between the position of the nucleons. This enables one to write the nuclear wave function as the product of the individual nucleon wave functions. Thus introducing the single particle densities $\rho_j(\boldsymbol{r_j})$, one finds:

$$\left|\psi_{\mathrm{i}}\left(\boldsymbol{r}_1\ldots\boldsymbol{r}_A\right)\right|^2=\prod_{j=1}^{A}\rho_j\left(\boldsymbol{r}_j\right)\,, \tag{188}$$

which has the following normalization condition:

$$\int\rho_j\left(\boldsymbol{r_j}\right)\mathrm{d}^3r_j=1\,. \tag{189}$$

These approximations (Eqs. 187 and 188) can be used to calculate the amplitude for an elastic nuclear scattering, which is when the final state is the same as the initial one. Thus,

Eq. 186 will be transformed into:

$$\begin{aligned} F_{\mathrm{N}}(\Delta) &= \frac{ik}{2\pi}\int \mathrm{e}^{i\boldsymbol{\Delta}\cdot\boldsymbol{b}}\psi_{\mathrm{i}}^{*}\left(\{\boldsymbol{r}_j\}\right)\left\{1-\prod_{j=1}^{A}\left[1-\Gamma_j\left(\boldsymbol{b}-\boldsymbol{s}_{\boldsymbol{j}}\right)\right]\right\}\psi_{\mathrm{i}}\left(\{\boldsymbol{r}_j\}\right)\prod_{1}^{A}\,\mathrm{d}^3r_j\,\mathrm{d}^2b \\ &= \frac{ik}{2\pi}\int \mathrm{e}^{i\boldsymbol{\Delta}\cdot\boldsymbol{b}}\left\{\left|\psi_{\mathrm{i}}\left(\{\boldsymbol{r}_j\}\right)\right|^2-\left|\psi_{\mathrm{i}}\left(\{\boldsymbol{r}_j\}\right)\right|^2\prod_{j=1}^{A}\left[1-\Gamma_j\left(\boldsymbol{b}-\boldsymbol{s}_{\boldsymbol{j}}\right)\right]\right\}\prod_{1}^{A}\,\mathrm{d}^3r_j\,\mathrm{d}^2b \\ &= \frac{ik}{2\pi}\int \mathrm{e}^{i\boldsymbol{\Delta}\cdot\boldsymbol{b}}\left\{\int\prod_{j=1}^{A}\rho_j\left(\boldsymbol{r}_j\right)\,\mathrm{d}^3r_j-\int\prod_{j=1}^{A}\rho_j\left(\boldsymbol{r}_j\right)\left[1-\Gamma_j\left(\boldsymbol{b}-\boldsymbol{s}_{\boldsymbol{j}}\right)\right]\,\mathrm{d}^3r_j\right\}\,\mathrm{d}^2b \\ &= \frac{ik}{2\pi}\int \mathrm{e}^{i\boldsymbol{\Delta}\cdot\boldsymbol{b}}\left\{1-\prod_{j=1}^{A}\left[1-\int\rho_j\left(\boldsymbol{r}_{\boldsymbol{j}}\right)\Gamma_j\left(\boldsymbol{b}-\boldsymbol{s}_{\boldsymbol{j}}\right)\mathrm{d}^3r_j\right]\right\}\mathrm{d}^2b \end{aligned} \tag{190}$$

Following the original Glauber prescription [190], one will use the high-energy approximation and work with phase-shift functions. Thus, analyzing Eq. 190, one can see that it has a similar form as Eq. 184; hence it is convenient to define the second term of Eq. 190 in terms of an effective phase-shift function χ_{opt}:

$$e^{i\chi_{opt}(\boldsymbol{b})} = \int\left|\psi_{\mathrm{i}}\left(\{\boldsymbol{r}_j\}\right)\right|^2 e^{i\sum_{j=1}^{N}\chi_j(\boldsymbol{b}-\boldsymbol{s}_j)}\prod_{j=1}^{A}d^3r_j = \prod_{j=1}^{A}\left[1-\int\rho_j\left(\boldsymbol{r}_{\boldsymbol{j}}\right)\Gamma_j\left(\boldsymbol{b}-\boldsymbol{s}_{\boldsymbol{j}}\right)\mathrm{d}^3r_j\right], \tag{191}$$

which leads to the following:

$$\chi_{opt}(\boldsymbol{b}) = -i\sum_{j=1}^{A}\log\left[1-\int\rho_j\left(\boldsymbol{r}_{\boldsymbol{j}}\right)\Gamma_j\left(\boldsymbol{b}-\boldsymbol{s}_{\boldsymbol{j}}\right)\mathrm{d}^3r_j\right]. \tag{192}$$

It is good to remark that the logarithmic is a multi-valued function. Thus, in order to maintain the consistency of the theory, one chooses the branch which vanishes when $b\to\infty$.

Another simplification should be considered to evaluate the integration in Eq. 192. One should recall that the range of the interactions between the incident particles and the target nucleons should be smaller than the nuclear radius R. Consequently, when this interaction is strong, the profile functions Γ_j approach the unit, and when it is weak, they vanish. This implies that the term:

$$\int\rho_j\left(\boldsymbol{r}_{\boldsymbol{j}}\right)\Gamma_j\left(\boldsymbol{b}-\boldsymbol{s}_{\boldsymbol{j}}\right)\mathrm{d}^3r_j \tag{193}$$

should be small, especially for $b\gg R$. This fact permits one to expand the logarithm function and obtain:

$$\chi_{opt}(\boldsymbol{b}) = i\sum_{j=1}^{A}\int\rho_j\left(\boldsymbol{r}_{\boldsymbol{j}}\right)\Gamma_j\left(\boldsymbol{b}-\boldsymbol{s}_{\boldsymbol{j}}\right)\mathrm{d}^3r_j+\cdots \tag{194}$$

Considering that all nucleon profile functions $\Gamma_j\left(\boldsymbol{b}\right)$ have the same form $\Gamma\left(\boldsymbol{b}\right)$, one can write χ_{opt} in terms of the average particle density,

$$\chi_{opt}(\boldsymbol{b}) = iA\int\rho\left(\boldsymbol{r}\right)\Gamma\left(\boldsymbol{b}-\boldsymbol{s}\right)\mathrm{d}^3r \tag{195}$$

which is defined as:

$$\rho = \frac{1}{A}\sum_{j=1}^{A}\rho_j\left(\boldsymbol{r_j}\right) . \tag{196}$$

Now, to facilitate the integration in Eq. 195, it will be useful to make explicit the components of the vector $\boldsymbol{r} = (\boldsymbol{s}, z)$ (where z is the longitudinal component of $\boldsymbol{r}$) and to introduce the vector $\boldsymbol{l} = \boldsymbol{b} - \boldsymbol{s}$:

$$\begin{aligned}\int \rho\left(\boldsymbol{s}, z\right)\Gamma\left(\boldsymbol{b}-\boldsymbol{s}\right)\mathrm{d}^3 r &= \int \rho\left(\boldsymbol{b}-\boldsymbol{l}, z\right)\Gamma\left(\boldsymbol{l}\right)\mathrm{d}^2 l dz \\ &= \left(\int \Gamma\left(\boldsymbol{l}\right)\mathrm{d}^2 l\right)\left(\int_{-\infty}^{\infty}\rho\left(\boldsymbol{b}, z\right)dz\right) .\end{aligned} \tag{197}$$

In the last line, it was used the fact that the nucleon density function $\rho(\boldsymbol{s}, z)$ varies very smoothly inside the nucleus and must vanish outside it. This encourages one to make a power expansion at the point $\boldsymbol{b} = \boldsymbol{s}$, i.e., $l = 0$, and to use the first term (which does not depend on l) to separate the integrals.

Now, one can relate the integration of the profile function with the definition of the proton-nucleon scattering amplitude (Eq. 184):

$$f\left(0\right) = \frac{ik}{2\pi}\int \Gamma(\boldsymbol{b})\mathrm{d}^2 b\,, \tag{198}$$

and use it in Eq. 197 to obtain the following expression for the effective phase-shift function

$$\chi_{opt}(\boldsymbol{b}) = \frac{2\pi A}{k} f(0) T_A(b)\,. \tag{199}$$

In this expression $T_A(b)$ is the thickness function, which is defined as $T_A(b) = \int_{-\infty}^{\infty}\rho\left(\boldsymbol{b}, z\right)dz$.

Returning to the elastic nuclear scattering amplitude (Eq. 190), one finds:

$$F_{\mathrm{N}}(\Delta) = \frac{ik}{2\pi}\int \mathrm{e}^{i\boldsymbol{\Delta}\cdot\boldsymbol{b}}\left\{1 - e^{i\chi_{opt}}\right\}\mathrm{d}^2 b = \frac{ik}{2\pi}\int \mathrm{e}^{i\boldsymbol{\Delta}\cdot\boldsymbol{b}}\left\{1 - e^{\frac{2\pi i A}{k} f(0) T_A(b)}\right\}\mathrm{d}^2 b\,. \tag{200}$$

In order to relate the forward proton-nucleon scattering amplitude with a cross section, it is convenient to separate its real and imaginary parts:

$$\begin{aligned}F_{\mathrm{N}}(\Delta) =& \frac{ik}{2\pi}\int \mathrm{e}^{i\boldsymbol{\Delta}\cdot\boldsymbol{b}}\left\{1 - e^{\frac{2\pi i A}{k}[\mathrm{Re}\{f(0)\}+i\mathrm{Im}\{f(0)\}]T_A(b)}\right\}\mathrm{d}^2 b \\ =& \frac{ik}{2\pi}\int \mathrm{e}^{i\boldsymbol{\Delta}\cdot\boldsymbol{b}}\left\{1 - e^{\frac{-2\pi A}{k}\mathrm{Im}\{f(0)\}[1-i\rho]T_A(b)}\right\}\mathrm{d}^2 b\end{aligned} \tag{201}$$

where $\rho = \frac{\mathrm{Re}\{f(0)\}}{\mathrm{Im}\{f(0)\}}$ is the ratio of the real to the imaginary part of the forward scattering amplitude. Considering that the forward scattering amplitude is purely imaginary, one can use the optical theorem to write:

$$F_{\mathrm{N}}(\Delta) = \frac{ik}{2\pi}\int \mathrm{e}^{i\boldsymbol{\Delta}\cdot\boldsymbol{b}}\left\{1 - e^{\frac{-1}{2}AT_A(b)\sigma_{q\bar{q}}}\right\}\mathrm{d}^2 b\,. \tag{202}$$

Lastly, it is worth highlighting that the Glauber formalism was built on the wave function formalism, thus, for the purpose of this work, it is necessary to translate Eq. 202 to the dipole formalism:

$$\mathcal{A}_{\mathrm{N}}(\boldsymbol{\Delta}) = \frac{4\pi}{k} F_{\mathrm{N}}(\Delta) = 2i \int \mathrm{e}^{i\boldsymbol{\Delta}\cdot\boldsymbol{b}} \left\{ 1 - e^{\frac{-1}{2} A T_A(b) \sigma_{q\bar{q}}} \right\} \mathrm{d}^2 b \,. \tag{203}$$

This leads to the following expression for the nuclear scattering amplitude for the coherent $\gamma A \to V A$ process:

$$\mathcal{A}^{\gamma A \to V A}(x, \Delta) = i \int \mathrm{d}^2 r \int_0^1 \mathrm{d}\beta \int \mathrm{d}^2 b \, e^{-i\boldsymbol{b}\cdot\boldsymbol{\Delta}} \Psi_V^*(r,\beta) \Psi_\gamma(r,\beta) 2 \left[1 - e^{-\frac{A T_A(b) \sigma_{q\bar{q}}(x,r)}{2}} \right] . \tag{204}$$